POLITECNICO DI MILANO
Polo Regionale di Como
Facoltà di Ingegneria Civile, Ambientale e Territoriale
Master of Science in Environmental and Land Planning Engineering

PROCESSING OF HIGH RESOLUTION AND MULTISPECTRAL AERIAL IMAGES FOR FOREST DSM PRODUCTION AND TREE CLASSIFICATION

Supervisor Politecnico di Milano: Dr. Giovanna Sona
Supervisor ETH Zurich: Dr. Emmanuel Baltsavias

Master graduation thesis by: Rossana Gini
Student Id. number: 736009

Academic Year 2009/2010

POLITECNICO DI MILANO
Polo Regionale di Como
Facoltà di Ingegneria Civile, Ambientale e Territoriale
Corso di Laurea Specialistica in Ingegneria per l'Ambiente e il Territorio

PROCESSAMENTO DI IMMAGINI AEREE MULTISPETTRALI E AD ALTA RISOLUZIONE PER LA PRODUZIONE DI UN DSM FORESTALE E PER LA CLASSIFICAZIONE DI SPECIE ARBOREE

Relatore Politecnico di Milano: Dr.ssa Giovanna Sona
Relatore ETH Zurigo: Dr. Emmanuel Baltsavias

Tesi di laurea di: Rossana Gini
Matricola: 736009

Academic Year 2009/2010

ABSTRACT

The master project thesis here presented focused on procedures for forestry applications and was embedded in the on-going Ph.D. thesis of Lars T. Waser, entitled "Use of high-resolution airborne remote sensing data for derivation of forest area and tree species composition". In this context, the work dealt with two different, but equally essential, aspects: the use of Unmanned Aerial Vehicles (UAVs) for generating high-resolution DSMs and the study of a selection procedure to find the combination of "variables" (textural, geometrical and spectral information) able to facilitate the separation, in the so-called "multispectral space", between tree species classes.
Encouraging results were produced, even if further studies are needed.

CONTENTS

PART 2 – THE TREE CLASSIFICATION

LIST OF FIGURES

1. UNMANNED AERIAL VEHICLES

2. DATA ORIGIN AND SELECTION

3. IMAGERY PROCESSING

5. MATERIAL

6. VARIABLES SELECTION AND CLASSIFICATION

APPENDIX A: DMSs COMPARISON RESIDUALS

APPENDIX B: TREE SPECIES' APPEARANCE

LIST OF TABLES

2. DATA ORIGIN AND SELECTION

3. IMAGERY PROCESSING

5. MATERIAL

6. VARIABLES SELECTION AND CLASSIFICATION

APPENDIX C: INPUT VARIABLES DETAILS

LIST OF GRAPHS

6. VARIABLES SELECTION AND CLASSIFICATION

APPENDIX D: CONFUSION MATRICES

LIST OF ABBREVIATIONS

AAHRS	Attitude, Altitude and Heading Reference System
AAT	Automatic Aerial Triangulation
ADS40	Airborne Digital Sensor 40
ALTMS	Airborne Laser Terrain Mapping System
AOI	Area Of Interest
AUVSI	Association for Unmanned Vehicle Systems International
BBA	Bundle Block Adjustment
CASA	Civil Aviation Safety Authority
CCD	Charge Coupled Device
CHM	Canopy Height Model
CIR	Color Infrared
DSM	Digital Surface Model
DTM	Digital Terrain Model
ETHZ	Swiss Federal Institute of Technology Zurich *(Eidgenössische Technische Hochschule Zürich)*
EUROUVS	European Association of Unmanned Vehicles Systems
FAO	Food and Agriculture Organization of the United Nations
GCP	Ground Control Point
GNSS	Global Navigation Satellite Systems
GPS	Global Positioning System
IGP	Institute of Geodesy and Photogrammetry *(Institut für Geodäsie und Photogrammetrie)*
IHS	Intensity, Hue, Saturation
INS	Inertial Navigation System
ISODATA	Iterative Self-Organizing Data Analysis Technique
JM distance	Jeffries – Matusita distance
LiDAR	Light Detection and Ranging or Laser Imaging Detection and Ranging
LPS	Leica Photogrammetry Suite
LSM	Least Square Matching
LS3D	Least Square 3D

NDVI	Normalized Difference Vegetation Index
NFI	National Forest Inventory (of Switzerland)
NIR	Near Infrared
PCA	Principal Component Analysis
RC-Helicopter	Remote Controlled Helicopter
RGB	Red Green Blue
RMSE	Root Mean Squared Error
ROA	Remotely Operated Aircraft
RPV	Remotely Piloted Vehicle
RTK-DGPS	Real Time Kinematic-Differential Global Positioning System
SAT-PP	SATellite Image Precision Processing
SWISSTOPO	Swiss Federal Office of Topography
TD	Transformed Divergence
TP	Tie Point
UAV	Unmanned Aerial Vehicle
UVS	Unmanned Vehicle Systems
VTOL AUMAV	Vertical Take Off and Landing Autonomous Unmanned Micro Aerial Vehicle
WSL	Swiss Federal Institute for Forest, Snow and Landscape Research *(Eidg. Forschungsanstalt für Wald, Schnee und Landschaft)*

INTRODUCTION

The master thesis project here presented was carried out at ETH (Eidgenössische Technische Hochschule) Zürich, from March to October 2010 under the supervision of Dr. Emmanuel Baltsavias of the ETHZ Institute of Geodesy and Photogrammetry and Dr. Giovanna Sona of Politecnico di Milano.
The work, focused on procedures for forestry applications, is embedded in the on-going Ph.D. thesis of Lars T. Waser**, entitled "Use of high-resolution airborne remote sensing data for derivation of forest area and tree species composition".

Forest ecosystems, as part of the landscape, represent an important natural resource: precise information on forest area, structure and composition may be helpful for different purposes such as inventories, protection tasks, management and environmental monitoring, playing also a key role in the discussion of carbon sinks.
Moreover, updated and accurate maps of tree species are a necessary input for biodiversity and biomass estimations and they are required by environmental agencies and land surveying offices to assess possible changes in their distribution or condition.

Classification of tree species was historically based on the interpretation and mapping of aerial photographs, employing different methods to identify the individual crowns. However, the development of digital devices, which are supposed to be both spectrally and radiometrically superior to the analogue cameras, and the subsequent diffusion of digital airborne data have promoted the exploration of new procedures and appropriate classification strategies. According to Jensen (2005), for example, these latter depend on different aspects such as the biophysical characteristics of the analysis area, the homogeneity of the remote sensing data and the "a priori" knowledge.
Several studies stress also the advantages of combining multi-resolution segmentation with object-based classification so that the information content of very high resolution images is fully exploited. The growing need of sensitive tools able to predict temporal and spatial patterns of tree species is associated with a parallel increasing usage of predictive spatial modeling, with which the vegetation cover may be reconstructed.

** WSL-Swiss Federal Institute for Forest, Snow and Landscape Research

Although a great progress is still occurring in three-dimensional remote sensing (including stereo-photogrammetry, radar interferometry and LiDAR), one problem remains the fact that the definition of forestry parameters like area, structure and composition can change in the various European countries: what is considered as "forest" is indeed defined differently in the national inventories.
The forest definition adopted by Italy agrees with the one proposed by the Food and Agriculture Organization of the United Nations (FAO):

> «*Forest* is a minimum area of land of 0.05 - 1.0 hectares with tree crown cover (or equivalent stocking level) of more than 10 - 30 per cent, with trees with the potential to reach a minimum height of 2 - 5 meters at maturity in situ. A forest may consist either of closed forest formations where trees of various storeys and undergrowth cover a high proportion of the ground or open forest. Young natural stands and all plantations which have yet to reach a crown density of 10 - 30 per cent or tree height of 2 - 5 meters are included under forest, as are areas normally forming part of the forest area which are temporarily unstocked as a result of human intervention such as harvesting or natural causes but which are expected to revert to forest […]»
>
> *FCCC/CP/2001/13/Add.1*

For forest, Switzerland chose the following definition:

> «*Forest* is a minimum area of land of 0.0625 hectares with crown cover of at least 20% and a minimum width of 25 m. The minimum height of the dominant trees must be 3 m or have the potential to reach 3 m at maturity in situ»

Although orchards, parks, camping grounds, open tree formations in settlements, gardens, cemeteries, sports and parking fields may fulfill the (quantitative) forest definition, they are not considered as forests.
In Switzerland, it's possible to obtain:

a) DISCRETE FOREST MAPS: based on satellite images classification or aerial images interpretation, they are provided from "CORINE Land Cover", "Swiss Federal Statistical Office" and "Federal Office of Topography" (SWISSTOPO);
b) DATA BASED SAMPLE PLOTS: available at "National Forest Inventory" (NFI), they're based on field work and stereo-image interpretation;

c) MAPS OF FOREST DISTRICTS: only partly available, they're often out of date and therefore difficult to compare with other data sets.

It should be stated that actual, accurate and complete spatial data sets, which also include composition and structure, cannot be extracted for any Swiss region from the existing discrete forest maps; a possible alternative for obtaining those parameters would be the interpolation of the NFI sample plots using statistical estimations. However, this would not resolve the problem of having incomplete spatial information.

Inserted in this operative context, the Ph.D. thesis of Lars T. Waser aims at developing algorithms for semi-automated derivation of forest area and tree species composition, using high-resolution airborne remote sensing data. These models must be robust, representative and applicable for typical Swiss regions, with different trees' characteristics: hence, although tested only on three separated areas until now (Üetliberg, Breitmoos and Tarasp), the methods will be of general nature for being applicable to other forest ecosystems.

As already mentioned, the master thesis project is embedded in this Ph.D. work, going to deal with two different, but equally essential, aspects.

First of all, it was necessary to explore methods for generating a high resolution and accurate DSM (it didn't care from what type of sensor, at that stage): from this DSM, it's indeed possible to analyze the forest surface and, subtracting a corresponding DTM, create a so-called Canopy Height Model.

Therefore, the research investigated the use of Unmanned Aerial Vehicles (UAVs), performing a flight with the Microdrones MD4-200 in October 2009. The captured pictures were conveniently elaborated so that a DSM with 0.08 m as grid spacing was created and then compared with standard DSMs, namely, those produced by Aerial Photogrammetry with the ADS40 sensor and the LiDAR system.

In the second part, instead, different types of input variables were derived from aerial data, concerning the test area of Üetliberg (Zürich) and using a sensor ADS40 SH52. Some of these variables, grouped into geometric, spectral and textural features, could be correlated to each other and/or provide redundant information, so that a selection procedure was needed. Hence, the work focused on finding the best variables'

combination able to facilitate the separation, in the so-called “multispectral space”, between tree species classes with similar characteristics.
This operation should improve the subsequent classification, performed with several algorithms (Isodata, Maximum Likelihood method and the one based on the Mahalanobis distance).

Since these two thesis’ components not only had different aims and data sets but also were developed independently from each other, it was decided to maintain this distinction in the report too, describing and analyzing the work done in two separated parts.

PART 1

THE DSM GENERATION

UNMANNED AERIAL VEHICLES

As already happened for many technologies originally born for military purposes, also UAVs showed and are still showing their great potential for photogrammetric measurements in a lot of fields.
Thereby, before facing the current project, it is better to present a brief overview of the UAVs world: definition, development and possible classifications are in succession summarized, followed by the different applications. Challenges for possible future studies are then presented at the end. For further information on UAVs in Photogrammetry, please refer to Eisenbeiss, 2009.

1.1 WHAT ARE UAVs?

«Once we tried to Google "UAV" and got more than two million citations on the Internet. Try to find *the* definition of Unmanned Aerial Vehicle (UAV) and you'll uncover a welter of choices in the literature» (De Fátima Bento, 2008). It has been nearly three years and the citations have become more than 6 million: that's only a clue of the speed with which UAVs are spreading in the scientific and civilian world.

1.1.1 DEFINITION AND DEVELOPMENT

With these conditions, it should be even more difficult to identify *the* definition. However, it could be enough satisfactory *a* definition: let's say that a UAV is a powered aerial vehicle that does not need a human operator physically onboard; it can fly autonomously or be piloted remotely and it uses aerodynamic forces to provide vehicle lift. In particular, UAVs can be remotely controlled, semi–autonomous, autonomous, or have a combination of these capabilities.
This term is widespread in the Computer Science, Robotics and Artificial Intelligence as well as in the Photogrammetry and Remote Sensing communities, but synonyms like Remotely Piloted Vehicle (RPV), Remotely Operated Aircraft (ROA), Remote Controlled

Helicopter (RC-Helicopter), Unmanned Vehicle Systems (UVS) are often used too (Eisenbeiss, 2004).
The recent terminology “UAV Photogrammetry” describes a photogrammetric platform, which operates remotely controlled, semi autonomously or autonomously, without a pilot sitting in the vehicle. The platform is equipped with a photogrammetric measurement system, including thermal or infrared camera systems, airborne LiDAR system or a combination thereof (Eisenbeiss, 2009).

Already in the World Wars, different methods for the aerial transport of cameras were explored and employed for spying, from balloons to kites, from rockets to pigeons.
Therefore it’s possible to say that the UAVs development has its origin in the will of the nations, coming from the terrible experience of the Second World War, of identifying new aerial vehicles able to allow actions of surveillance, reconnaissance and penetration into enemy territory without endangering humans. Nowadays, military UAVs perform reconnaissance as well as attack missions.

Figure 1.1 – A group of aerial demonstrators at the 2005 Naval Unmanned Aerial Vehicle Air Demo

First experiments in the photogrammetric field date back to 1979 (Przybilla and Wester - Ebbinghaus) but, at that time, the results were not satisfactory due to vibrations caused by the rotor, which resulted in image motion. The tests accomplished by the company Hegi with a model aeroplane can be considered the next important step: the vehicle, flying at 150 m on the ground with a speed equal to 40 km/h, was able to acquire useful images of an archaeological area and of architectural sites; moreover, the combination of aerial and terrestrial measurements was carried out.

Since then, the UAVs development and the integration of GPS/INS data onboard has become more and more object of discussion in the UVS international community: the research is now focusing on low cost UAV, open source systems and integration of different sensors, with more investigations on fast processing like online triangulation and direct georeferencing. The considerable reduction of the dimension of sensors and systems must be underlined as well.

1.1.2 CLASSIFICATIONS

Several groups have proposed the creation of reference standards for the UAV international community: however different classifications exist in literature, varying also from one country to another. It should be noted, in fact, that the definition encompasses fixed and rotary wings UAVs, lighter than air UAVs as well as lethal aerial vehicles and uninhabited combat aerial vehicles.

Hence, possible classifications can divide the UAVs into:

- unpowered or powered;
- flexible, fixed or rotary wings;
- single rotor, coaxial, quadrotors or multi-rotors;
- lighter than air (balloons) or heavier than air (kites, quadrotors, etc.).

Moreover, using characteristics such as the size/weight, endurance, maximum flying height and the flight duration, UAVs can be subdivided into:

- micro or mini;
- close, short, medium or long range;
- low, medium or high altitude.

A classification based on these features is adopted by European Association of Unmanned Vehicles Systems (EUROUVS), whereas Australian Civil Aviation Safety Authority (CASA) distinguishes between three classes on the base of the system weight:

a) micro UAVs: take-off weight of 100 g;
b) small UAVs: take-off weight of less than 150 kg;
c) large UAVs: take-off weight of more than 150 kg.

Finally, vehicles can be classified according to their integrated sensors and real–time capability that influence directly the data processing: on one hand, the low–cost sensor with the necessary post georeferencing, on the other hand high–end sensors with the

potential for doing the direct one. Taking into account the implemented sensors and the type of processing, it's possible to identify UAVs that will be suitable only for particular applications.

1.1.3 ADVANTAGES

Compared to manned aircraft systems, many advantages can be exploited by the use of UAVs. In particular, concerning small–scale applications and low–cost systems, they:

- don't need a qualified pilot onboard;
- can be used in environments that are dangerous to human life or not accessible for manned systems (i.e. at low altitude and at flight profiles close to the objects) such as natural disaster sites: volcanic or desert areas, flood plains, earthquake and scenes of accidents;
- can acquire images also in cloudy and drizzly weather conditions, if the distance to the object allows flying below the clouds;
- can be used for high resolution texture mapping as well as for image rectification;
- can guarantee sufficient image coverage and overlap, thanks to the stabilization and navigation units and the implementation of GPS/INS systems;
- are characterized by fast data acquisition and real time transmission to the ground control station;
- are less expensive than manned aircrafts, with lower operating costs;
- can be programmed to complete the mission autonomously.

1.1.4 DRAWBACKS

As all the technologies, UAVs don't differ in presenting some drawbacks. First of all, the sensor payload is limited both in weight and in dimension by low costs and this can influence the selection of some components:

- LOW WEIGHT SENSORS (like small or medium format amateur cameras, see figure 1.2): since they are normally less stable than high–end sensors, the effect is a reduced image quality; furthermore, a higher number of images must be acquired to obtain the same coverage and a comparable image resolution;
- LOW WEIGHT NAVIGATION UNITS: they affect the results for the orientation of the sensors, often less accurate;

- LESS POWERFUL ENGINES: a direct consequence can be some limitations in the reachable altitude.

Figure 1.2 – Microdrones MD4-200 with amateur camera as image sensor

Moreover, another disadvantage can be found in the lack of communication equipments and collision avoidance systems: hence, UAVs are restricted to the flight in line-of-sight because of the lack of communication with the air traffic authorities.
Lastly, commercial software packages applied for photogrammetric data processing are not usually set up to support UAV images: for instance the Automatic Aerial Triangulation (AAT), a standard consolidated technique from Aerial Photogrammetry, often can't be applied to UAVs imagery, due to the presence of scale differences, illumination changes, occlusions and convergence. Hence, new accurate methodologies are under studying, in order to automatically extract image correspondences from UAVs image blocks and to derive the exterior orientation parameters through a bundle adjustment (Barazzetti et al., 2002). In fact, the implementation of standardized workflow and sensor models is as much important as the development of new technologies.

1.2 PRESENT AND FUTURE OF UAVs

As already mentioned, in the past the UAVs development was primarily driven by the military market and then by the artificial intelligence community: more recently, UAVs demonstrated their great potential also for Photogrammetric measurements in many application fields, summarized as “observation, maintenance, surveillance, monitoring, remote sensing and security tasks” (Eisenbeiss, 2004).
However, at the same time it should be underlined that some issues still need to be faced and overcome.

1.2.1 APPLICATIONS

The increased use of UAVs in Photogrammetry can be linked with the diffusion of low cost combined GPS/INS systems which are necessary to navigate the vehicle with high precision to the predicted acquisition points. This aspect surely contributed to the spread of operational UAVs for several application fields:

- cultural heritage: documentation and generation of 3D models (Pueschel et al., 2008);
- archaeological sites: 3D documentation through high resolution imagery (Sauerbier et al., 2010);
- agriculture: precision farming (Herwitz et al., 2002) and insect pest control (e.g. rice, soybeans and wheat);
- forestry tasks: monitoring and determination of vegetation coverage through the use of UAVs as ground truth measurement systems;
- civilian application: 3D buildings or cities modeling, road condition assessment (Zhang, 2008), documentation of industrial constructions, surveying of power lines, pipeline inspection, dam monitoring and recording of cadastral data;
- construction of DSM (Eisenbeiss et al., 2006);
- atmospheric and environmental monitoring.

Furthermore, the extraction of terrain, orthoimages and textured 3D models from UAVs images can be applied to all kinds of hazards, catastrophic or environmental disaster in order to construct and to coordinate urgent response measures: aircraft accidents,

search and rescue operations, fire combat, crop damages, landslides and volcano outburst.

1.2.2 CHALLENGES

This general overview can be concluded with a brief analysis of the challenges still object of studies by the research world.

First of all, the autonomy of flight of micro UAVs is an issue of great importance since they are too small for remote control instrumentation as traditional stability–and–control or navigation units. Also the radar technologies are too large and heavy to be used in smaller UAVs; moreover, neither inertial nor GNSS navigation systems can supply guidance or collision avoidance for autonomous close–proximity flight, which requires the estimation of the UAV accurate position.

Other factors that can play a key role in the achievement of the micro UAVs autonomy are: the miniaturization of the airframe, components and payload, the integration of air traffic management, the development of robust communications (secure and not suffering from signal jamming), the overcoming of problems related to propulsion and energy storage.

A further challenge is represented by the exploitation of onboard cameras as obstacle avoidance system: namely, by the creation of a simple and efficient computer vision algorithm able to convert images into a real time guidance and obstacle avoidance system, practical for being used in small UAVs. In fact sensing technologies (such as laser range finders or radar) are already available for medium and large UAVs.

Lastly, a powerful coordination and cooperation of multiples vehicles is still a current research subject (De Fátima Bento, 2008).

DATA ORIGIN AND SELECTION

In the previous chapter, the UAVs importance in the photogrammetric and remote sensing fields was underlined: the practical demonstration is indeed their increasing presence not only for civil applications and for modeling of buildings, but also for archaeological and forestry purposes. However, before a new technology spreads more and more, it's desirable that research explores its several uses in order to identify potentials and weaknesses and try to overcome the latter ones (giving useful information for the development of appropriate software, identifying best procedures and/or methodologies and so on).
As already said, this project was born to meet the need of knowing the reliability of a DSM generated by UAVs, in particular when it's employed for forestry purposes.
To discover this aspect, a comparison with standard DSMs, i.e., those obtained by ADS40 sensor and by LiDAR system, was carried out.

In this chapter, details of the chosen testing area, of the used equipment and of the images' generation are provided, followed by the description of the data sets selected to be processed.

2.1 TESTING AREA

Of course, it was advisable to find a region with representative characteristics for the study's aim, namely, a forestry terrain: this was identified in Üetliberg, a hill of the Albis chain (part of the Swiss Plateau) in the Canton of Zürich, Switzerland (Figure 2.1).
In particular, it was chosen a rectangular portion with 100 m x 250 m as dimensions, area equal to 2.5 ha and altitude between 680 and 710 meters above the mean sea level.

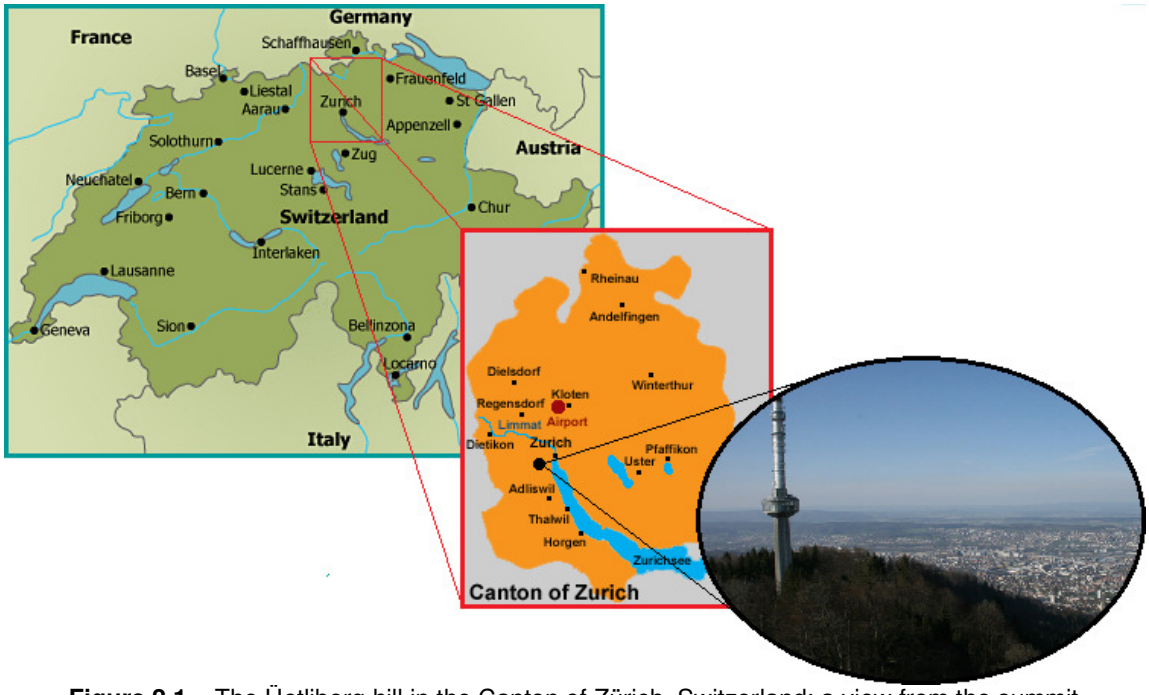

Figure 2.1 – The Üetliberg hill in the Canton of Zürich, Switzerland: a view from the summit

This selection was made in such a way to comprehend, at the same time, distinct surfaces of modeling: so, a road becomes a flat surface and the small pine trees along its sides reproduce single objects. Further, a complex surface is a zone that includes trees with different heights while, if they are similarly tall, data with continuous features is represented.

To sum up, trees of several species, height and age grow in the testing area, which is therefore characterized by shrubs, mixed forest (deciduous species) and young conifers.

Figure 2.2 – Images of the testing area: the road, the small pine trees and the mixed forest

It should be stated that modeling a forest is not a procedure as simple as it may seem: a wood is a very complex surface and this can be understood only thinking that it's constituted by a set of objects, the trees. They have not only different aspect and shape, but also a not so well-defined geometry; in addition, it's necessary to consider the presence of small branches and leaves which are moving thanks to the wind. This implies they may easily change their position and orientation in two consecutive images, thereby making really difficult the identification of the so-called "tie points" (i.e. points located on elements in common to the pictures) and, consequently, the subsequent reconstruction of the distinct trees.

2.2 EQUIPMENT

Before planning the flight in details, the first step is the choice of the most appropriate equipment, namely, the flight platform, the image sensor and the GPS instrument for measuring the GCPs.

2.2.1 FLIGHT PLATFORM

The quadrotor Microdrones™ MD4-200 was selected as the optimal flight platform from which taking images: it's a Vertical Take Off and Landing Autonomous Unmanned Micro Aerial Vehicle (VTOL AUMAV), designed to perform tasks in the field of documentation, coordination, exploration, surveying and communication.

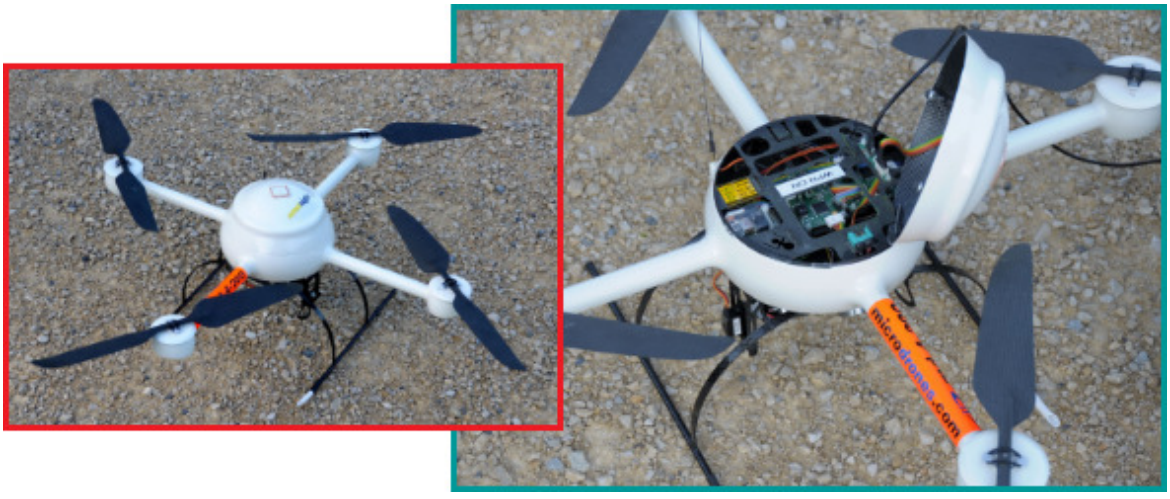

Figure 2.3 – The Microdrones MD4-200

MD4-200 is made of carbon fiber materials and it can fly by remote control or autonomously, using the automatic pilot function and thanks to the aid of a GPS navigation system. Equipped with four motors, it owns an efficient Attitude, Altitude and Heading Reference System (AAHRS) which integrates different instruments: an accelerometer, a gyro, a magnetometer, a barometer, a thermometer and a hygrometer. Moreover, the MD4-200 is furnished with the software "mdCockpit" which allows the user to manage all the functions needed to plan, monitor and analyze the flights.
More technical specifications are listed in the following table:

MICRODRONES MD4-200	
Vehicle weight	585 g
Payload capacity	up to 200 g
Size	< 70 cm (rotor axis/rotor axis)
Flight duration	> 30 min
Flight radius	max. 500 m
Flight altitude	max. 150 m
Power supply	4 Cell LiPo 2300 mAh, 14.8 V
Humidity	max. 80%
Temperature	0-40°C
Wind speed	4 m/s (for sharp pictures)

Table 2.1 – Microdrones MD4-200 technical specifications

2.2.2 CAMERA

Figure 2.4 – The chosen digital camera

Panasonic Lumix DMC-FX35 is a digital and extremely compact camera with high resolution and wide angle capability, suitable for both beginners and experienced users. Its performances and dimensions make it the appropriate image sensor for the project: with a width of 94.7 mm, a height of 51.9 mm and a weight of 160 g (with battery and card), this camera could be easily mounted on the Microdrones MD4-200.

The camera features a CCD image sensor and an effective resolution of 10.1 megapixels and it can take photos with 3648 x 2736 pixels as maximum resolution. Other technical specifications are:

PANASONIC LUMIX DMC-FX35	
Min. focal length	4.3968 mm ~ 4.4 mm
Image sensor dimensions	6.13 x 4.60 mm
Pixel size	0.00168 mm
Format	JPEG

Table 2.2 – Panasonic Lumix DMC-FX35 technical specifications

Figure 2.5 – The Panasonic Lumix DMC–FX35 camera, mounted on the Microdrones MD4-200

2.2.3 GPS EQUIPMENT

Figure 2.6 – The Leica GPS equipment

It was decided to measure the Ground Control Points using the Real Time Kinematic Differential GPS method (RTK-DGPS).

A Leica antenna was fixed on a ranging rod and, through the employment of a controller with graphical interface, the points' coordinates were estimated, placing the equipment on a signalized GCP and then moving to the following one.

2.3 DATA GENERATION

2.3.1 FLIGHT PLANNING

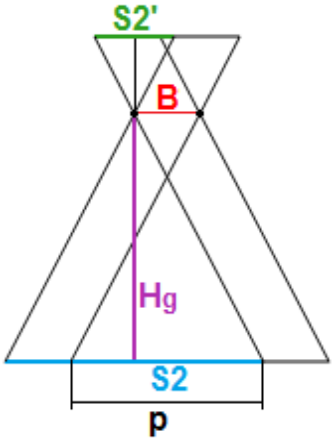

Figure 2.7 – Lateral view of the flight planning geometry

The flight planning began from the technical specifications of the chosen equipment (e.g. the camera ones) and from a set of initial parameters such as the height of flight (H_g), the testing area dimensions (L_q, L_p) and, lastly, the long-strip and the cross-strip overlaps (p, q).

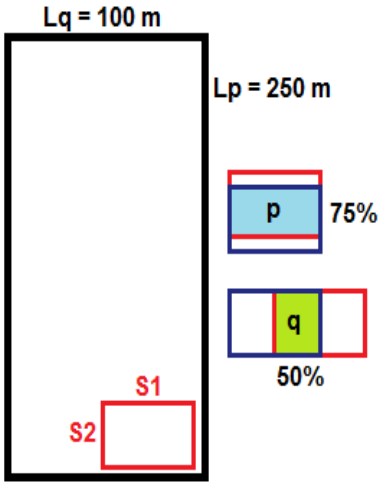

Figure 2.8 – Testing area dimensions and overlaps

Hence, not only the base length and the distance between strip axes, but also the number of photos and of strips were computed using the appropriate formulas, as it's possible to see in figure 1.9:

Flight height	Hg	60 m
Focal length	f	0.005 m
Image scale	m_b = Hg / f	12000
Sensor size	S1'	6.13 mm
	S2'	4.60 mm
Ground cover	S1 = S1' x m_b	73.56 m
	S2 = S2' x m_b	55.20 m
Along-strip overlapping	p	75 %
Cross-strip overlapping	q	50 %
Single frame area	FA = S1 x S2	4060.512 m^2
		0.406 ha
Base length	B = S2(1 - p/100)	13.8 m
Distance between strip axes	A = S1(1 - q/100)	36.78 m
Length of flight line	Lp	250 m
Wide of area	Lq	100 m
Number of photos per strip	Np = [(Lp/B) + 1] + 1	20
Number of strips	Nq = (Lq/A) + 1	4

Figure 2.9 – Flight planning: an extract of the calculation sheet

2.3.2 DATA ACQUISITION

The field trip was carried out on the morning of October 15, 2009 in a sunny but a bit windy day; the images were acquired by performing two separate flights, the first around 10.00 and the second one at about 10.30 a.m.

The control unit received as input all parameters needed to coordinate the flight path: therefore, the quadrotor Microdrones MD4–200 flew autonomously on the testing area, thanks to the automatic pilot function, while the take–off and the landing were remotely controlled by the operator. Moreover, it was possible to check the flight status on the monitor of the control unit, where the battery level, the signal quality, the wind speed and other information were displayed; at the end, they were downloaded and saved.

Figure 2.10 – The control unit and the Microdrones MD4-200 in flight

The decision of performing two flights has allowed to acquire a large amount of images (about 50), among which choosing the best ones to be processed: all the pictures were RGB, 8-bit with dimensions of 3648 x 2736 pixels that are equivalent, as already seen, to an area of 73.56 m x 55.20 m.

Taking into account the flight height of 60 meters, the image quality was enough satisfactory: however, it should be noted that the sunny weather and the time (10-10.30 a.m.) caused the presence of shadows, while the wind created blurring effects. In general, both of them bring to a reduction of objects' details and to a consequent higher difficulty in finding Tie Points (TPs), affecting the quality of the final DSM.

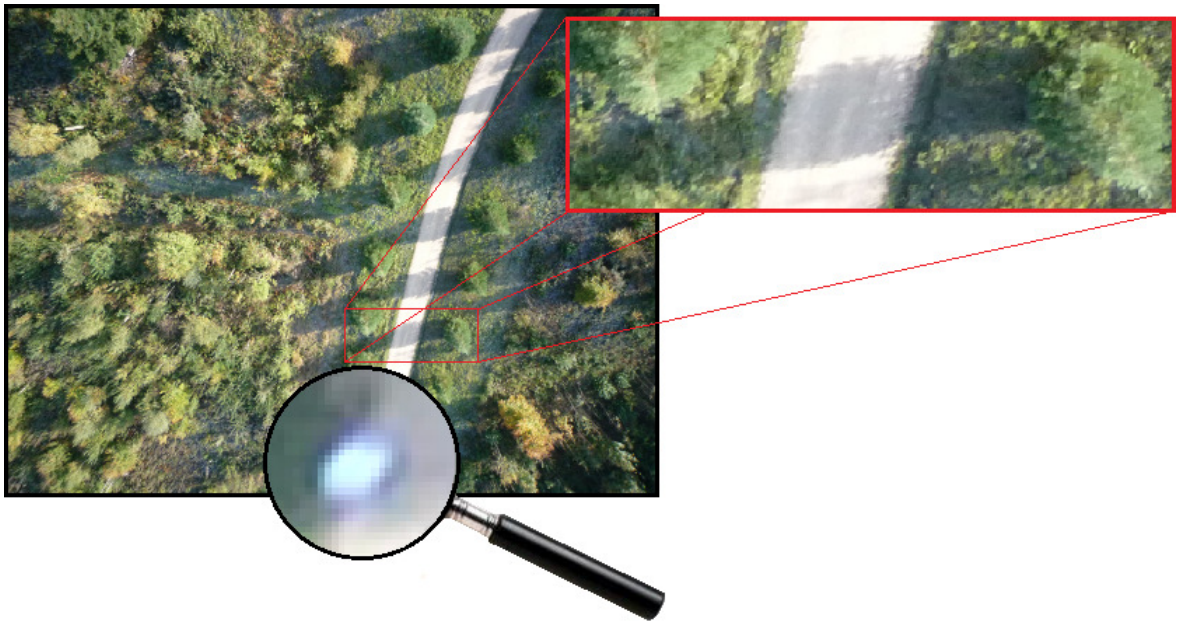

Figure 2.11 – Sample image with some problems pointed out

For what concerns the GCPs, signalized points were considered, that is, circular targets fixed manually on the ground with the aspect of black circles, inside which there're others, white and smaller. It should be specified that:

- the centers of the *internal white circles* are actually the signalized points; since it's important they're clearly visible and identifiable in the images, their dimension is designed starting from the ground resolution of these latter. In this project, the ground resolution is equal to 2 cm, therefore the diameter was set to 20 cm;
- the *external black circles* act as background for ensuring a sufficient contrast with the white ones and for marking their edges.

Figure 2.12 – Signalized GCP placed on the road

Figure 2.13 – Signalized GCP

Hence, the targets were spread in the testing area so that one of them, at least, was visible in each image: some were positioned along the road (as in figure 2.12), others in the grass for a total of 7 GCPs.

As already mentioned, the GCPs were measured through the RTK-DGPS method:

- *Real Time Kinematic (RTK)*: survey carried out with two receivers, one fixed ("base") and one mobile ("rover"), connected via radio modem or mobile phone. The base receiver acquires its position, computes the corrections (a set of parameters, mainly atmospheric) and then sends them to the rover; this latter acquires them as well as its position in real time and solves the so-called "initial ambiguity" (i.e. it fixes the ambiguities), with characteristic accuracy of centimeters (typically, 2 or 3);

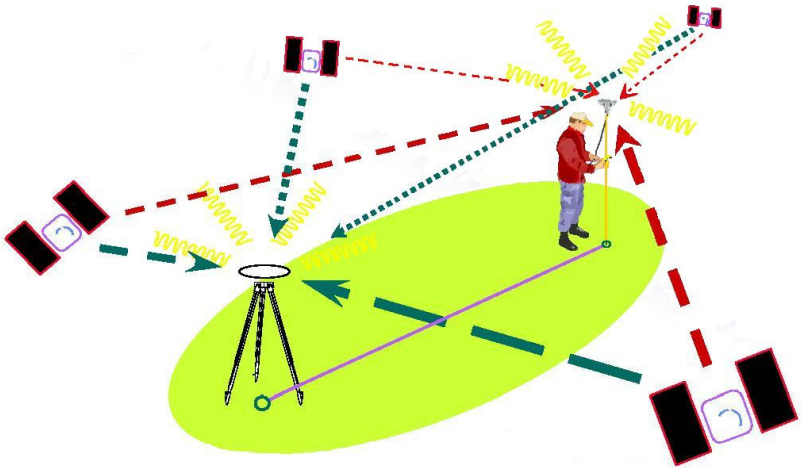

Figure 2.14 – Scheme of the RTK method

- *Differential GPS (DGPS)*: some fixed, ground based reference stations broadcast the difference between the known fixed positions (internally estimated) and the ones indicated by the satellite systems; hence, the receiver stations may correct their pseudorange (the distance between a satellite and a receiver) by the same amount.

The GCPs measurements were acquired in the Swiss coordinate system with accuracy of 1 – 2 cm.

2.4 FINAL DATA SELECTION

The following is the final data processed in the project: the two standard DSMs, used for the comparison, are briefly described before the selected images.

2.4.1 DSM GENERATED BY ADS40 SENSOR

Produced by Leica, the ADS40 is an Airborne Digital Sensor system that unites photogrammetric precision for positional accuracy of processed data with multispectral capabilities for image analysis and interpretation. The three main components are:

a) the SENSOR HEAD (first generation: SH40, second generation: SH51 & SH52): it has individual CCD lines for panchromatic, red, green, blue and NIR bands with 12000 pixels and 6.5 µm pixel size (Sandau et al., 2000); the spectral bands are narrow, non-overlapping and have a response with almost a rectangular shape and a radiometric resolution of 12-bit;

b) the CONTROL UNIT CU40: it records the data and it's integrated with a mass memory MM40 that consists of a high–capacity disk array;

c) the IMAGE PROCESSING SOFTWARE Leica GPro: it allows to download and ground process ADS40 imagery.

The sensor is mounted on a plane and the images, taken during the flight on the area of interest, are processed with methods of classical Aerial Photogrammetry that lead, through different steps (e.g. preprocessing, matching, image orientation, stereo pairs) to the generation of a DSM.

Figure 2.15 – Leica ADS40 sensor

The standard DSM used in this project was generated with resolution equal to 0.50 m, from aerial images taken on January 13, 2009 (leaves–off); it was entirely provided by the Swiss Federal Institute for Forest, Snow and Landscape Research (WSL).

2.4.2 DSM GENERATED BY LiDAR

LiDAR is an optical remote sensing technology that measures properties of scattered light to find range and/or other information of a distant target. The use of laser pulses is the prevalent method to determine the objects' distance, estimated by measuring the time delay between the transmission of a pulse and the detection of the reflected signal.

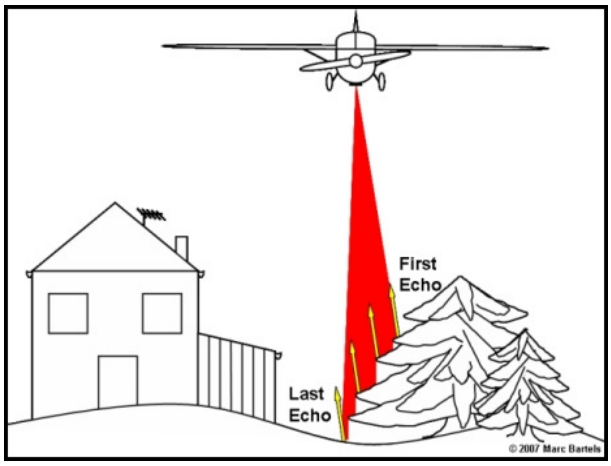

Moreover, not only it scans the surface evaluating the vegetation layer, but it also penetrates to the ground providing important information on it and assessing heights with accuracy of centimeters. Hence, it's an efficient technology for the acquisition of DTMs and DSMs of large portions of territory.

Figure 2.16 – Airborne LiDAR data acquisition

Swiss national LiDAR data was acquired by Swissphoto AG/TerraPoint, employing an ALTMS 2536 system with an average flight height above ground of 1200 m. A first flight was performed in March 2002 while a second one in March 2003 (leaves-off in both cases).

The DSM was generated by SWISSTOPO with average density equal to 0.5 points/m^2 and height accuracy (1σ) of 0.5 m for open areas and 1.5 m for vegetation and buildings (Artuso et al., 2003). Hence this standard DSM, with resolution equal to the first one (by ADS40), was entirely provided by WSL.

2.4.3 SELECTION OF IMAGES BY MICRODRONES MD4-200

The images' selection was carried out on the base of two criteria:

1) the condition of along–strip and cross–strip overlaps, respectively equivalent to 75% and 50%, should be satisfied;
2) the details are not blurred, after zooming in on them.

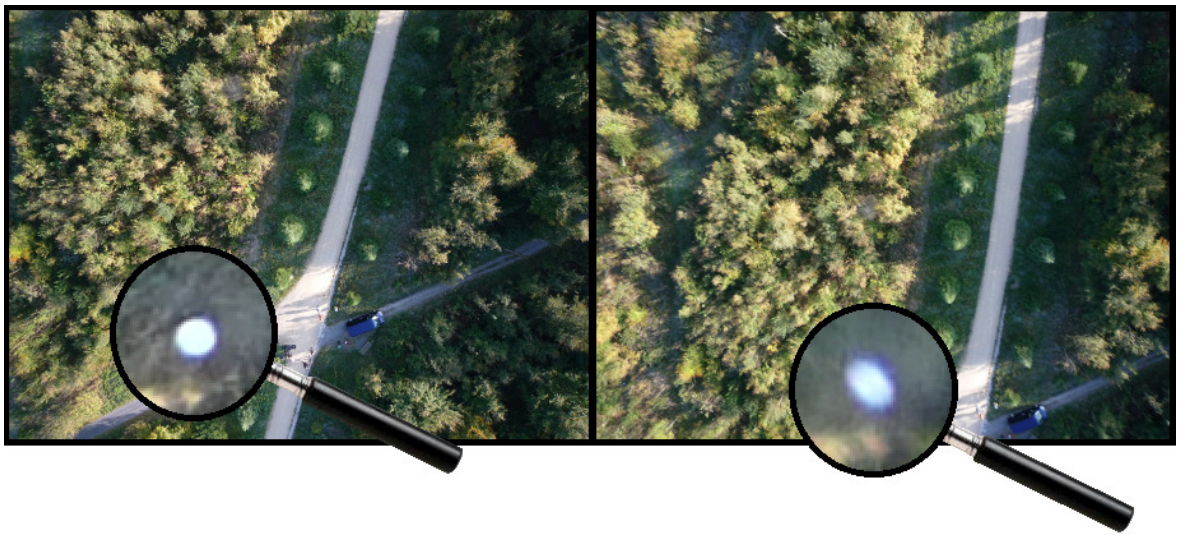

Figure 2.17 – The same area, in a rejected image (on the right) and in an accepted one (on the left): the GCP, zoomed in 200%, well shows the blurring and deformation effects in the first one

An initial selection (14 images in 2 stripes) was done by Jedsada Kerdsrilek for his master thesis project entitled "Application of airborne remote sensing in forest tree (Comparison of ADS40, UAV and LiDAR data)": he mainly used implemented functions of the software LPS (e.g. the automatic TPs generation), producing a DSM with resolution of 0.20 m.

Even though the datasets were the same, the work described in this report is aimed at improving the above one, identifying the best procedure to generate a higher resolution DSM (with 0.08 m as grid spacing). Therefore, it was decided to consider only 8 images belonging to a single strip (the other, more affected by the wind, followed a quite curvilinear path). This new smaller area was chosen in such a way that the flat road and its surroundings were included: the road was indeed regarded as a reference area in the subsequent comparisons with the standard DSMs.

IMAGERY PROCESSING

After the data generation and selection, in this chapter the description of the actual processing phase is presented:

1) RADIOMETRIC PREPROCESSING: to make the TPs matching easier, a noise estimation in homogenous areas was briefly performed, followed by its reduction; then the Wallis filter was employed to enhance the contrast of the images;
2) MATCHING: the image coordinates of both GCPs and TPs were identified;
3) AERIAL TRIANGULATION: exterior orientation parameters and TPs object coordinates were estimated;
4) DSM GENERATION: for extracting a DSM with 0.08 m as grid spacing, new points were selected on the ground in overlapping areas of epipolar images;
5) DSMS CO-REGISTRATION: comparison between the three DSMs to understand the reliability of that generated by UAV.

The whole workflow is outlined below in figure 3.1.

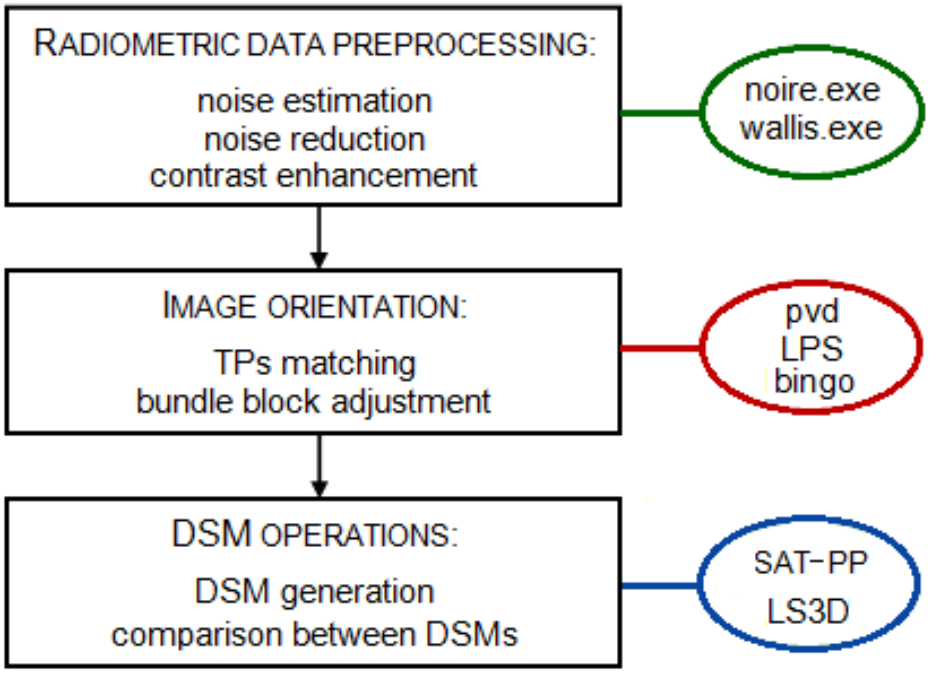

Figure 3.1 – The workflow with the employed software

3.1 IMAGES AND GROUND CONTROL POINTS

Already described in the previous chapter, the selected data set was composed by:

- 8 RGB images: 8-bit with dimensions of 3648 x 2736 pixels, roughly equal to 73.56 m x 55.20 m;
- signalized GCPs put along the road.

For simplicity, a new notation (used from now on and summarized in table 3.1) was assigned to GCPs and images; in particular, these latter were renamed with the last three digits of their original name:

P1030620.jpeg ⟹ 620.jpeg

IMAGES NAME	GCPS NOTATION
615	4
618	4 & 1
620	1
624	1 & 2
625	2
628	2
630	2
632	3

Table 3.1 – GCPs in each image, with notation

It should be pointed out that the GCPs are all aligned in the center of the photos and that the number 3 is visible only in the image 632 and therefore not very useful for the external orientation of the block (see figure 3.3).

Moreover, the three RGB channels were subdivided to create 3 new monochromatic images for each of the old ones, for a total of 24 pictures saved as *.tiff* without compression.

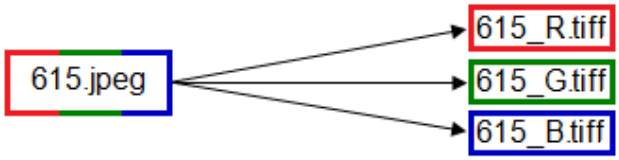

Figure 3.2 – Subdivision into three separate channels

Figure 3.3 – Overview of the 8 images: the GCPs are circled and identified by their notation

Then, a planimetric and altimetric transformation of the GCPs object coordinates was performed, in order to generate later a DSM in the same reference frame of the standard ones: therefore the special webpage of SWISSTOPO** was used for this purpose, by allowing the passage to the Swiss national system called LV03.

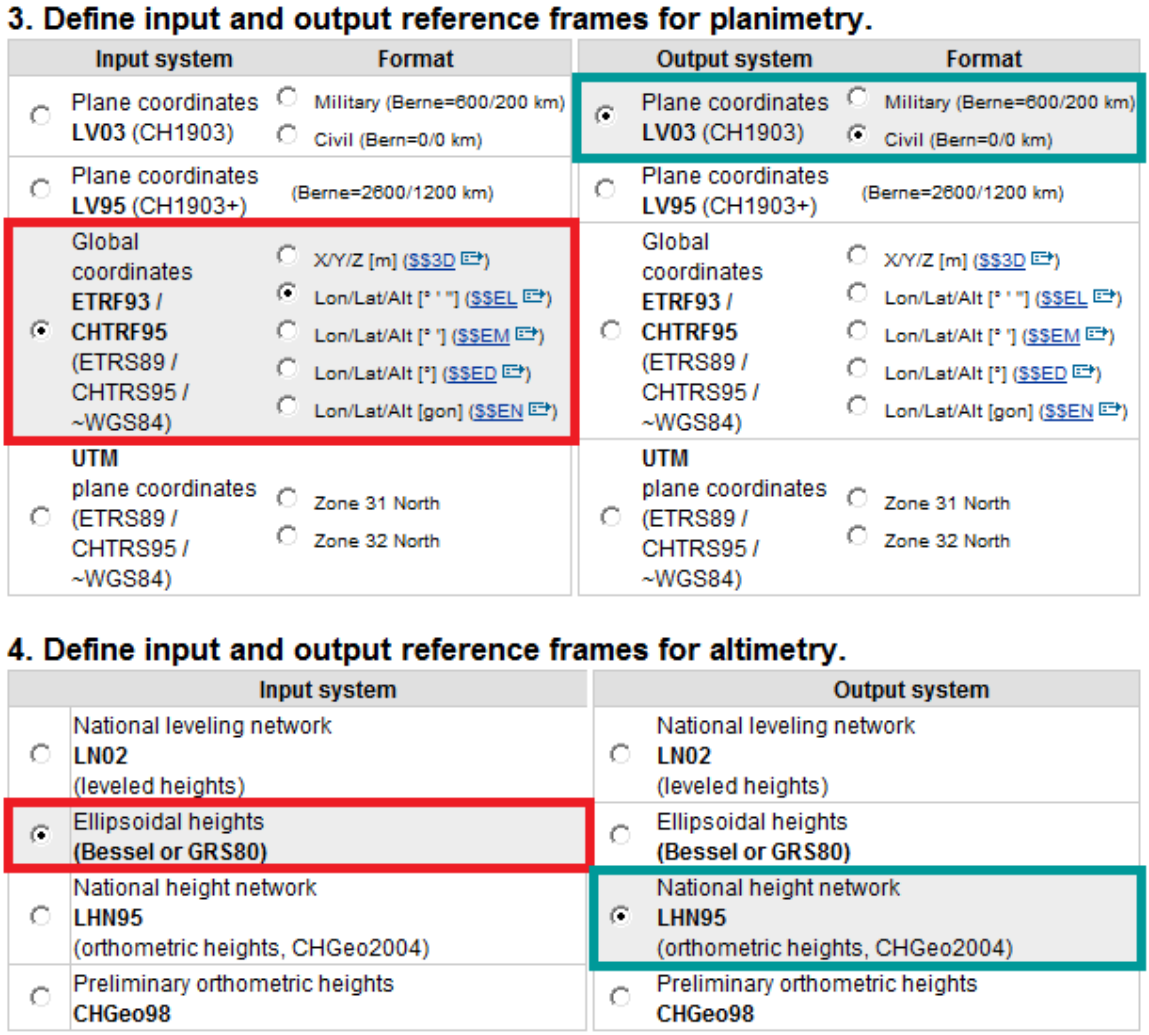

3. Define input and output reference frames for planimetry.

Input system	Format	Output system	Format
○ Plane coordinates **LV03** (CH1903)	○ Military (Berne=600/200 km) ○ Civil (Bern=0/0 km)	◉ Plane coordinates **LV03** (CH1903)	○ Military (Berne=600/200 km) ◉ Civil (Bern=0/0 km)
○ Plane coordinates **LV95** (CH1903+)	(Berne=2600/1200 km)	○ Plane coordinates **LV95** (CH1903+)	(Berne=2600/1200 km)
◉ Global coordinates **ETRF93 / CHTRF95** (ETRS89 / CHTRS95 / ~WGS84)	○ X/Y/Z [m] ($$3D) ◉ Lon/Lat/Alt [° ' "] ($$EL) ○ Lon/Lat/Alt [° '] ($$EM) ○ Lon/Lat/Alt [°] ($$ED) ○ Lon/Lat/Alt [gon] ($$EN)	○ Global coordinates **ETRF93 / CHTRF95** (ETRS89 / CHTRS95 / ~WGS84)	○ X/Y/Z [m] ($$3D) ○ Lon/Lat/Alt [° ' "] ($$EL) ○ Lon/Lat/Alt [° '] ($$EM) ○ Lon/Lat/Alt [°] ($$ED) ○ Lon/Lat/Alt [gon] ($$EN)
○ **UTM** plane coordinates (ETRS89 / CHTRS95 / ~WGS84)	○ Zone 31 North ○ Zone 32 North	○ **UTM** plane coordinates (ETRS89 / CHTRS95 / ~WGS84)	○ Zone 31 North ○ Zone 32 North

4. Define input and output reference frames for altimetry.

Input system	Output system
○ National leveling network **LN02** (leveled heights)	○ National leveling network **LN02** (leveled heights)
◉ Ellipsoidal heights **(Bessel or GRS80)**	○ Ellipsoidal heights **(Bessel or GRS80)**
○ National height network **LHN95** (orthometric heights, CHGeo2004)	◉ National height network **LHN95** (orthometric heights, CHGeo2004)
○ Preliminary orthometric heights **CHGeo98**	○ Preliminary orthometric heights **CHGeo98**

Figure 3.4 – An extract from the SWISSTOPO webpage

** see Website Citations for more information

3.2 RADIOMETRIC PREPROCESSING

Radiometric preprocessing started with the selection of the “best channel” for optimizing the matching step (it must be pointed out that the software “pvd” requires single channel inputs). Then, a noise reduction filter was applied to reduce the noise level and minimize the noise amplification that could occur during the subsequent contrast enhancement.

3.2.1 CHANNEL SELECTION

The “best channel” should be that with less blur and distortion but, it must be said, the operation is less immediate and simple than it could seem.
For the choice, in fact, it was useful to keep in mind some a priori knowledge:

- CCD IMAGE SENSORS: today, they are usually designed using the “Bayern pattern”, namely, a particular arrangement of red, green and blue pixels to create a color image. Half of the pixels are employed to collect the green, with the remaining evenly split between red and blue: in other words, since CCD sensors are less sensitive to the blue and red components of light, the *green* channel is often the best one;
- CONTRAST AND BLUR: the presence of high contrast, which means big histogram’s standard deviation, is important in order to facilitate the matching. The channel that satisfies better this aspect is usually the *red* one, whereas the blue is the worse as it happens for what concerns the blurring effects (that affected the GCPs’ borders);
- DIMENSIONS: the objects’ dimension usually decreases passing from the blue to the red, with the *green* channel that represents the best compromise.

Since a “regular circle” with standard size was taken as target in the matching, it was not so negligible to select the channel in which GCPs looked as similar as possible to it.
In the red channel, the contrast was greater but the GCPs’ white circles appeared usually smaller and often deformed in ovals. On the other hand, in the blue layer they were larger and clearly blurred in most of the cases.

Thus, on the basis of the observations listed above and of the practical analysis, the GREEN channels represented a good compromise because they were characterized by enough contrast and contained blur's effects, whereas the size of the GCPs was between the reduced one of the red and the enlarged one of the blue.
Nevertheless, it was sometimes hard to choose due to the too much deformed shape of the signalized GCP, shape that didn't change at all passing from the total RGB image to the single channels (see figure below).

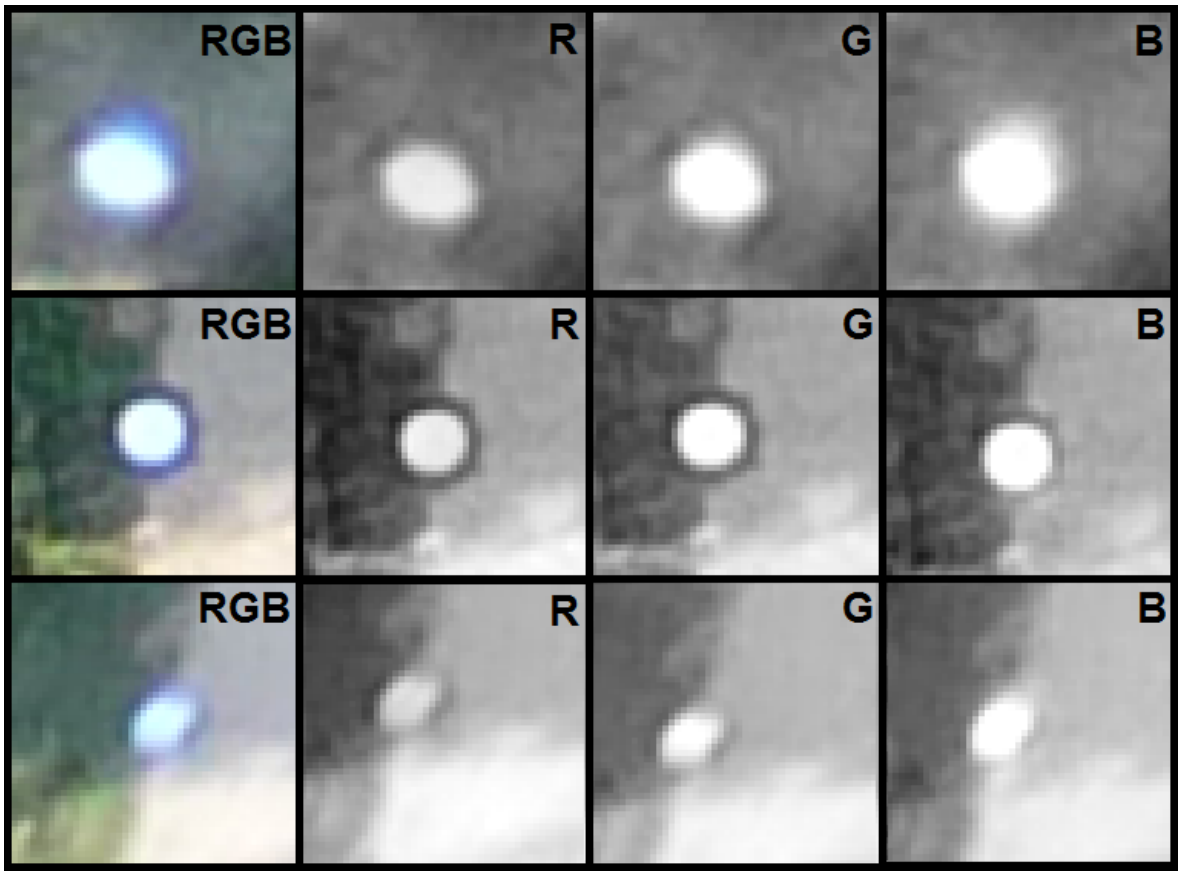

Figure 3.5 – How signalized GCPs look in the different layers with zoom equal to 400%: at the top, image 618 shows how size and blur change in the channels; in the middle, a good-looking GCP (photo 625), whereas the 630 presents, at the bottom, an example of distortion that remains unchanged everywhere. The green channel seems always the best compromise

3.2.2 NOISE ESTIMATION AND REDUCTION

In general, the radiometric accuracy of an image sensor is affected by different noise sources (e.g. dark current noise, thermal noise, etc): since it's not so easy to separate one from the others, it's better to analyze the overall noise characteristics in homogenous areas.

IMAGE	ST. DEVIATION σ
615	3.59
618	3.25
620	3.52
624	3.62
625	3.83
628	3.88
630	3.93
632	3.38

Table 3.2 – Standard deviations of homogeneous areas

Therefore, their manual selection was done in Adobe Photoshop to be able to check the homogeneity by looking the histogram standard deviation (i.e. the dispersion of the gray values): since it should be as small as possible, "narrow" histograms are preferred. The objective of identifying areas neither too underexposed nor too overexposed was achieved in the choice of regions in the shade on the road: however, the operation was more difficult for pictures from 625 to 632, since the road was almost completely illuminated by the sun and the few present shadows were characterized by large noise. Hence the corresponding areas, although smaller in size, had higher standard deviations than the others (as figure 3.6 well shows).

The method «adaptive edge preserving smoothing», implemented in "noire.exe" and developed at ETHZ-IGP, represents a good compromise to reduce noise by preserving even fine details such as one pixel wide lines. The algorithm calculates the homogeneity through absolute differences of pixels, neighboring to the central one in a 3 x 3 mask, and then compares these differences to a threshold T. When T is too small, smoothing of homogeneous areas and sharpening are less, whereas edges remain; on the contrary, if T is too big, small gray value differences in homogeneous regions disappear (Pateraki, 2005).

Thus, the thresholds T were set equal to $3 \cdot \sigma$, where σ stands for the above standard deviations, obtaining values between 10 and 12; these noise estimates were put in "noire.exe" and the files were processed.

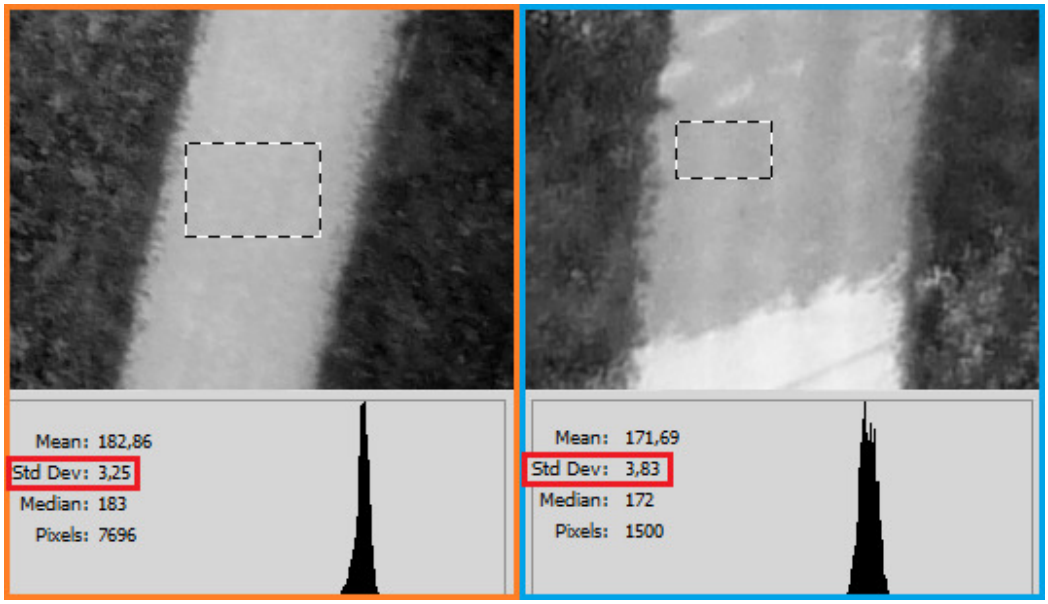

Figure 3.6 – Picture 618 (on the left) and 625 (on the right): comparison between homogeneous areas and their standard deviations

3.2.3 CONTRAST ENHANCEMENT

Wallis filtering is an important step in the images preprocessing for future operations like matching and DSM generation: it applies a contrast enhancement to increase signal variation in parts with less texture (shadowed areas for example) and to improve features definition. However, noise amplification occurs in parallel to the signal one and its indicators are usually chess pattern noise or random noise: precisely to avoid this effect, noise level was reduced prior to contrast enhancement.

Indeed, if the reverse order had been applied, after Wallis filtering, small structures couldn't have been distinguished anymore from the image noise and they would have disappeared during the subsequent step of noise reduction (Pateraki, 2005).

Therefore, the goal was to force the mean and especially the standard deviation to fit to some target values, for obtaining as much as possible a histogram with equal level of saturation on both sides.

The most important parameters, with starting values assigned by default, were:

- *target mean*: 127 → the Gaussian function should cover all the gray values' interval and for this reason, at the beginning, it was set in the middle of the range [0, 255]. Since the saturation in the histogram's right part was usually bigger, for

reaching an equal one it was necessary to decrease the mean, moving it to the left part;

- *target standard deviation*: 40-60 → it affects the level of saturation: indeed, if it's too high, the saturation will be excessive with consequent loss of information. The initial standard deviation was taken from the image's histogram, displayed in Adobe Photoshop;
- *brightness enforcing constant*: 0.5-1 → concerning the mean, it determines how much to enhance the new target value: it was always set equal to 1, that is, the new mean was totally applied;
- *contrast enforcing constant*: 0.75-1 → it works as the previous parameter but concerning the standard deviation; it's very important because it has the strongest influence on noise (and on its growing) and so it should be kept between 0.90 and 0.96.

How much saturation is acceptable is subjective but it should not be too much, otherwise objects disappear (so, it was decided to get values between 0.04% and 0.05%): in order to take this aspect under control and to understand how much the statistics had to be changed, the images' histogram was visualized in Adobe Photoshop after each running of "wallis.exe".

Table 3.3 and figure 3.7 show, numerically and visually, the parameters' variation needed to get the final filtered images, renamed then by putting the "W" of Wallis before the number (e.g. W615_G.tiff).

IMAGE	PARAMETERS	FIRST RUN	SECOND RUN	FINAL RESULT	SATURATION
N615_G	Mean St. Deviation Contrast constant	127 55 0.95	120 55 0.94	110 46 0.94	Left: 0.043 % Right: 0.043%
N618_G	Mean St. Deviation Contrast constant	127 60 0.98	120 50 0.94	120 47.5 0.94	Left: 0.044% Right: 0.045%
N620_G	Mean St. Deviation Contrast constant	127 57 0.98	120 45 0.94	120.3 47.8 0.94	Left: 0.045% Right: 0.044%
N624_G	Mean St. Deviation Contrast constant	127 55 0.98	120 50 0.95	114.5 47.8 0.94	Left: 0.045% Right: 0.045%

Table 3.3 – Example of parameters' variation, where N615_G, for instance, is the green channel of the image 615 after the noise reduction

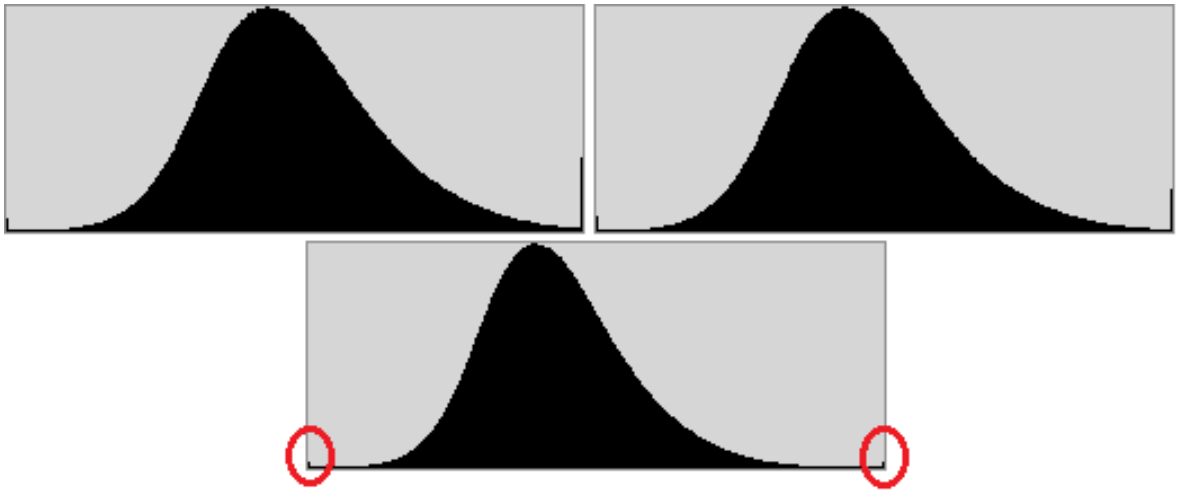

Figure 3.7 – Image N615_G.tif during the different steps, 'till the final result with equal saturation on both sides

It should be noted that, after the Wallis filtering, the images are not really "good-looking" but they're for sure useful for improving the results of the matching.

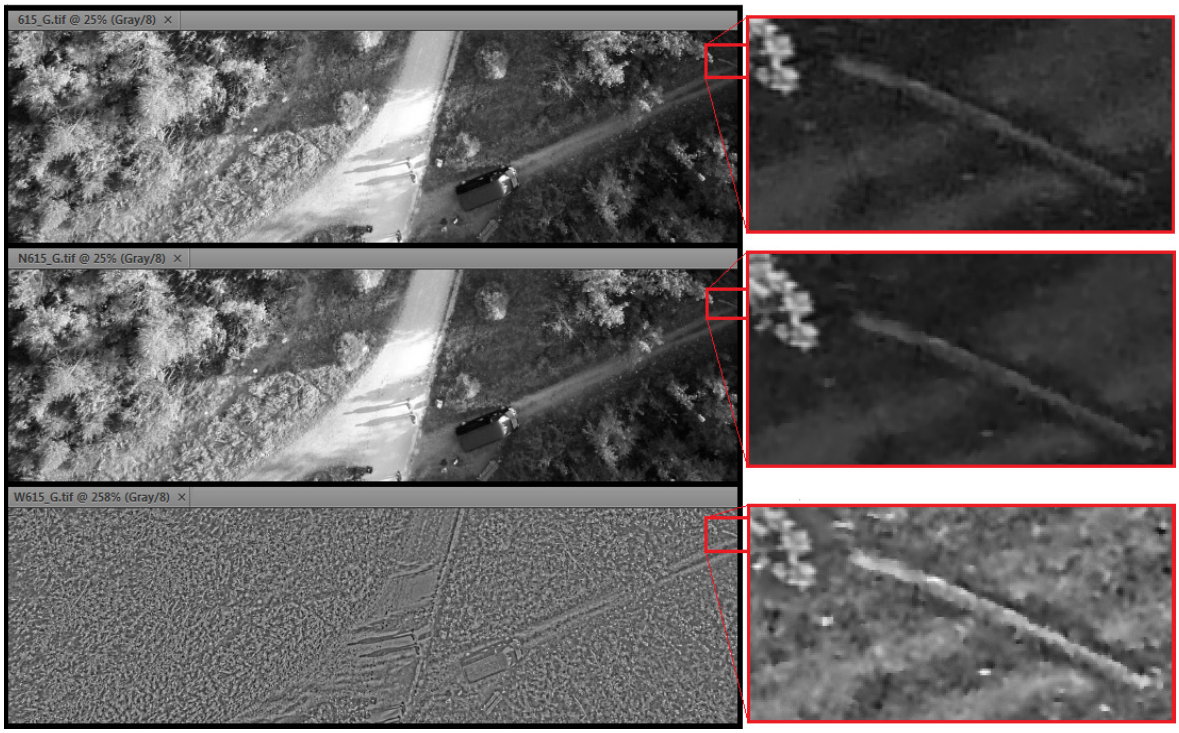

Figure 3.8 – From the top to the bottom, images 615_G, N615_G and W615_G: an extract (on the left) and a detail on the right

3.3 IMAGE MATCHING

A Tie Point (TP) is a point visually recognizable with unknown ground coordinates, whereas the image ones are identified and measured, either manually or automatically, in the overlap area between two or more images; the object coordinates are then computed during block triangulation.
A manual procedure was here preferred in order to avoid a coarse or wrong TPs identification (in fact, the automatic algorithms often locate TPs on the shadows borders) and to improve the external orientation.

3.3.1 TPs SELECTION

TPs should be both visually well–defined in all images and with a good distribution in the overlap areas: for each of these, it was decided to pick out 12 tie points, 10 of which were placed as much as possible along the edges and 2 inside.

Figure 3.9 – Distribution of TPs (red dots in the circles) in the overlap area between images 615 and 618

The identification was carried out in Adobe Photoshop, by displaying the RGB images and by searching for suitable elements to be checked then in the corresponding Wallis filtered pictures. Furthermore, it was focused on areas with high concentration of texture considering, at the same time, the need of identifying points along edges.

Suitable TPs should be:

- clearly visible and recognizable in multi overlap areas;
- seen with similar angle of view in different images;
- placed on the ground;
- belonging to branches if can be found only at altitude (branches have geometry more stable and less subject to the wind);
- not placed on leaves, bushes and, in general, on all those objects that can easily change their position and orientation in two consecutive images, because of the wind;
- inside shadows but not on the edges, on account of their obviously changeable shape.

It must be borne in mind that finding TPs in wooded regions is usually far from simple and this time, unfortunately, was not an exception for several reasons:

1) there were portions with only trees so that the ground was not visible and some points were found at altitude;

Figure 3.10 – TPs on a branch and on the ground (on the right)

2) the different angles of view made difficult to find TPs especially in multi overlap areas;

Figure 3.11 – Different angles of view between images 628 and 630

3) the wind moved leaves and branches and created blur's effects with loss of details, compounded also by the presence of long shadows.

A total of 71 TPs were identified, only 20 of which were distributed in multi overlap areas.

3.3.2 GCPs AND TPs MATCHING

The matching step was performed using “pvd”, a not commercial program developed by a Ph.D. student at ETHZ-IGP: it runs on Sun Solaris and requires, as input, 8-bit single channel (or panchromatic) images in tiff format (without compression). It allows viewing images, measuring manually image coordinates and applying LSM, with multi–images and with/without geometric constraints. A special version of the program for SPOT image matching with geometric constraints is also available.

The Least Square Matching makes use of gray values differences in homologous areas belonging to different images, called “target” and “search” image.

A) *GCPs*: the target image was a sort of “template” containing regular circles of different sizes, white on black background or vice versa; the original green channels (e.g. 615_G.tiff) were instead, from time to time, the search image.

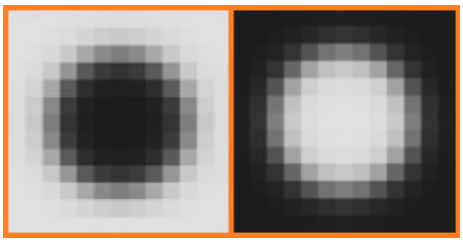

Figure 3.12 – Ideal signalized target: on the right, the selected one

The dimension of signalized GCPs was measured on a picture for choosing a corresponding target, that is, a white circle on black background with 15 pixels as diameter (see figure 3.12).

Hence, the parameter “Patch size” was set equal to a window of 21 x 21 (i.e. the above circle, surrounded by an edge of 3 pixels), whereas as “Transformation” was adopted a composition of affine transformations: two shifts, two scales and only one shear because the circular shape didn’t allow knowing information on the rotation.
Then, inserted the exact coordinates of the target circle’s center, the cursor was placed roughly on the GCP one finding out its image coordinates by means of the command “match” (with sub pixel precision).

B) *TPs*: the matching procedure was basically the same but made, from time to time, on pairs of filtered images (for instance W615_G.tiff), considering the first as target and the second as “search image”.
The “Patch size” changed for each point, going from 15 x 15 (flat terrain or slightly sloping) to 11 x 11 pixels: when the TP is on a branch, in fact, the larger the mask

dimension, the bigger the mixture of information coming from the tree and from the background. In these cases, it happened that the automatic matching failed and the procedure was performed manually; furthermore, a window smaller than 9 by 9 has never been employed since it's usually difficult that all the 6 parameters of the affine transformations are found.

The Least Squares normal matrix is computed as average of "template" values and "search image" ones, with subsequent smoothing of the differences.

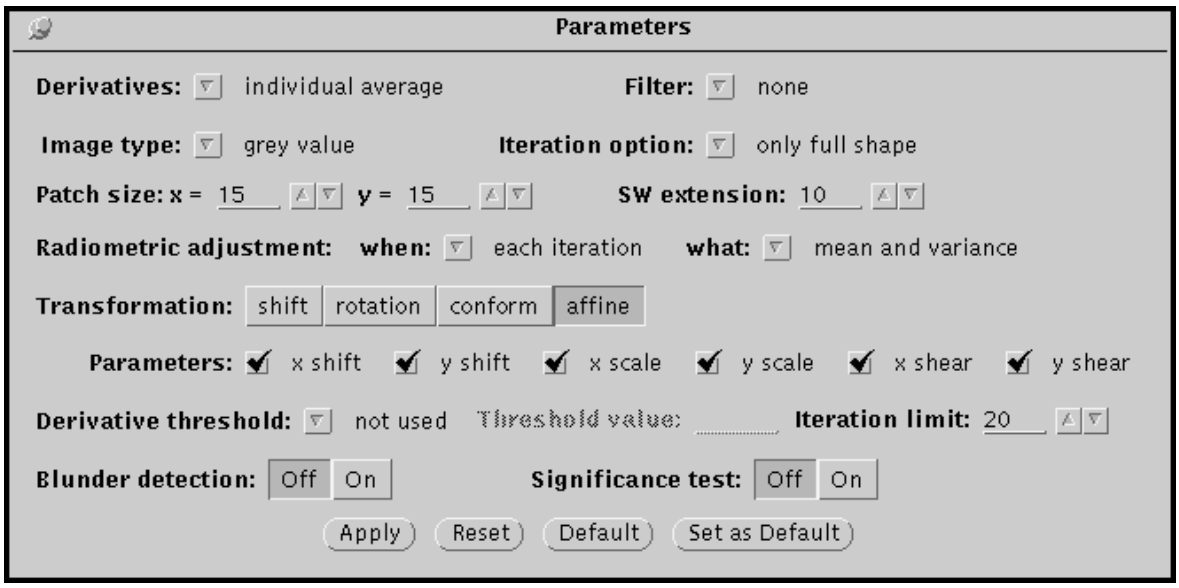

Sometimes the result of the affine transformation was not satisfactory: therefore, for reduced patch, the conform one was applied.

Figure 3.13 – Window in "pvd" for allowing the tuning of parameters

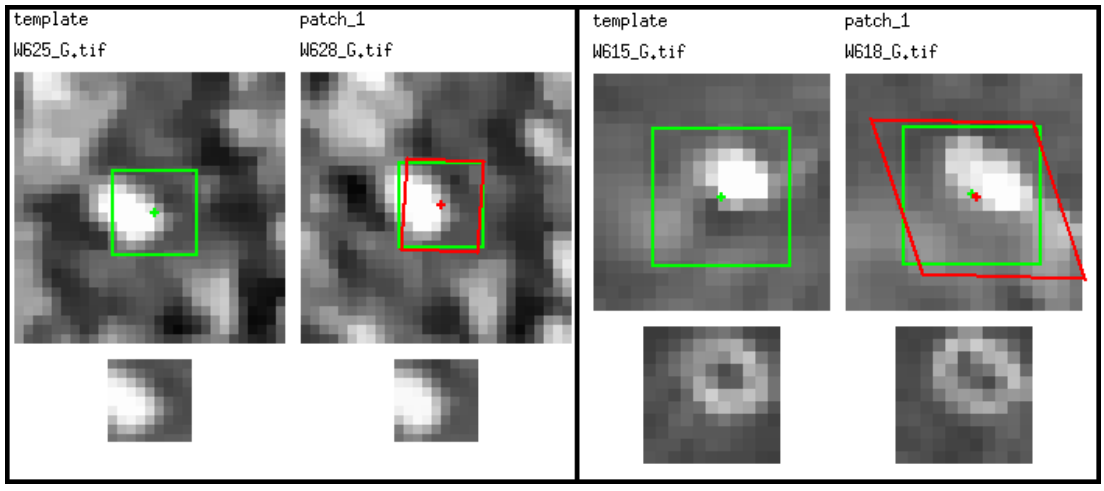

Figure 3.14 – Example of accepted matching on the left (affine, 9 by 9 mask) and rejected on the right (affine, 11 by 11) for two different TPs

The image coordinates of both GCPs and TPs were finally saved in .txt files and edited to be suitable for the software LPS: in particular, 0.5 was added to all the measured values since LPS places the origin of the reference system at the center of the upper left pixel.

3.4 IMAGE ORIENTATION

The main aim of Photogrammetry is the reconstruction of 3D objects from the use of 2D images: for achieving it, an essential requirement is to calculate through a precise mathematical model:

- the interior characteristics of the camera ⟹ interior orientation;
- the position of the images, at the acquisition time, with respect to the object to be modeled ⟹ exterior orientation.

3.4.1 INTERIOR ORIENTATION

The interior orientation defines the inner geometry of a camera/sensor as it existed at the time of data capture; the associated variables are:

a) THE PRINCIPAL POINT: it is mathematically defined as the intersection of the perpendicular line through the perspective center of the image plane. From an optical point of view, instead, it can be described as the image position where the optical axis intersects the image plane (see figure 3.15, a);

b) THE FOCAL LENGTH: it's the length from the principal point to the perspective center;

c) THE LENS DISTORTION: it deteriorates the positional accuracy of image points located on the image plane and occurs when light rays, passing through the lens, are bent, thereby changing directions and intersecting the image plane at positions deviant from the norm. There are two different types of distortions:

- radial: it causes image points to be distorted along radial lines from the principal point. Its effect is indicated as Δr (figure 3.15, b);
- tangential: it occurs at right angles to the radial lines from the principal point. Since its effect (Δt) is usually much smaller in magnitude than radial one, it's often considered negligible.

The effects of radial lens distortion throughout an image can be approximated by a polynomial, used to determine three coefficients:

$$\Delta r = k_0 r + k_1 r^3 + k_2 r^5$$

Once the coefficients are calculated, each measurement taken on an image is corrected for radial lens distortion.

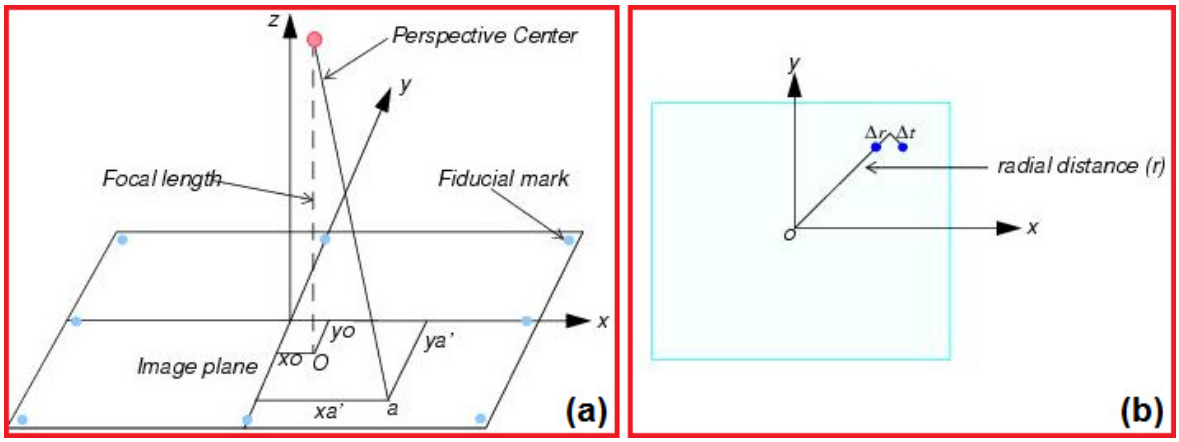

Figure 3.15 – Variables associated with the internal geometry of an image captured from an aerial camera, where *O* is the principal point and *a* is an image point. On the right, the difference between radial and tangential lens distortion

The variables, described above, are usually estimated during the so–called "camera calibration" procedure, performed in this project by using the software I–Witness.

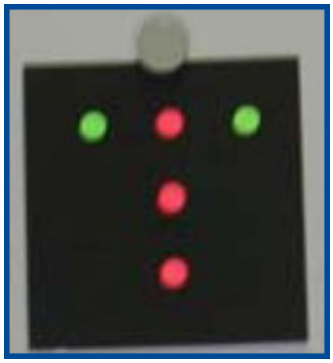

It requires, as input, images referring to scenes created in laboratory and usually composed by small coded targets (figure 3.16). The recognition of homologous points in different pictures is automatic and then a bundle adjustment with self–calibration is run, supplying at the end the calibration parameters.

Figure 3.16 – Calibration target

For performing the image orientation, a new project was created with LPS, going to set some necessary properties such as:

- the reference coordinate system (see section 3.1);
- the rotation system (ω, φ, κ), with degree as angle unit;
- the photo direction (z–axis for normal images);

- the average flying height (60 m);
- the type of sensor (digital non metric camera).

After adding the original images, pyramids were generated in order to work with hierarchical data and the camera parameters, assessed with I–Witness, were inserted to realize the interior orientation.

PANASONIC LUMIX DMC – FX35	
Focal length	4.3968 mm
Principal point X_0	0.0078 mm
Principal point Y_0	0.0414
k_0	-1.0888 e $^{-03}$
K_1	3.6922 e $^{-04}$
K_2	-1.2841 e $^{-05}$
Pixel size in x and y directions	1.62 μm

Table 3.4 – Parameters for the interior orientation: all, except the last one, were estimated by I–Witness

3.4.2 EXTERIOR ORIENTATION

The exterior orientation consists of 6 parameters which describe the spatial position and the orientation of the camera's reference frame compared to the object global reference one:

- the position, in the object space, of the projection center $\Longrightarrow$ $[X_S, Y_S, Z_S]$
- the rotation matrix R, result of three independent rotations:
  1) ω around X axis (roll);
  2) φ around Y_ω axis (pitch);
  3) κ around $Z_{\omega\varphi}$ axis (yaw).

The most widespread mathematical model is called "Bundle Block Adjustment" (BBA): it rests on the well–known collinearity equations which permit estimating the exterior orientation parameters, associated with each image in the block, and the coordinates (X, Y, Z) of TPs.

It must be noted that the BBA is of course implemented in LPS to perform aerial triangulation, with the additional possibility to recover the interior orientation parameters associated with the camera, using a self–calibrating bundle adjustment.

Therefore, GCPs and TPs coordinates (both image and object ones for the former, and only image ones for the latter) were loaded in the LPS project.

A first BBA gave a Root Mean Squared Error (RMSE) quite high (roughly 8 pixels) as well as several large residuals of image points; furthermore, the position of the projection center in the object space (X_S, Y_S, Z_S) was estimated as exactly equal for the two last images (630 and 632), indicating that something wrong happened.

The exterior orientation parameters

image ID	Xs	Ys	Zs	OMEGA	PHI	KAPPA
7	78799.5401	46062.2597	752.6772	2.1661	18.2825	-58.7034
8	78799.5401	46062.2597	752.6772	7.0990	7.9864	-56.5550
3	78737.7018	46034.8937	751.5812	4.9197	13.4393	-58.5451
4	78756.2270	46041.8928	752.3894	8.6618	15.2479	-60.3822
5	78766.9033	46043.9919	752.1844	5.3494	9.9073	-64.8443
6	78774.7920	46045.6601	753.1986	2.6621	12.9513	-54.1817
2	78727.0206	46031.8708	750.9026	10.9847	13.0852	-58.7005
1	78705.3416	46021.2606	751.3647	6.7549	6.1447	-54.9731

Point	Image	Vx	Vy	Point	Image	Vx	Vy
63	7	123.107	275.968	65	7	144.793	-96.301
63	8	-250.064	-627.367	65	8	-105.128	62.804

Point	Image	Vx	Vy	Point	Image	Vx	Vy
64	7	133.470	-647.296	66	7	73.984	-14.064
64	8	-81.694	302.013	66	8	-55.885	10.247

Figure 3.17 – Extract of the BBA report: at the top, the exterior orientation parameters with the position of the projection center in the red rectangle; at the bottom some huge residuals of image points in the last two images (ID 7 and 8 stand for 630 and 632)

Since the selection of TPs in these two images was very difficult, mainly due to the fact that the 630 was really blurred, it was decided to try a new BBA leaving out the 632 and bringing the total number of GCPs to three (in fact, the GCP 3 was visible only in the last picture); afterwards, another run was done without both 630 and 632 in order to compare the results and understand the influence of the images. Moreover, some settings were refined too:

a) *Image point standard deviations (pixel)*: 0.75 for both X and Y ⟹ during the iterative aerial triangulation process, the image coordinates (X, Y) are allowed to fluctuate within the limits of the specified standard deviations: larger values indicate poor image measurements and vice versa;

b) *GCPs type and standard deviations (X, Y, Z: meters)*: X, Y = 0.05 m; Z = 0.10 m ⟹ this property permits to define the type of GCPs weighting technique and the corresponding statistical weights. Applying statistical weights means that GCPs positions are allowed to fluctuate within the limits of their specified standard

deviations during the iterations (larger values indicate poor measurements and vice versa).

Indeed, it must be borne in mind that the use of statistical weights assists in minimizing and distributing data error throughout the block of imagery, thereby ensuring highly accurate results (in the first BBA, instead, the option "fixed values" was applied).

It's a global precision indicator describing the quality of the entire solution.

BBA – 7 IMAGES AND 3 GCPS	
Total Image RMSE	1.2750
GCPs RMSE: Ground X	0.0393
GCPs RMSE: Ground Y	0.0841
GCPs RMSE: Ground Z	0.0171
GCPs RMSE: Image X	0.2883
GCPs RMSE: Image Y	0.5293

Table 3.5 – RMSEs for the bundle block adjustment performed on 7 images with 3 GCPs

Since the two final reports did not differ too much in improving the results, it was decided to choose the solution that would allow to keep the largest possible number of images (namely 7 in total, rejecting only the 632).

Figure 3.18 – Variation of the Z coordinate, which increases with the distance from the central GCP (in green)

Moreover, as mentioned in 3.1, a considerable problem was constituted by the alignment of the GCPs in the center of the image, along the road: this means that the rotation ω along the X axis (roll) could vary, influencing the Z coordinates, in particular of all the points near the images' edges.

Hence, it was decided to add "new" GCPs: some particular TPs, distributed near the strip's edges and in multi overlap areas, were identified; then, inside this group, residuals and accuracy of their object coordinates (estimated in the last BBA) were carefully checked to select the best ones. At the end, 5 TPs (ID: 9/10/19/46/59) were chosen to become GCPs with the purpose to stabilize ω.

A new bundle block adjustment was therefore run on the 7 images, with 8 GCPs (3 original + 5 "new") and the same settings as previous: figure 3.19 shows the improvements reached, even if the total RMSE remained bigger than 1 pixel (1.1539).

The accuracy of the exterior orientation parameters

image ID	mOMEGA	mPHI	mKAPPA
7	2.4188	0.5841	0.2717
3	2.4682	0.5454	0.2318
4	2.4562	0.5701	0.2089
5	2.4603	0.5785	0.2326
6	2.4396	0.5710	0.2594
2	2.4827	0.5538	0.1861
1	2.4965	0.5598	0.2202

image ID	mOMEGA	mPHI	mKAPPA
7	0.4309	0.2164	0.0824
3	0.4286	0.1966	0.0682
4	0.4361	0.1838	0.0617
5	0.4302	0.1952	0.0635
6	0.4454	0.1792	0.0647
2	0.4522	0.1798	0.0659
1	0.4523	0.2197	0.0769

The accuracy of object points

Point ID	mX	mY	mZ
9	0.1129	0.2119	0.6959
10	0.0630	0.0572	0.3035
11	0.0632	0.0597	0.2561
12	0.1572	0.1295	1.7005
13	0.1779	0.2549	1.4688
14	0.2081	0.1491	0.6105
15	0.2499	0.1034	0.3810
16	0.5202	0.2108	1.6258
17	0.1729	0.1558	1.5018

Point ID	mX	mY	mZ
7	0.0509	0.0501	0.1307
8	0.0560	0.0787	0.1934
11	0.0428	0.0418	0.1431
12	0.0833	0.1031	0.3766
13	0.1185	0.2204	0.3470
14	0.1743	0.1262	0.3022
15	0.2151	0.0845	0.3243
16	0.4505	0.1689	0.5642
17	0.1219	0.1281	0.3992

Figure 3.19 – BBA with 3 GCPs on the left: the large values of ω, higher than φ and κ ones, have corresponding influence on the Z coordinate. Even if this effect remains, it's much reduced doing the BBA with 8 GCPs (on the right)

Finally, the image coordinates of the TPs with the biggest residuals were estimated again in "pvd", without leading to better results; these were not achieved even performing the orientation with ORIMA (Orientation Management software, from Leica Geosystem).

The last option was the use of BINGO (a program system for close range Photogrammetry and aerial triangulation), always on 7 images (from 615 to 630) and with 8 GCPs.

Remembering that 1 squared pixel has 1.62 μm as side, a value of 1.59 μm as final sigma means roughly 0.9815 pixels.

Although it was hoped to get an even better result, this image (internal and external) orientation was considered enough satisfactory, keeping also in mind that the starting data set was not optimal and composed by a single strip with aligned GCPs (aspect that, for sure, created some problems).

3.5 HIGH RESOLUTION DSM

Once the image orientation was performed, it was possible to proceed to the creation of a high resolution DSM through the not commercial software “SAT-PP”, designed and developed by ETHZ-IGP.

3.5.1 SAT-PP AND THE ORIENTATION FILES

The main component of the software package SAT-PP (Satellite Image Precision Processing) is a precise, robust and automated matching algorithm for the generation of DSMs: a multi–image Least Squares Matching (LSM) for image features like points and lines.

The approach uses a coarse-to-fine hierarchical solution with an effective combination of several image matching methods and automatic quality control (Wolff & Gruen, 2007). The matcher was originally created to process data collected by linear sensors of high-resolution satellites (IKONOS, QuickBird, SPOT 5, Cartosat-1), but it was subsequently modified to be also suitable for images of aerial or terrestrial Photogrammetry. More technical information can be found in Baltsavias et al. (2005) and Gruen et al. (2005).

The software requires in input some text files (*.ori*), one for each image: they have a fixed structure, containing internal and external orientation parameters.

Principal point coordinates

and focal length

Coefficients of the affine

n from file to film

sition, in the object

ce, of the projection

ter

```
3
0          0                4.3968
-2.9541    0.001620         0.000000
 2.2153    0.000000        -0.001620
0
678705.909        246033.599        752.397
0.55846528        0.821459893       0.115413068
-0.829296627      0.549594324       0.101060291
0.019586609       -0.152150332      0.988163267
```

Figure 3.20 – Example of orientation file

Rotation matrix (3 x 3), computed from the three angles (ω, φ, κ) in radiant

3.5.2 EPIPOLAR IMAGES

The 7 Wallis filtered green channels (W615_G – W630_G, see 3.2.3), in the "raw" format, were added to a new project with the orientation files; the following properties were selected:

- Image type: aerial digital camera;
- Average terrain: 700 m (see section 2.1);
- Grid space for DTM: 0.08 m (1.5 - 2 million points).

In order to facilitate the matching, SAT-PP is able to generate automatically epipolar images, i.e. stereo pairs: they are two images of the same area, taken from different points of view and re-projected so that they are on the same plane with their axes parallel. In this way the homologous points are aligned along the same axis, as represented in figure 3.21.

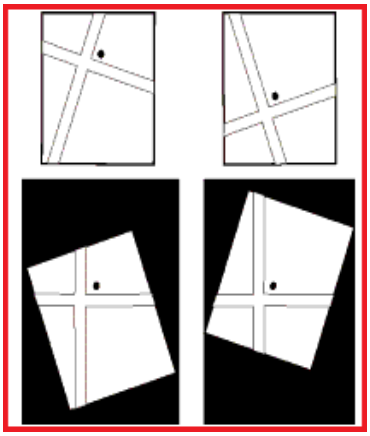

Figure 3.21 – Original images at the top and, below, the epipolar ones

The needed epipolar image parameters were only the minimum and the maximum heights of the imaging area, whereas the option "mass points (feature points + regular spacing points") was set as matching parameter.

Because of the still too large parallax between pictures 628 and 630, the latter had to be removed: therefore five epipolar images were created, on which measuring some homologous points (called "seed points"). Even if they represent a starting approximation, it's appropriate to choose them carefully: that is, mainly points on the ground and well–distributed on the overlap areas (from 8 to 14 for each stereo pairs).

Then the so initialized matching procedure was run with the following selections:

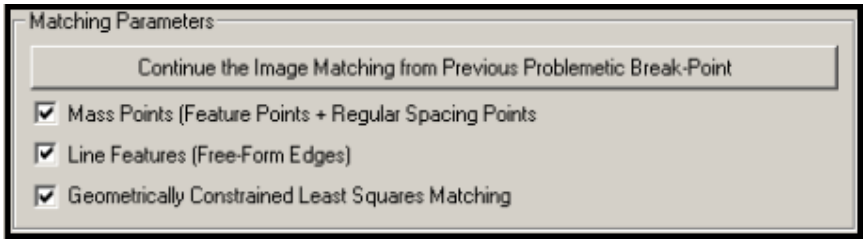

Figure 3.22 – Matching parameters selected for the DSM generation

The majority of homologous points were identified in the road's surroundings and, in general, the results were considered satisfactory with the exception of the pair 625 – 628 (with only few points belonging to it). The orientation files were rechecked and the matching redone with more initial seed points, but all these operations didn't lead to any improvements: hence, also the image 628 had to be removed.

3.5.3 DSM GENERATION

After a visual inspection of the matching result, all was ready for the DSM generation (i.e. a digital representation of the earth surface, which includes vegetation as well as artificial features such as roads and buildings) by using five of the original eight images (from 615 to 625) and 0.08 m as grid spacing (see figure 3.22 for more options).
First, it must be noted that the DSM represented a surface's portion smaller than that initially considered, obviously due to the reduction in the images number; the heights varied between 693 m and 709 m, in agreement with the altitude values of the testing area (see section 2.1).

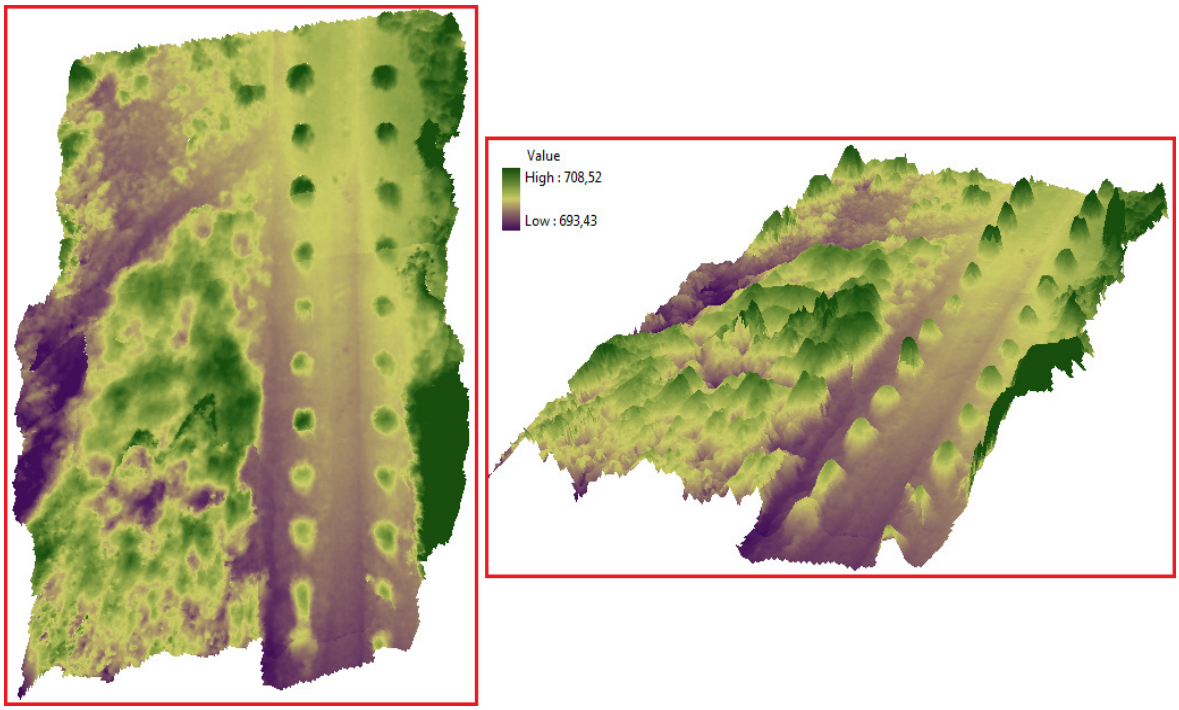

Figure 3.23 – Overview of the DSM: from on high and sideways (on the right)

The analysis can be subdivided into the separate treatment of the different modeled elements:

* FLAT SURFACES: it seems there are no big problems in the reproduction of flat surfaces such as the well–known road (slightly sloping) and a small path on the left; however, it must be remembered that the SAT-PP matching picked out a greater number of homologous points near the road than elsewhere. Besides the latter, the path descending to the left ends in a small clearing with grass and bushes: this irregular surface was sufficiently reconstructed even if discontinuities and higher elements were smoothed;

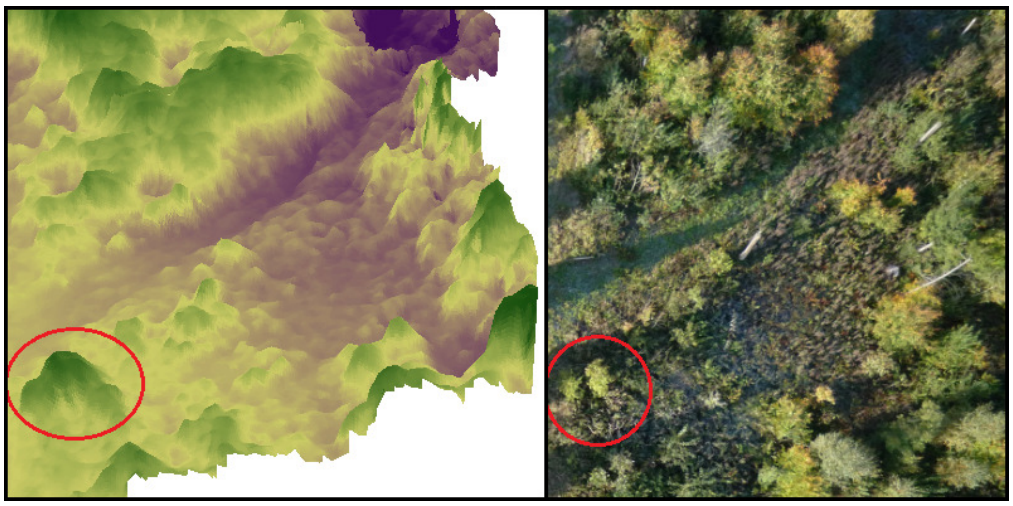

Figure 3.24 – The clearing with shrubs and grass: in the circle, a bigger smoothed bush

* COMPLEX SURFACES: namely, the wooded regions on the left and on the right side of the road. Actually, the latter is almost completely missing with the exception of a thin strip, characterized by solitary and taller trees/bushes: since the portion was visible in the images with different widths, it was normal that the resulting overlap area was a reduction of the original one. Moreover, only few homologous points were identified on it by the SAT–PP matcher, due to blur's effects and the fact that the algorithm has a less correlation's capacity near the edges. For this reason, outliers can be here identified (see figure 3.25, a).

  On the left side, instead, a more wooded homogeneous (for trees' height and continuity) part was modeled, although a small worsening of the canopy can be noted because of the reduction of the trees' volume and height. Furthermore, near a wide ground area (small in reality), some taller trees were represented

with a sharpened shape (the presence of a discontinuity between overlap areas can have contributed);

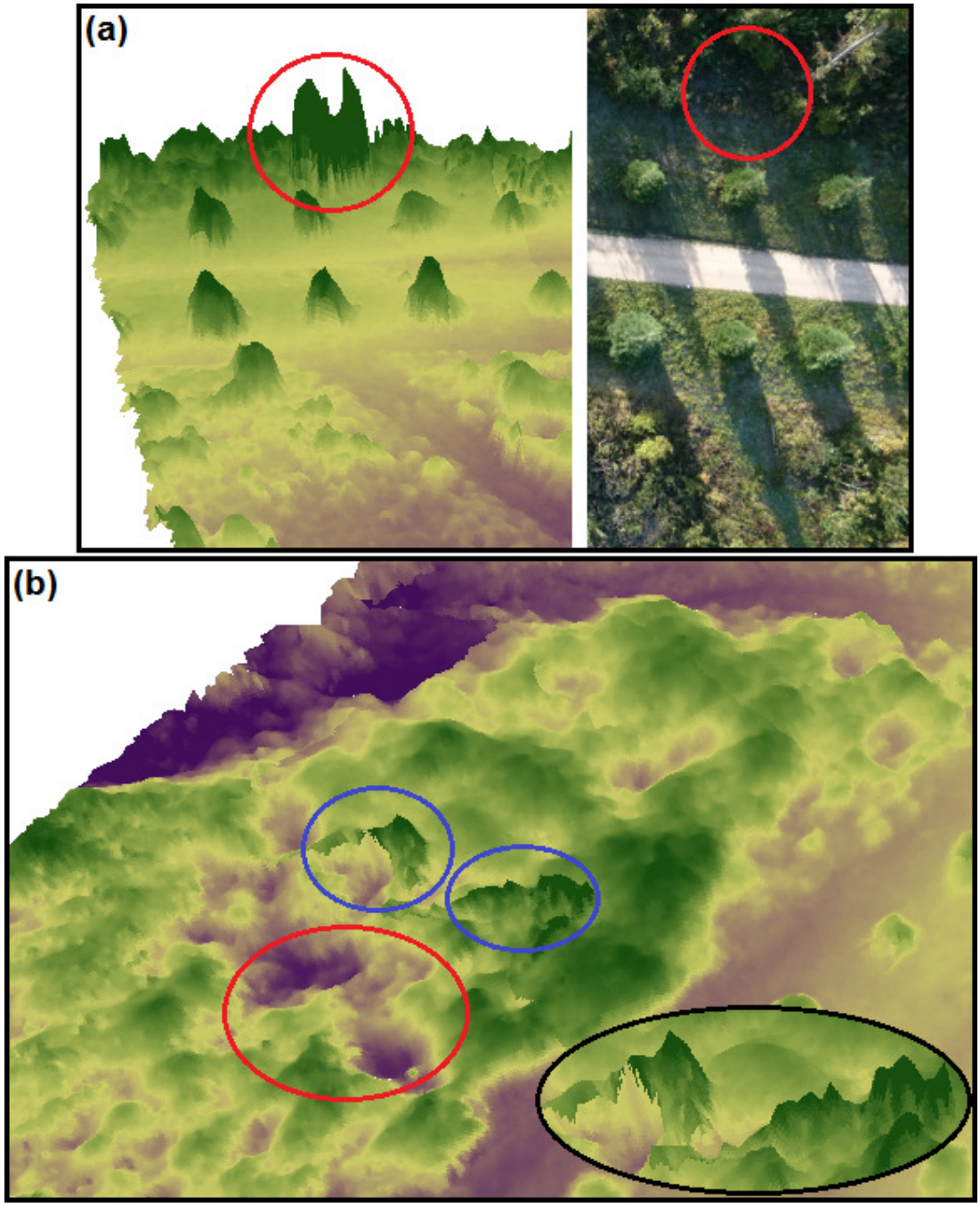

Figure 3.25 – (a) area on the right side of the road: it's possible to see the presence of an outlier, since there's a tall element not corresponding to anything in the image.
(b) region on the left side of the road: the small ground area is highlighted in the red circle while the blue ones surround the sharpened trees (see black oval for more details)

* SINGLE OBJECTS: the small pine trees were well identified on the sides of the road; nevertheless, some aspects should be outlined: the two pine trees (in the red oval) were represented as a single entity in the DSM because, in the image, of the first appeared above the one due to the viewpoint. In , on the other side of the road, a e was modeled together with the one close to it. Lastly, the junctions overlap areas affected the modeling of trees with discontinuities as well as already mentioned above.

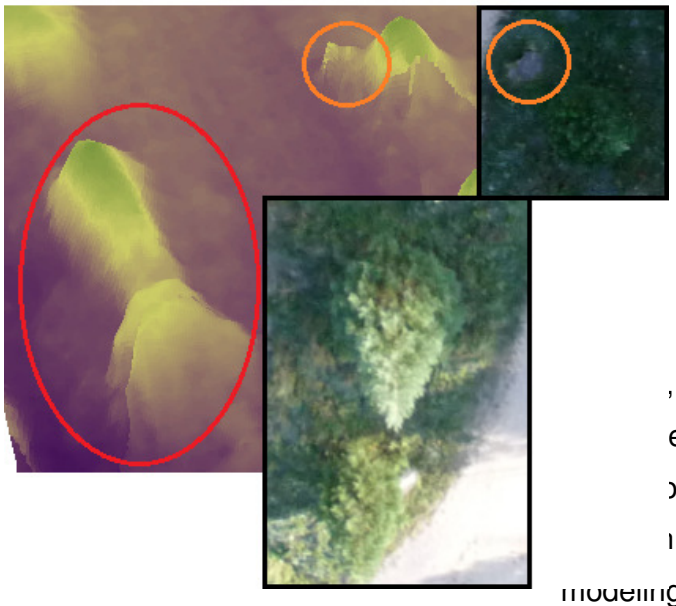

Figure 3.26 – Errors in the modeling of the pine trees

A general smoothing of the pines' shape can be also observed.

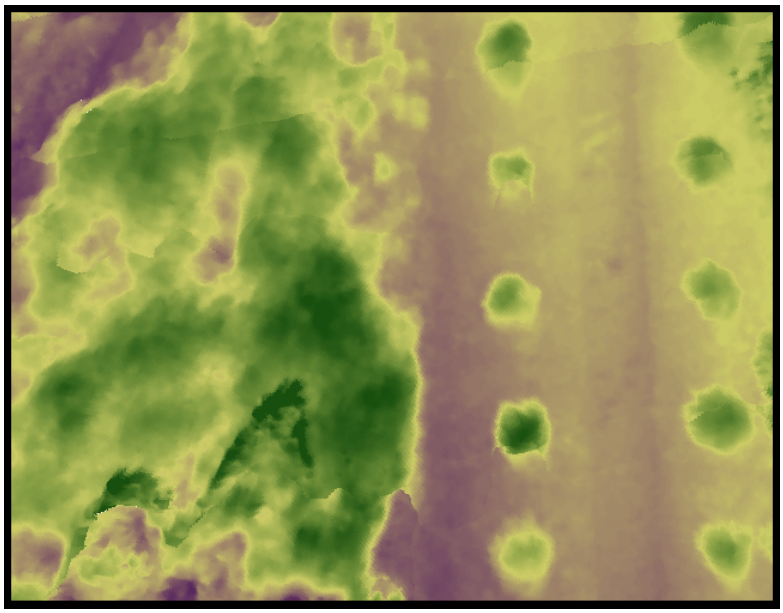

Figure 3.27 – Discontinuities that affected the modeling

Therefore, it's possible to say that UAV images allow the generation of high resolution DSMs, in which different elements, such as flat and complex surfaces or single objects, are detected and separated; furthermore, they're also modeled taking into account small features.

Despite this, there are still some problems associated with the presence of outliers and blunders: however, the lack of matching points in the overlap areas can be improved through the use of a better starting dataset, less affected by blur, long shadows and wind's effects, that is, all those aspects that lead to a loss of texture.

These factors are not negligible, for sure, when considering a DSM for a forestry purpose, context in which the smoothing and the reduction of canopy are significant: let's consider, for instance, the generation of a Canopy Height Model (having a corresponding updated DTM) suitable for tree height and growth estimation and for evaluating the available biomass. Thus, it can be said that UAVs will play a key role especially by allowing frequent observations and monitoring: in addition, from their images it's possible to generate high resolution orthophotos too. These, in presence of NIR data, could improve the study of the vegetative age and state, beyond the species classification.

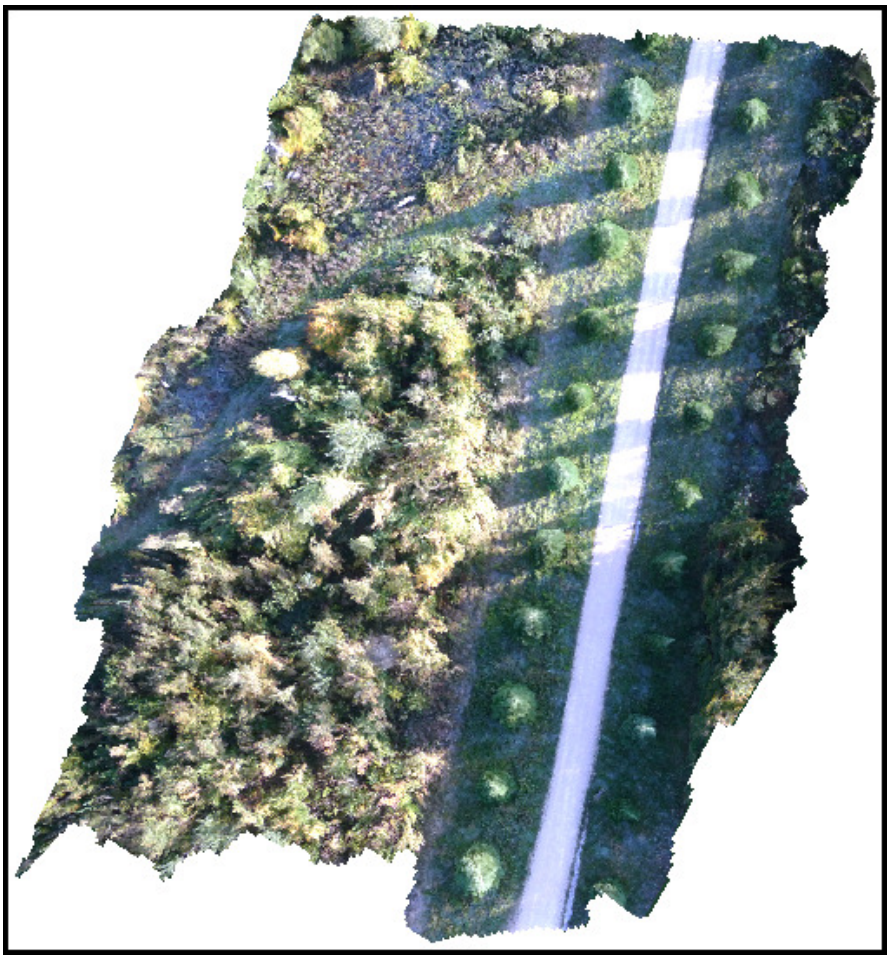

Figure 3.28 – Mosaicing of the orthophotos generated by the DSM: outliers and blur's effects are especially present at the edges

3.6 COMPARISON WITH STANDARD DSMs

The final step of this first project part was the comparison between the just generated DSM and the standard ones, i.e. those produced by Aerial Photogrammetry with the ADS40 sensor and the LiDAR system, whose main characteristics are listed below (for more information, see subsections 2.4.1 and 2.4.2). This procedure was performed to understand the reliability of a DSM produced by UAV images in addition to the visual analysis described above.

DSM	RESOLUTION	DATE OF FLIGHT	LEAVES
DSM_UAV	0.08 m	October 2009	Leaves-on
DSM_ADS40	0.50 m	January 2009	Leaves-off
DSM_LiDAR	0.50 m	March 2002/2003	Leaves-off

Table 3.6 – Summary of the main DSMs characteristics

The three DSMs were co-registered using the semi commercial program LS3D (Gruen & Atka, 2005): in fact, "Least Squares 3D" allows to match a 3D surface (slave) to a master one, possibly with different point density and accuracy. The slave is transformed by a seven parameters 3D similarity transformation estimated using the generalized Gauss–Markoff model, minimizing the sum of the squares of the Euclidean distances between the surfaces (Freeman et al., 2008). After the transformation of the slave point cloud, the standard deviation of the remaining distance differences is estimated (sigma-naught) as quality measure, and it's decomposed in X, Y and Z components. The residuals can also be decomposed in X, Y, Z components (Baltsavias et al., 2008).

The standard DSMs were cut so that only the area of interest was processed (hence, reducing the computational weight) and then they were converted in *.ascii*.

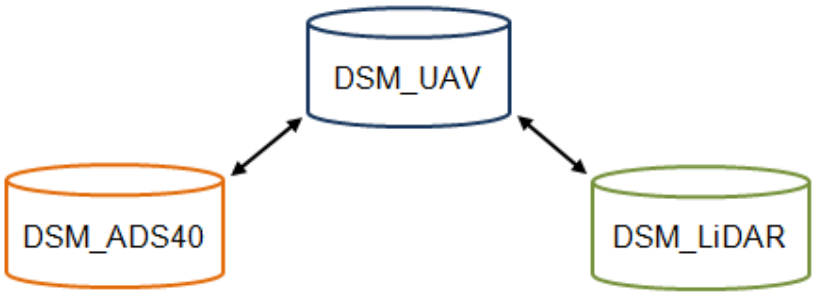

Figure 3.29 – Outline of the comparison procedure

3.6.1 COMPARISON ON THE ENTIRE AREA

A first comparison was performed on the entire area of analysis, considering the DSM_UAV as master and the others as slave:

COMPARISON	A PRIORI σ_0 [m]	A POSTERIORI σ_0 [m]
DSM_UAV – DSM_ADS40	0.05	0.90
DSM_UAV – DSM_LiDAR	0.05	1.09

Table 3.7 – A priori and a posteriori standard deviations

The a posteriori standard deviations reveal very high values, possibly connected with the problems encountered in the image orientation (see section 3.6). Some statistics were then computed on the residuals obtained: please note that negative residuals indicate that the values of the master are greater than the slaves' ones.

	DSM_UAV – DSM_ ADS40				DSM_UAV – DSM_LiDAR			
[m]	EUCLID. DISTANCE	X RES.	Y RES.	Z RES.	EUCLID. DISTANCE	X RES.	Y RES.	Z RES.
Mean	-0.1353	$-9.2006\ 10^{-4}$	-0.0117	-0.1024	-0.9567	0.0090	-0.0403	-0.8764
St. Dev.	0.9987	0.3110	0.4032	0.8636	1.9605	0.4374	0.5551	1.8680
Max.	4.2458	3.4697	3.6952	4.2458	6.2235	6.7391	6.1712	3.5690
Min.	-4.5942	-3.7231	-3.5680	-4.5942	-8.5209	-8.4026	-5.2467	-8.5209
mAD	0.8145	0.1045	0.1674	0.6485	1.6398	0.1078	0.2178	1.5354
MAD	0.7000	0	0	0.4800	1.2909	0	0	1.0311

Table 3.8 – Statistics concerning the Euclidean distance and the X, Y, Z components of the residuals

Where, using the data set $\{x_1, x_2, \dots, x_n\}$:

- the *mean absolute deviation* (mAD) is the average of the absolute deviations from the data's mean (m(X)); it's a summary statistic of the dispersion;

$$\frac{1}{n}\sum_{i=1}^{n}|x_i - m(X)|$$

- the *median absolute deviation* (MAD) is the median of the absolute deviations from the data's median; it's a robust statistic, being more resilient to outliers in

the data set than the standard deviation (on which outliers can have high influence since large deviations are usually weighted more heavily). In this statistic, instead, the magnitude of the distances of a small number of outliers is irrelevant.

$$median_i\left(\left|x_i - median_j(x_i)\right|\right)$$

What was stated above is easily verified by the fact that the MAD values are substantially lower than the corresponding standard deviations. Hence, let's consider them and the mAD ones, concerning the Z residuals, in table 3.8: it's possible to note how they are lower than one meter (for the comparison with the DSM_ADS40) but definitely higher for the DSM_LiDAR, while the mean values show the presence of a differences' trend equal to 10 cm for ADS40 and, again, near to 1 m for the LiDAR. The situation doesn't improve looking at the minimum and maximum values.

This doesn't seem very satisfactory… but, before drawing conclusions, it's better to take into account some elements:

- the LiDAR flight was performed in 2002 (and a second one a year later), thus a difference of 6/7 years exists with UAV data: surely trees' height variation has to be kept in mind, referring to normal growing as well as forestry management (e.g. the cutting down). Furthermore, it should be remembered that canopy penetration with laser could be happened;
- in a previous study on the same area (Kerdsrilek, 2010), the comparison between LiDAR and ADS_40 DSMs was carried out, highlighting the presence of scattered blunders in the first one: although the mean value was low (-0.88 m), there were gaps roughly equal to $\pm 25\ m$ (figure 3.30).

Beyond these, it must be said that in general a quantitative comparison is not so reliable when the time difference is so high.

Hence, surely the comparison with the DSM_ADS40 should be more trustworthy and the trees variations can be linked to seasonal changes.

Finally, it's better to not underestimate the problems encountered during the image orientation phase, namely, the "free" rotation along the X axis that affected the Z points coordinates. A background tendency of this type could be recognized in figure 3.31, with the road's heights of the slave (DSM_ADS40) usually greater than those of the master (DSM_UAV). **

** A complete overview of the residuals (X, Y, Euclidean distance) can be found in Appendix A

It was therefore decided to make the comparison only on the central road where it's supposable that the rotation was negligible: the resulting values should be more reliable.

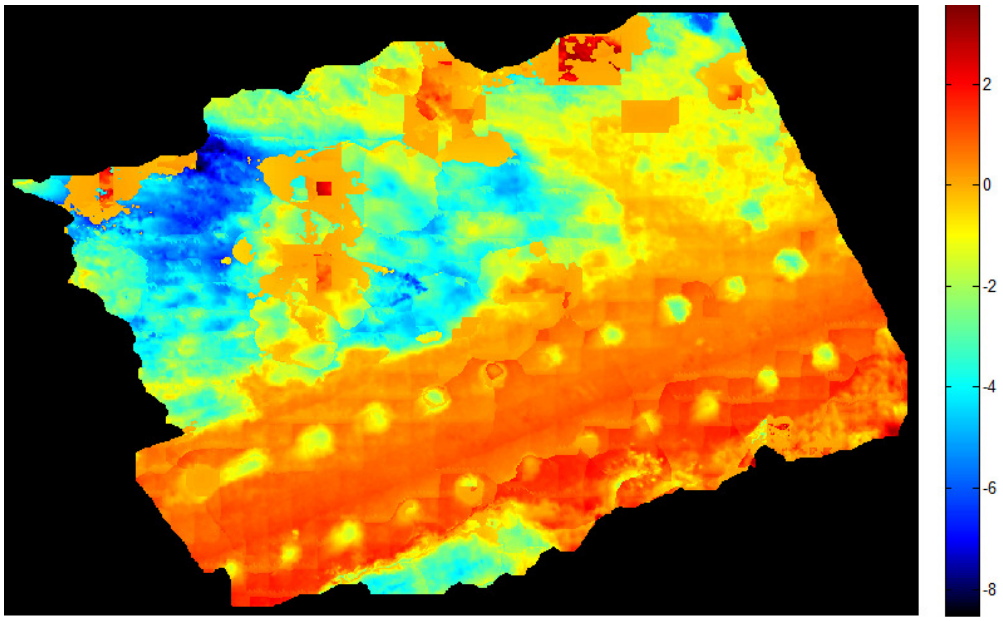

Figure 3.30 – Comparison between DSM_UAV and DSM_LiDAR: the Z residuals; the black ovals surround some evident blunders

It has to be remember that negative residuals indicate that the master values are greater than the slaves' ones.

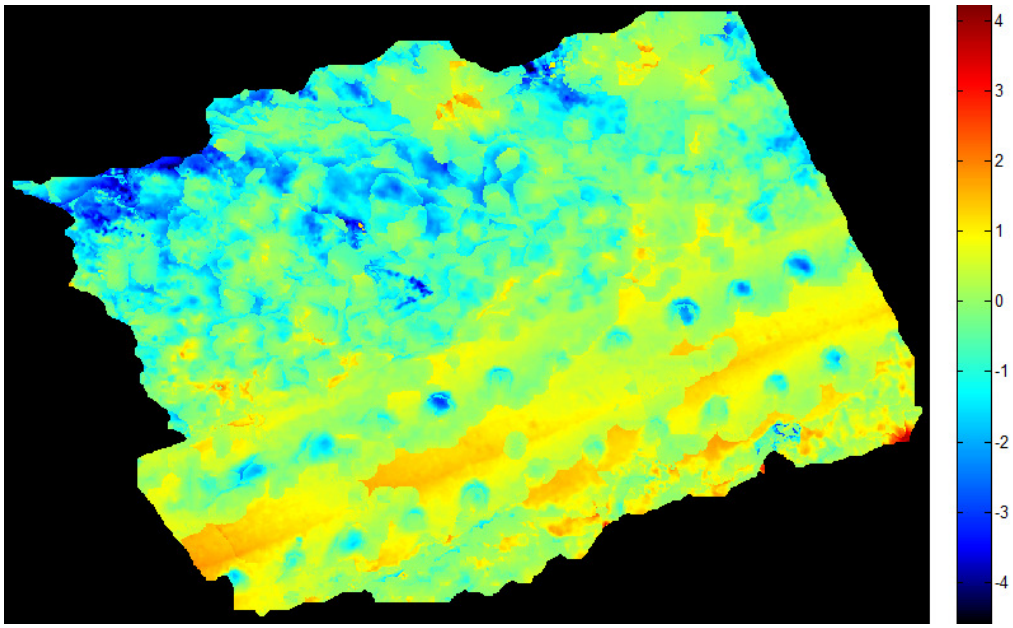

Figure 3.31 – Comparison between DSM_UAV and DSM_ADS40: the Z residuals

3.6.2 COMPARISON ON THE ROAD

LS3D was again employed for the co–registration, with the DSM_UAV as master and the other two as slave:

COMPARISON	A PRIORI σ_0 [m]	A POSTERIORI σ_0 [m]
DSM_UAV – DSM_ADS40	0.05	0.07
DSM_UAV – DSM_LiDAR	0.05	0.51

Table 3.9 – A priori and a posteriori standard deviations

Remembering the previous values (see table 3.7), it's easy to note the improvement; for what concerns the statistics:

	DSM_UAV – DSM_ ADS40				DSM_UAV – DSM_LiDAR			
[m]	EUCLID. DISTANCE	X RES.	Y RES.	Z RES.	EUCLID. DISTANCE	X RES.	Y RES.	Z RES.
Mean	-3.2511 10^{-6}	4.2425 10^{-5}	1.2904 10^{-4}	-2.7604 10^{-4}	0.0787	0.0013	0.0013	-0.0053
St. Dev.	0.0701	0.0051	0.0127	0.0687	0.4866	0.1946	0.2118	0.4002
Max.	0.1865	0.0287	0.0816	0.1865	1.3095	1.0409	0.9931	1.2192
Min.	-0.2255	-0.0422	-0.0604	-0.2255	-0.8769	-0.9512	-0.6733	-0.8768
mAD	0.0563	0.0014	0.0046	0.0550	0.4083	0.0875	0.1317	0.2745
MAD	0.0463	0	0	0.0452	0.3336	0	0.0546	0.1748

Table 3.10 – Statistics concerning the Euclidean distance and the X, Y, Z components of the residuals

Since the road didn't suffer big temporal changes, these results are more reliable than before; the DSM_LiDAR shows always bigger values than the DSM_ADS40 ones.
Looking at its Z residuals in particular, it's possible to note that, beyond the very low mean, the dispersion is less than the grid spacing of DSM_UAV (i.e. 0.08 m), considering both standard deviation and MAD (with and without influence of outliers).
Even if the dataset is not optimal with effects on the matching step, even if image orientation was affected by problems, even if the generated DSM presented some outliers and blunders, high resolution Digital Surface Models can be derived from UAV images, with enough reliability for forestry application. However, further studies are needed and these encouraging results should incentivize efforts in this direction.

PART 2

THE TREE CLASSIFICATION

TREE CLASSIFICATION CONTEXT

In this chapter, after a general introduction on the context of the forestry applications (with a particular attention to the Switzerland situation), a brief overview of some common classification algorithms is provided.

Forest ecosystems, as part of the landscape, represent an important natural resource: precise information on forest area, structure and composition may be helpful for different purposes such as inventories, protection tasks, management and environmental monitoring, playing also a key role in the discussion of carbon sinks.
Moreover, updated and accurate maps of tree species are a necessary input for biodiversity and biomass estimations and they are required by environmental agencies and land surveying offices to assess possible changes in their distribution or condition.

Classification of tree species was historically based on the interpretation and mapping of aerial photographs, employing different methods to identify the individual crowns. However, the development of digital devices, which are supposed to be both spectrally and radiometrically superior to the analogue cameras, and the subsequent diffusion of digital airborne data have promoted the exploration of new procedures and appropriate classification strategies. According to Jensen (2005), for example, these latter depend on different aspects such as the biophysical characteristics of the analysis area, the homogeneity of the remote sensing data and the “a priori” knowledge.
Several studies stress also the advantages of combining multi-resolution segmentation with object-based classification so that the information content of very high resolution images is fully exploited. The growing need of sensitive tools able to predict temporal and spatial patterns of tree species is associated with a parallel increasing usage of predictive spatial modeling, with which the vegetation cover may be reconstructed.

Although a great progress is still occurring in three-dimensional remote sensing (including stereo-photogrammetry, radar interferometry and LiDAR), one problem remains the fact that the definition of forestry parameters like area, structure and composition can change in the various European countries: what is considered as “forest” is indeed defined differently in the national inventories. The forest definition

adopted by Italy agrees with the one proposed by the Food and Agriculture Organization of the United Nations (FAO):

> «*Forest* is a minimum area of land of 0.05 - 1.0 hectares with tree crown cover (or equivalent stocking level) of more than 10 - 30 per cent, with trees with the potential to reach a minimum height of 2 - 5 meters at maturity in situ. A forest may consist either of closed forest formations where trees of various storeys and undergrowth cover a high proportion of the ground or open forest. Young natural stands and all plantations which have yet to reach a crown density of 10 - 30 per cent or tree height of 2 - 5 meters are included under forest, as are areas normally forming part of the forest area which are temporarily unstocked as a result of human intervention such as harvesting or natural causes but which are expected to revert to forest […]»
>
> *FCCC/CP/2001/13/Add.1*

For forest, Switzerland chose the following definition:

> «*Forest* is a minimum area of land of 0.0625 hectares with crown cover of at least 20% and a minimum width of 25 m. The minimum height of the dominant trees must be 3 m or have the potential to reach 3 m at maturity in situ»

Although orchards, parks, camping grounds, open tree formations in settlements, gardens, cemeteries, sports and parking fields may fulfill the (quantitative) forest definition, they are not considered as forests.

In Switzerland, it's possible to obtain:

d) DISCRETE FOREST MAPS: based on satellite images classification or aerial images interpretation, they are provided from "CORINE Land Cover", "Swiss Federal Statistical Office" and "Federal Office of Topography" (SWISSTOPO);

e) DATA BASED SAMPLE PLOTS: available at "National Forest Inventory" (NFI), they're based on field work and stereo-image interpretation;

f) MAPS OF FOREST DISTRICTS: only partly available, they're often out of date and therefore difficult to compare with other data sets.

It should be stated that actual, accurate and complete spatial data sets, which also include composition and structure, cannot be extracted for any Swiss region from the existing discrete forest maps; a possible alternative for obtaining those parameters

would be the interpolation of the NFI sample plots using statistical estimations. However, this would not resolve the problem of having incomplete spatial information.

MATERIAL

Before starting with detailed description on the work done, it should be remembered that this project is embedded in the Ph.D. thesis (still on–going) of Lars T. Waser, who aims at developing algorithms for semi–automated derivation of forest area and tree species composition, using high–resolution airborne remote sensing data. The algorithms should be robust and applicable for Swiss regions with different trees' characteristics: for this reason, three separated testing areas were selected since considered representative of the typical Swiss ecosystems.
Inserted in this context, starting from multispectral images, different types of input variables were derived: due to the fact that some of them could be correlated to each other and/or provide redundant information, a selection procedure was performed. Hence, the current work focused on finding the best variables' combination able to facilitate the separation of the trees' spectral signatures and to improve the subsequent classification.

Prior to the processing description, details of all the data received by Lars Waser (WSL) are provided in this chapter: from the chosen testing area to the selected tree species, from the initial data to the derived one.

5.1 ORIGINAL DATA

Among Üetliberg, Breitmoos and Tarasp, the first one was selected and assigned to this project by Waser since some tests had already been done on the other two.

5.1.1 STUDY AREA: ÜETLIBERG

Figure 5.1 – Image of the testing area: deciduous and coniferous trees

The study area is located in the Swiss central Plateau (roughly 47° 22' N and 8° 28' E) with extension of 7.6 km^2 and altitudes between 450 m and 850 m above the mean sea level (Canton of Zürich, Switzerland). Both flat and hilly terrains are present with mixed land cover such as forest, settlements and cropland: obviously, this project was interested only in the wooded part that covers roughly 3.5 km^2 and is mostly characterized by mixed forest with young conifers and deciduous trees (see figure 5.1).

5.1.2 STARTING DATA

Image data was acquired on August 18, 2008 using the sensor ADS40, type SH52, in the Red, Green, Blue, NIR (Near Infrared) and Panchromatic channels: a brief sensor's description can be found in subsection 2.4.1, whereas table 5.1 lists more technical information.

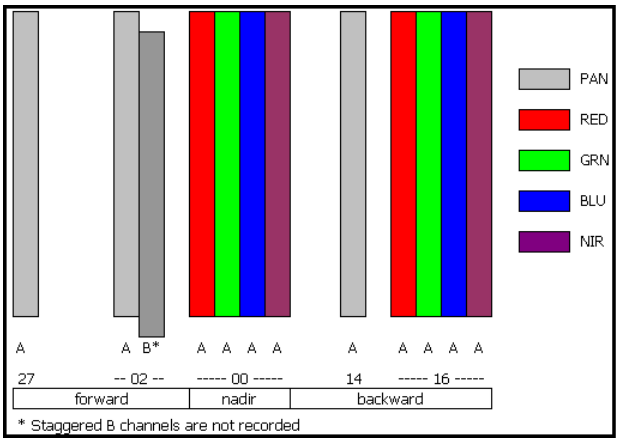

Figure 5.2 – Focal plate configuration of ADS40 SH52 (source: SWISSTOPO)

SENSOR ADS40 SH52	
Focal length	62.8 mm
Spectral resolution	Blue: 428 - 492 µm Green: 533 - 587 µm Red: 608 - 662 µm NIR: 833 - 887 µm Panchromatic: 465 - 680 µm
Radiometric resolution	11 bit 12000 pixels/array pixel size: 6.5 µm
Scale	~1:15000
Ground pixel size	~25 cm

Table 5.1 – Technical information on ADS40 SH52

Images were subjected to neither topographic nor atmospheric corrections because they can be assumed as negligible when working on small extensions (of course it's not true for a Swiss-wide classification, but this didn't concern the current project). Afterwards, starting from the 16° forward and nadir Color Infrared (CIR) ADS40 stereo images (all in the Swiss reference frame LV95), a DSM was generated with an "in-house" adapted and optimized strategy**: the "Ngate" module of the software "SocetSet 5.4.1" and a grid spacing equal to 0.5 m were used.

Orthophotos in two different channels combinations, RGB and CIR, were also produced through the mosaicing tool of "BAE Systems" SocetSet 5.4.1" and with a cell size equal to 0.25 m (see figure 5.4).

Figure 5.3 – Channels combinations: Red Green Blue (RGB) and Color Infrared (CIR)

Finally, it was employed a Swiss national LiDAR digital terrain model (DTM): LiDAR data was acquired by Swissphoto AG/TerraPoint, employing an ALTMS 2536 system with an average flight height above ground of 1200 m. A first flight was performed in March 2002 while a second one in March 2003 (leaves-off in both cases). Please, refer to subsection 2.4.2 for more information on LiDAR.

** All operations were carried out by the Ph.D. student Lars T. Waser (WSL)

Hence, the DTM was generated by SWISSTOPO with average density equal to 0.8 points/m^2 and height accuracy (1σ) of 0.5 m (Artuso et al., 2003); then, it was interpolated to a regular grid with spacing of 0.25 m.

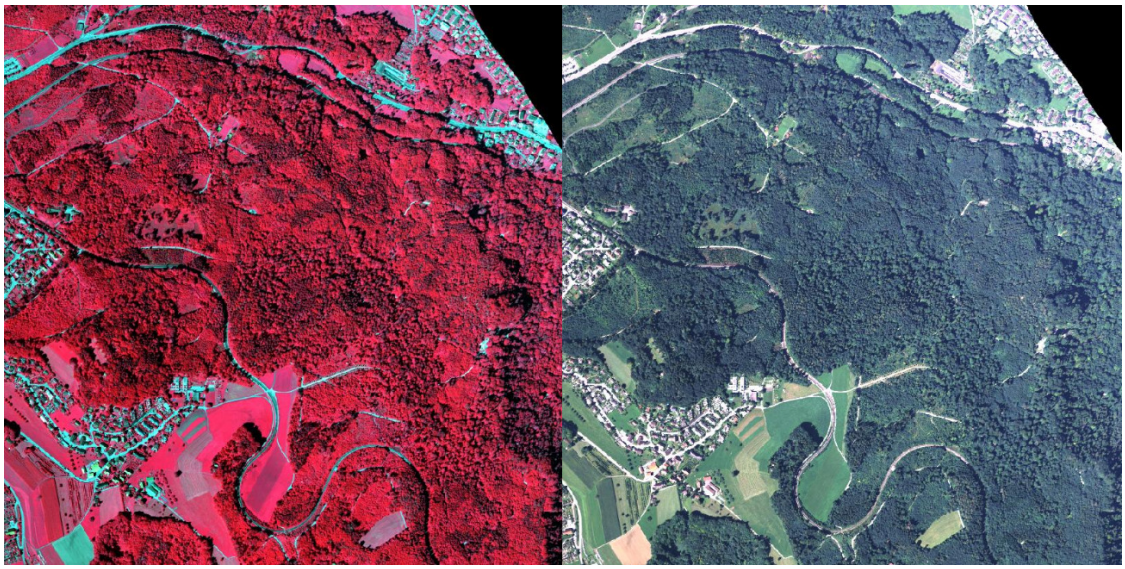

Figure 5.4 – From the left, CIR and RGB orthophotos of the study area Üetliberg

5.1.3 GROUND TRUTH DATA AND TREE SPECIES

In order to validate the classification results, ground truth data was collected in the natural environment so that it was as representative as possible of the study area. This operation is especially important in order to relate image data to real features and materials on the ground. Three ground surveys were carried out during the main vegetation period focusing on tree species that would fulfill, at the same time, two requirements:

a) SPREAD, i.e. at least 5% coverage in Switzerland;
b) VISIBILITY in the aerial images.

Hence, the species crowns were recorded and delineated on the corresponding aerial images, while the trees positions (X, Y) were determined with a sub–decimeter GPS with differential corrections (Leica TPS1200), for a total of 398 samples. Subsequently, they were digitized on the ADS40 RGB images, using as reference both these information. The seven selected tree species are listed in table 5.2 (Waser et al., 2010);

please refer to Appendix B for examples of the species' appearance in ADS40 RGB and CIR imagery.

SCIENTIFIC TREE SPECIES NAME	COMMON TREE SPECIES NAME	SPECIES PROPORTION
Acer sp.	Maple	5 %
Fagus sylvatica	Beech	20 %
Fraxinus excelsior	Ash	15 %
Abies alba	White fir	< 5 %
Larid deciduas	Larch	5 %
Picea abies	Norway spruce	15 %
Pinus sylvestris	Scots pine	< 5 %

Table 5.2 – Sampled tree species: the proportions were estimated by an expert during the field surveys

5.2 DERIVED DATA

For the extraction of the tree area and for the species' classification, new data was got from the original one (presented above): here follows a description of all those supplied by Lars Waser and available for the current master project.

5.2.1 INPUT VARIABLES

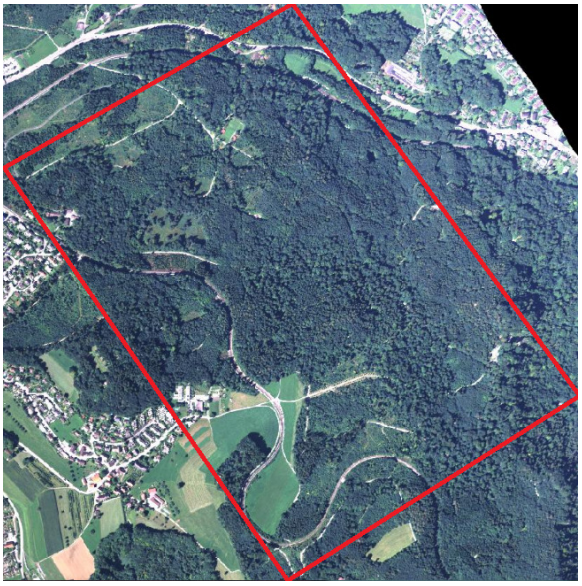

Figure 5.5 – The sub–area, inside the red rectangle

From DTM and image data, some derived quantities ('variables') were computed. Different types of input variables were derived from the ADS40 SH52 images and from LIDAR DTM and DSM , but only concerning a sub-area, mainly wooded, of the one previously shown (7529 x 7529 pixels as dimension).

These variables, which can be grouped into three classes on the base of the geometric, spectral and textural features, were made through the software "Erdas Imagine 9.2" and "ArcGIS 9.3".

GEOMETRIC FEATURES:

- CANOPY HEIGHT MODEL (CHM): it's the description of the trees heights, since it was obtained subtracting the LiDAR DTM from the DSM;
- CURVATURE: it is a measure of the landscape convexity or concavity. The curvature of a surface is calculated on a cell–by–cell basis: namely, for each cell a fourth order polynomial is fit to a surface composed of a 3 x 3 window. A positive value indicates that the surface is upwardly convex at that cell, while a negative one that it's upwardly concave; a value equal to zero corresponds instead to a flat surface;
- SLOPE: it is the rate of maximum change in Z value from each cell;
- ASPECT: it is the direction of the maximum rate of change in Z value from each cell;
- PLANIMETRY: it's the curvature of the surface perpendicular to the slope direction;
- PROFILE: it's the rate of change of slope for each cell; this is the curvature of the surface in the slope direction.

It should be noted that the last 5 variables were all created from the canopy height model and that, in general, the geometrical features have not a crucial role in classifying trees species, unless these latter have a characteristic and well-defined shape (e.g. cypress) or a particular limited height. Unfortunately, this is not completely true for the seven selected species (Waser et al, 2010).

SPECTRAL FEATURES:

- ORIGINAL RED, GREEN, BLUE AND NIR bands;
- RATIOS: these four variables are the result of arithmetic operations between the original channels:

$$\frac{X}{\sum(Red, Green, Blue, NIR)}, X = Red, Green, Blue, NIR$$

- INTENSITY, HUE, SATURATION (IHS): it's possible to define a color space that uses Intensity, Hue and Saturation as the three positional parameters in place of R, G, B; the system has the advantage of presenting colors more nearly as

perceived by the human eye. “Intensity” corresponds to the overall brightness of the scene and varies from 0 (black) to 1 (white); “saturation” is the purity of the color and it also ranges linearly from 0 to 1, whereas “hue” is representative of the color or dominant wavelength of the pixel. Its values interval is conventionally represented by a circle, so that it varies from 0 to 360 by defining the entire colors sphere. Therefore, the combination RGB was transformed into the IHS one and the three parameters (I, H, S) were separated, thereby creating three variables; the same procedure was carried out for the CIR;

- NDVI: the Normalized Difference Vegetation Index is a numerical indicator, typically employed in analyzing remote sensing measurements; it assesses whether the observed target contains live green vegetation or not. The aim is to emphasize the differences between the characteristic components of the vegetation reflectivity: the variation of the green grass’ spectral signature is used to discriminate this class from the dried grass and the bare soil. This variable was computed with the following formula:

$$NDVI = \frac{NIR - RED}{NIR + RED}$$

It can be noted that, beyond the simplicity, this index is quite powerful in performing a qualitative classification thanks to its capacity to broadly distinguish vegetated areas from other surface types (water, soil, etc.); instead, more attention should be paid in quantitative estimations since NDVI value turns out to be sensitive to some perturbing factors (clouds, atmospheric effects, etc.);

- PRINCIPAL COMPONENT ANALYSIS (PCA): PCA involves a mathematical procedure that transforms a number of possible correlated variables into a number of uncorrelated ones, called “principal components” and related to the originals by an orthogonal transformation. It’s defined in such a way that the first principal component has a variance as high as possible (i.e. it accounts for as much of the data’s variability as possible) and each subsequent component, in turn, has the highest variance possible under the constraint to be orthogonal to the previous (see figure 5.6). PCA is often used as a method of compression since it allows redundant data to be compacted into fewer bands; moreover, these are not correlated and often more interpretable than the source data.

A total of six PCA bands were generated, half coming from the RGB combination and half from the CIR one.

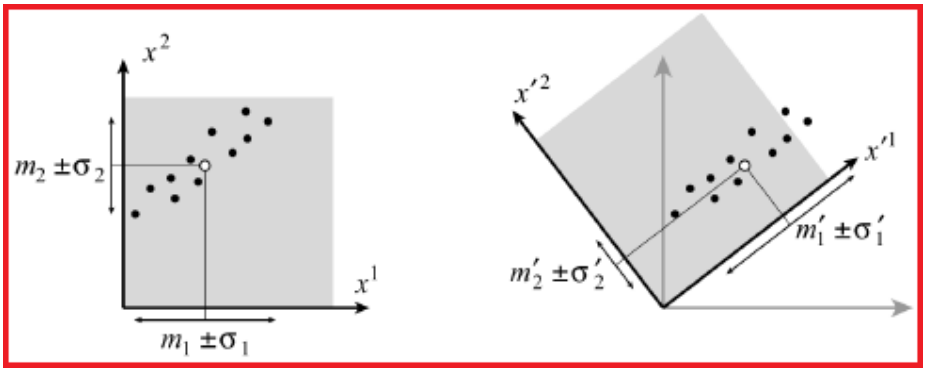

Figure 5.6 – A two-dimensional illustration of the principal component transformation (Dermanis & Biagi, 2002)

TEXTURAL FEATURE:

* SKEWNESS: it measures the asymmetry in an image histogram, by indicating that the "tail" on the left side is longer than the right side (positive value) or vice versa. A moving window of size 5 x 5 was applied independently on the four original channels, getting back four new variables computed using the following formula:

$$Skewness = \frac{\left|\sum(x_{ij} - M)^3\right|}{(n-1)(V)^{3/2}}$$

where:

° x_{ij} = value of pixel (i, j);

° n = number of pixels in the window;

° M = mean of the moving window;

° V = variance.

It should be remarked that the 31 listed variables were generated either in Erdas Imagine 9.2 and then exported as grid stacks in ArcGIS 9.3, or directly in the latter one: however, they were all exported from it in order to be supplied as *.img* (more variables' details are presented in Appendix C).

Finally, a sore point that has to be underlined: unfortunately only few days before the end of this work, it was found out that the original NIR variable had some problems. A bug in the orthophoto generation (only for the CIR images), using SocetSet, created a linear stretching of the values [0; 65000]: nevertheless, some tests done by Lars Waser are giving evidence that the influence on the analysis, on the selection procedure and on the findings is not significant.

5.2.2 TREE MASK

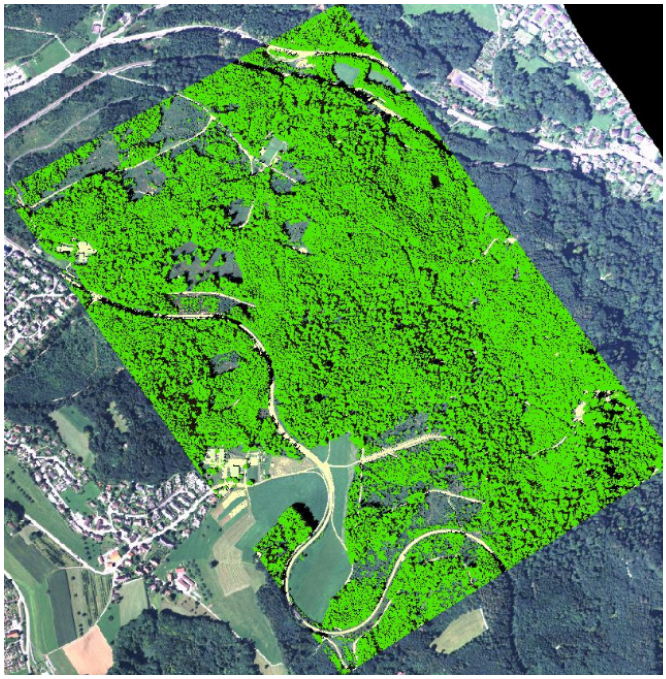

Figure 5.7 – Tree mask overlaid on the RGB orthophoto

The extraction of the area covered by trees is required for the area-wide mapping of the classified species; its production can be summarized in three steps (Waser et al., 2008).

1) the digital canopy model was produced subtracting the LiDAR DTM from the DSM;
2) pixels with values greater than 3 m were used to extract potential tree areas, according to the definition in the Swiss NFI (see section 4.1);
3) non-tree objects (e.g. rocks, buildings, artifacts, etc.) were removed thanks to spectral information from the ADS40 SH52 RGB images (low IHS pixel values) as well as information about the image segments: for instance, segments on buildings have lower curvature values and ranges than trees or large shrubs.

The result was the sunlit tree area of the test field Üetliberg shown in figure 5.7.

5.2.3 TREE SPECIES SAMPLES

The last set of data was constituted by eight shapefiles (*.shp*): seven of them contained groups of polygons, digitalized on ADS40 RGB images and corresponding to trees of the same species (information known by means of the ground truth data collection; see subsection 5.1.3). A similar digitalization, but only on the shadows, occurred to obtain the eighth file. Afterwards, all were employed for the creation of the so called “training” and “validation” samples, useful in the classification procedure.
Attached to them, also 31 excel files (*.xls*): the gray values of the pixels belonging to the previous polygons with their absolute frequencies were listed for statistical inspections.

SHAPEFILES	NUMBER OF SAMPLES
Ash.shp	52
Beech.shp	56
Larch.shp	45
Maple.shp	38
Norway spruce.shp	107
Scots pine.shp	22
White fir.shp	57
Shadows.shp	65

Table 5.3 – The eight shapefiles with their number of samples

VARIABLES SELECTION AND CLASSIFICATION

Following a structure parallel to the previous part ("the DSM generation"), in this chapter the experimental work is presented:

a) TRAINING AND VALIDATION SAMPLES: the shapefiles' polygons were selected for getting two different sets of samples;
b) RESCALING: homogenization of all the variables to ensure they had the same radiometric resolution and gray values range;
c) STATISTICAL ANALYSIS: it allowed a starting variables selection;
d) VARIABLES SELECTION: different operations were done to find out a combination able to lead to a potential improvement of the results of the tree species classification;
e) CLASSIFICATION: Isodata, Maximum Likelihood method and the one based on the Mahalanobis distance were employed;
f) QUANTITATIVE EVALUATION: to assess the results of the classifications.

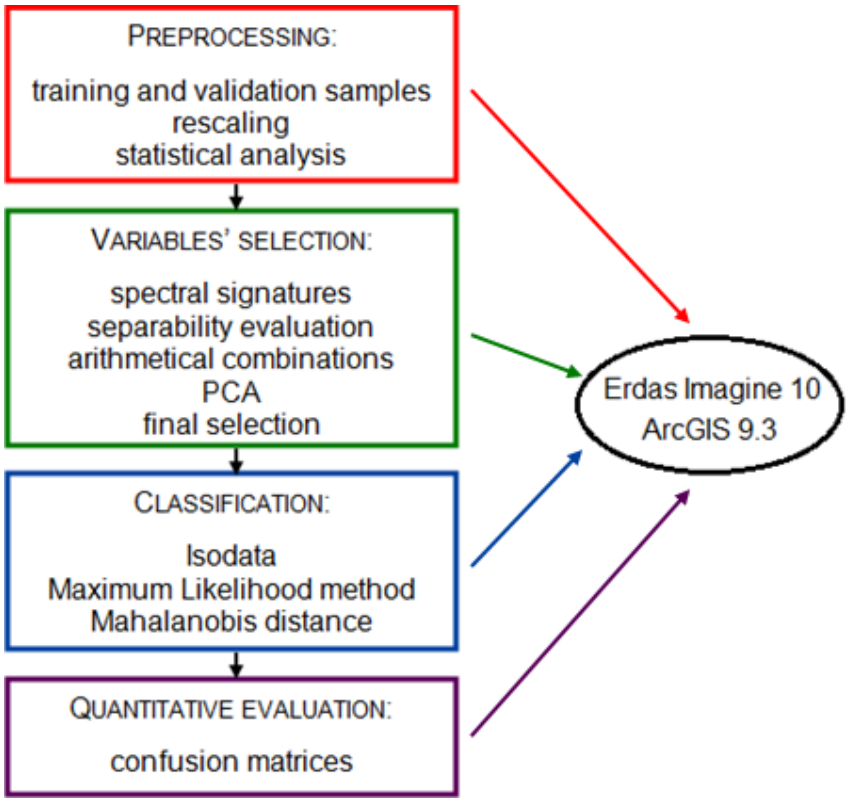

Figure 6.1 – The workflow with the employed software

6.1 PREPROCESSING

A first elaboration of the data provided by Lars Waser was needed to prepare it for the subsequent operations, which constitute the actual experimental part.

6.1.1 TRAINING AND VALIDATION SAMPLES

In summary, 8 shapefiles relating to the seven tree species crowns and to the shadows (see subsection 5.2.3) were processed to obtain:

- TRAINING SAMPLES: in the classification process, the image pixels are assigned to the same class when their values are similar in the different bands/axes of the multispectral space. To establish a correspondence between the identified classes and the ground cover categories is still necessary to have calibration data. Usually called “training samples”, they can be collected through field work and represent the hypothesis on which the unsupervised classification is based: that is, knowing a priori classes of a sufficient number of pixels;
- VALIDATION SAMPLES: they are groups of pixels, different from the prior ones but with classes still a priori known; they’re used after performing the classification, in order to validate and check the correctness of the algorithm’s results.

A rigorous and objective approach should be the groups creation by a clean split-up of the original sample (essentially, cutting it in half): however, this could lead to unbalanced sets, i.e. characterized only by small or large polygons or affected by errors present in a single region, etc. To prevent such drawbacks, it was preferred a manual selection of the polygons, surely more arbitrary but able to ensure a greater representation of the variation of the samples spectral signature values: in fact, they can range, though slightly, from area to area as well as from tree to tree.
The choice was done trying to fulfill some conditions concerning the final sets’ polygons, which should have:

- similar distribution in the area of interest (AOI);
- similar number;
- similar total covered area (see table 6.1).

Hence, the training polygons were selected by hand in ArcGIS and the remaining ones were assigned to the validation set: thus, two new shapefiles were created from each of the original ones (8 training and 8 validation samples).

Finally, all the files were converted into the *.aoi* format since it's the only accepted by the subsequently employed instrument "Signature Editor" of Erdas Imagine.

	TRAINING SAMPLES		VALIDATION SAMPLES	
CLASS	NUMBER OF POLYGONS	TOTAL COVERED AREA [m^2]	NUMBER OF POLYGONS	TOTAL COVERED AREA [m^2]
Ash	28	712	25	702
Beech	28	708	29	635
Larch	23	184	23	181
Maple	18	334	21	332
Norway spruce	54	734	54	747
Scots pine	12	65	11	53
White fir	29	246	29	243
Shadows	33	453	32	458

Table 6.1 – Training and validation samples: the number of polygons and the area covered by them

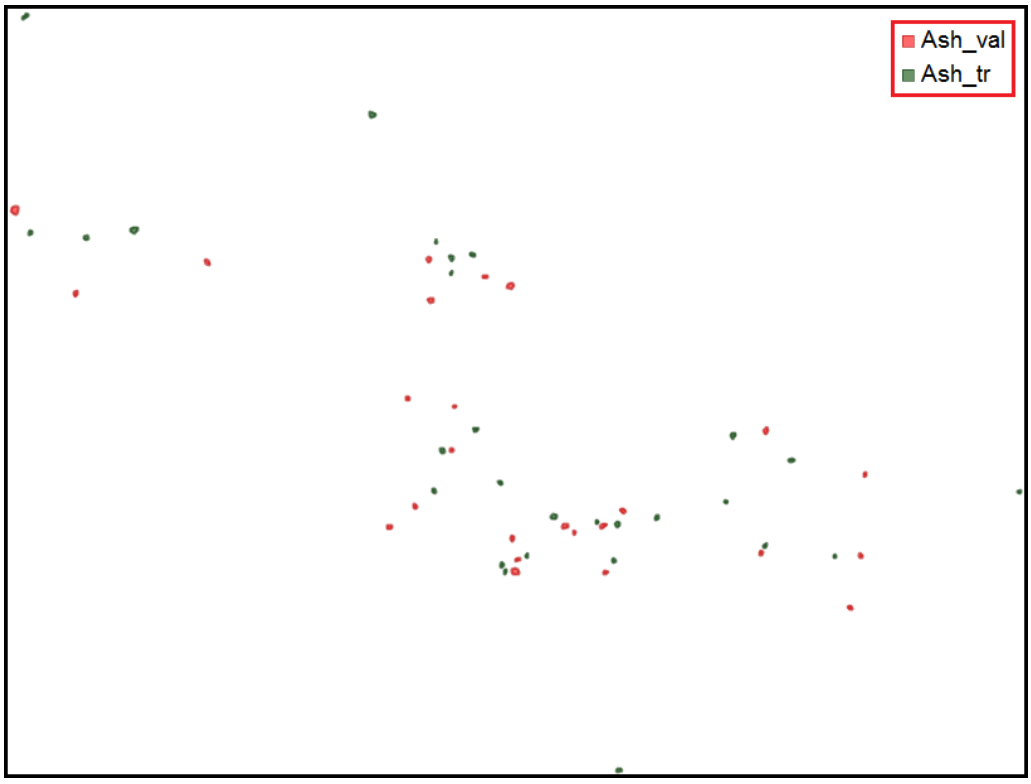

Figure 6.2 – Ash: similar distribution of training (Ash_tr) and validation (Ash_val) samples

6.1.2 RESCALING

The input variables were 31 single *.img* files: even if they represented always the same area with an equal point of view, they were the result of different processes that influenced both the values range and the data type. Moreover, the background of the variables (i.e. that part of the study area outside the sub-region visible in the variables) was constituted by the so-called "No Data" (pixels without an acquired value): during the exporting procedure, the software ArcGIS assigned to them an automatically conventional number, different on the basis of the values range of the specific file.
Thus the situation was a bit bewildering, with variables that had, at the same time, different:

- data type: float, Unsigned 16-bit, Signed 8- bit and so on;
- values range: for instance [0; 89], [-1; 1] or [0.0087; 0.4125];
- No Data value: -3.40E+38, -128, 0 and so on.

A list of these details can be found in Appendix C (for all the variables).

Now it should be said that Erdas doesn't work with a so big number of inputs, which have to be stacked together: in fact, different "images" can be "put together" in any order and saved to a single *.img* file, without occurrence of merging. This layer stack can be easily done with the proper command, but the "*sine qua non*" condition is that all the files should have both equal gray values range and data type.
However, Erdas provides also a "rescale" function with which it's possible to transform the various values ranges to a common one: data can be stretched or compressed to meet the new interval, but original low and high values are respectively rescaled to new low and high values.
In this project, new rescaled variables were computed by choosing

Unsigned 16-bit, integer values [0; 2^{16}-1]

as final data type, for different reasons:

- the interval [0; 65535] is suitable for all the variables: even in the case of decimal digits, only half of them turns out to be significant. Let's consider, for example, the Canopy Height Model whose exact range is [0; 53.46881103]: since the height is usually measured with accuracy of decimeters, it doesn't make sense to conserve all the following digits;

- the transformation to 16-bit is for sure linear, thereby it doesn't substantially modify the gray values: in other words, it doesn't influence the future classification;
- the computational effort is reduced, with better performances.

However, it should be borne in mind that also the No Data pixels values were transformed: in particular, since Erdas gave them by default the minimum value of the new range (in this case, 0), they were mixed with the others, by changing the histograms' statistics.

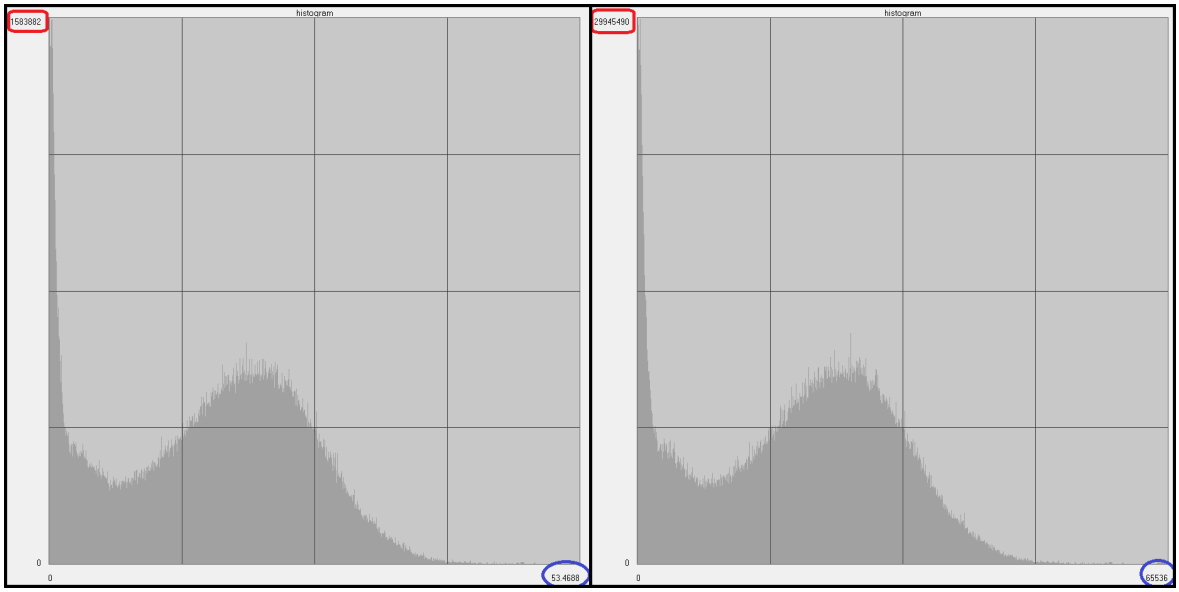

Figure 6.3 – CHM before (on the left) and after the rescaling (on the right): it's possible to see how the values range changes without an appreciable variation of the histogram shape; the number of pixels equal to zero increases due to the No Data presence

VARIABLES	MEAN	MEDIAN
Original CHM	14.973	16.528
Rescaled CHM	9169.466	0

Table 6.2 – After the rescaling, the increase of the pixels equal to zero determines a reduction of the mean and the median values

Despite this unpleasant effect, it must be said that there wasn't the risk of misclassified pixels due to the mixture: in fact, only a pixel equal to 0 in all the variables can be classified as "No Data".

6.1.3 STATISTICAL ANALYSIS

As already said in subsection 5.2.3, Lars Waser supplied also 31 excel files: each of them was related to a single original variable and contained the values of the pixels belonging to both that variable and the digitized polygons of the specific class (7 tree species and shadows). Thereby, eight lists of this type were present in every file, together with the corresponding absolute frequencies.

A satisfactory classification generally corresponds to an equally good separability of the classes' spectral signatures, in the multispectral space: this feature can be analyzed synthetically through two main statistics, i.e. mean and standard deviation. The first is commonly considered the "center" of the classes, while the second is their dispersion: therefore, the optimal situation is characterized by mean values as far as possible and, at the same time, by standard deviations as low as possible. In such a case, it is said that the classes have a high separability, that is, the algorithm will be able to distinguish them with a very low final number of misclassified pixels.
Considering all the variables, the multispectral space would be 31-dimensional and a data analysis would be "impossible": it is instead more feasible to calculate the statistics (of all classes for each variable) and to plot them. Each resulting graph makes it possible to view a single-axis of the multispectral space, by allowing the selection of the variables that lead to a better classes separability.

Thus, the statistics were computed:

$$\mu = \frac{1}{N}\sum_i x_i f_i \qquad \sigma = \sqrt{\frac{1}{N-1}\left[\sum_i (x_i - \mu)^2 f_i\right]}$$

where:

- μ is the mean value and σ is the standard deviation one;
- N = number of values;
- x_i = i-th value;
- f_i = absolute frequency of the i-th value.

Hence, the separability was observed plotting the mean values and the (μ ± σ) ones of only the seven tree species, since their spectral signatures were similar to each other but definitely different from the "shadows" one.

Furthermore, a special care was addressed to maximize the separability between some particular classes: in fact Waser et al. (2010) pointed out that the non-dominant tree species maple (*Acer sp.*) was often misclassified as the two dominant deciduous species ash (*Fraxinus ex.*) and beech (*Fagus syl.*); misclassification happened also between Scots pine (*Pinus sy.*) and larch (*Larix dec.*).

Starting from these 31 plots, ten variables were selected since they seemed to be the most promising ones:

VARIABLES	
CIR_IHS_Hue	Ratio_Green
CIR_IHS_Satuation	Ratio_NIR
RGB_IHS_Hue	Original Red band
RGB_IHS_Saturation	Original Green band
NDVI	Original NIR band

Table 6.3 – The 10 variables which maximizes the tree species separability

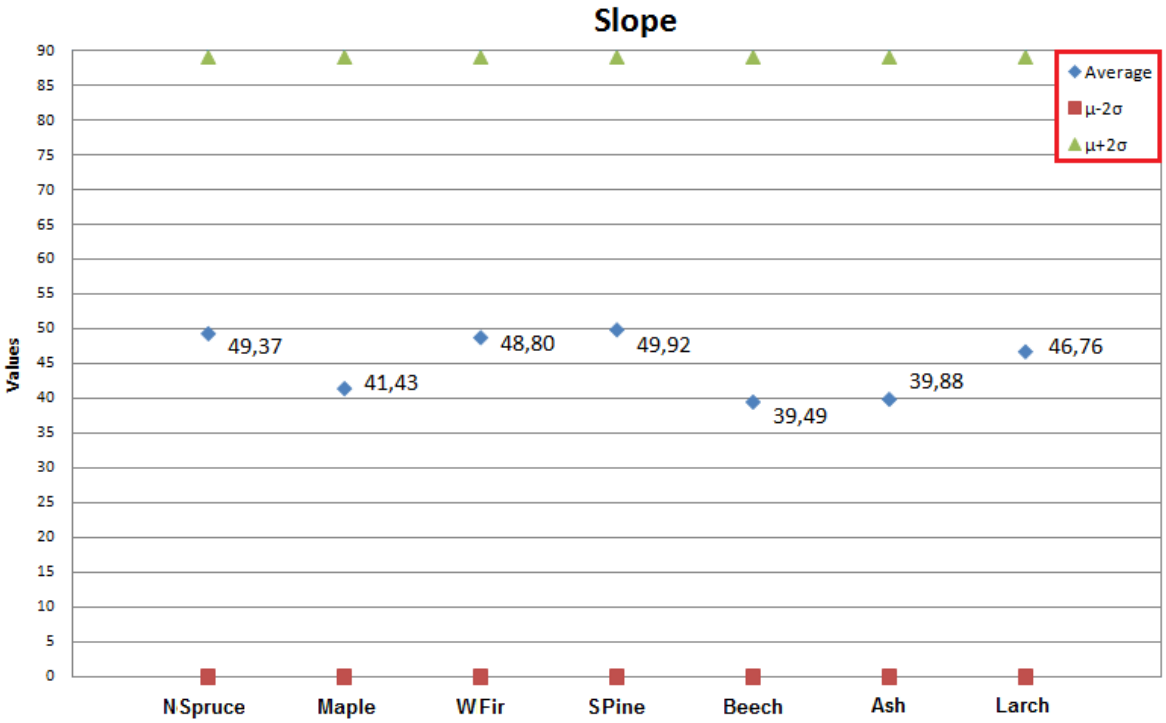

Graph 6.1 – Rejected variable (Slope): it's easy to note how the classes have the same variability and how they totally overlap

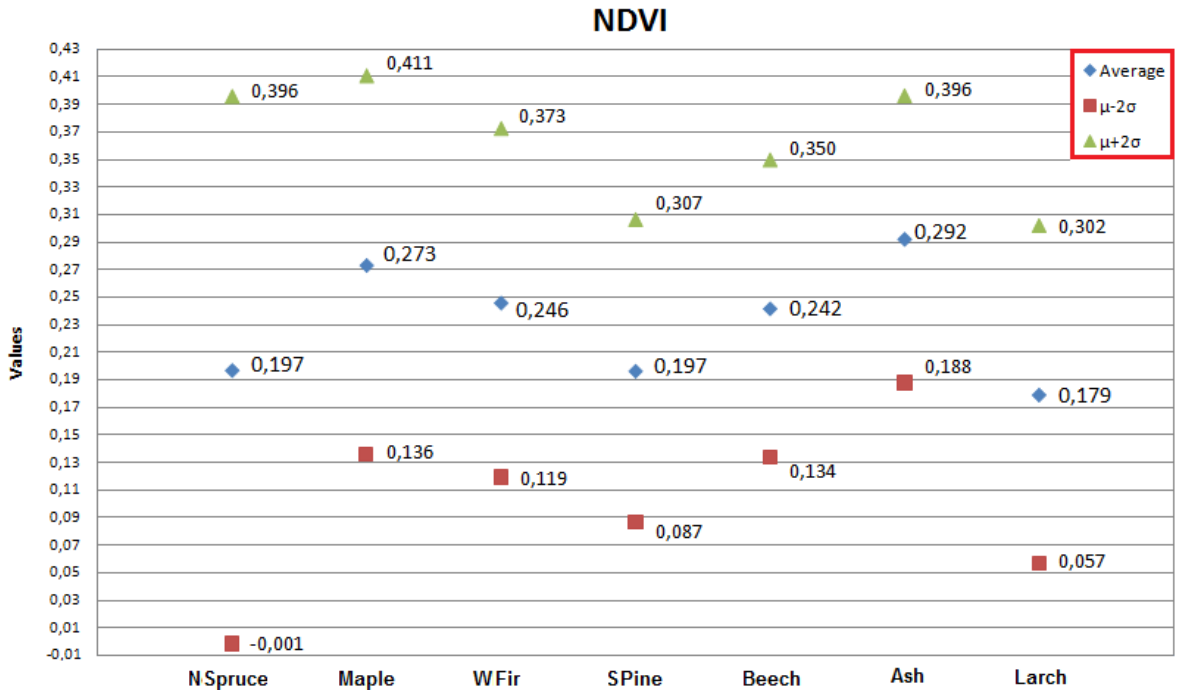

Graph 6.2 – Selected variable (NDVI): the separability is here more promising; however, it can be noted how deciduous species have similar spectral signatures (of course, the same for the coniferous ones)

6.2 VARIABLES' SELECTION

As already stated, the experimental work tried to find out that combination able to lead to a potential improvement of the results of the tree species classification: unfortunately, because of the time, it had to decide to stop the procedure after the principal component analysis (PCA), when a sufficient result was achieved. However, the various steps could be iterated different times to refine the final selection even more.

Furthermore, it should be underlined that Erdas Imagine proved to be a bit "limited" when employed in research work: indeed, it acted as a black-box in many cases, without giving the possibility to deeply know functions details or implemented formulas. One can't do anything but putting trust in it.

6.2.1 LAYER STACK: 10 VARIABLES

After choosing the ten variables, it was necessary to use the proper command to unify them in a "layer stack" (*.vsk*, with "Unsigned 16-bit" as data type). Afterwards, a signature file (*.sig*) should be associated to each generated layer stack, by opening on it the training samples (one at a time) and creating the corresponding spectral signatures through the "Signature Editor" tool.

Next step was the evaluation of the separability: the implemented function computes this statistical measure of the distance between signatures for any combination of bands. Thereby, it enables to determine the best subset of layers, to use in the classification, through formulas related to the Maximum Likelihood decision rule. Since there was more interest for this classification method, it was decided to exploit this command; the distance measure can be calculated on the base of different formulas:

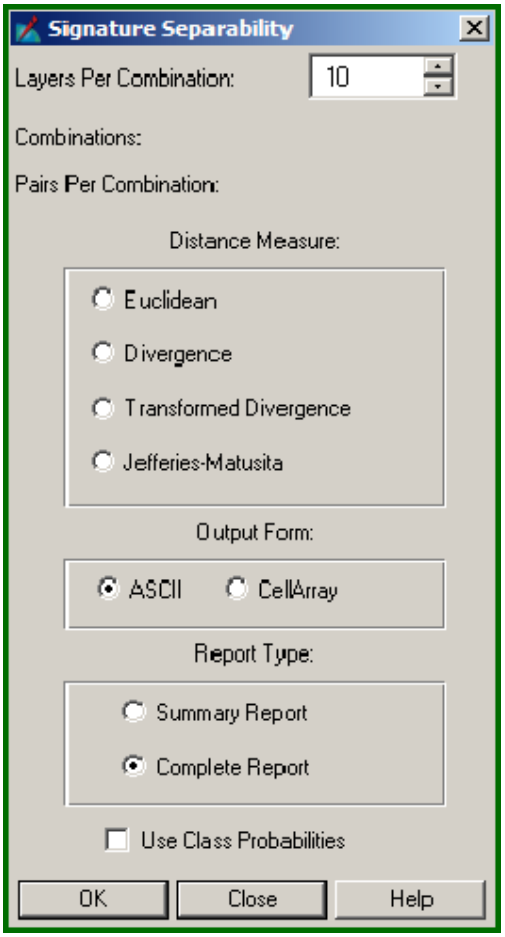

Figure 6.4 – The signature separability window

- EUCLIDEAN DISTANCE: the spectral distance between the mean vectors is computed;
- DIVERGENCE;
- TRANSFORMED DIVERGENCE (TD): it gives an exponentially decreasing weight to increasing distances between the classes;
- JEFFRIES – MATUSITA (JM) DISTANCE: it has a saturating behavior with increasing class separation like transformed divergence.

Hence, a part from the Euclidean one, the other three options use the covariance matrix of the signatures as well as their mean vector: in particular, the covariances should be invertible to allow the procedure.

Let's consider some aspects, relevant for discarding options:

a) the *Euclidean distance* does not take into account the dispersion of the data;

b) the *Divergence* values are not bounded in a precise interval: hence, without an indicator, it's difficult to understand how much signatures are far from each others;
c) the *Transformed Divergence* method is bounded between 0 and 2000 (poor and high separability, respectively) and seems the more suitable: unfortunately, it proved to be too optimistic in its predictions, with values often equal to the maximum one.

These considerations leaded to the employment of the JM distance that, though not as computationally efficient as the TD, is bounded between the values 0 and 1414, namely, bad and good separability.
The formula for computing the JM distance is the following:

$$\alpha = \frac{1}{8}(\mu_i - \mu_j)^T \left(\frac{C_i + C_j}{2}\right)^{-1} (\mu_i - \mu_j) + \frac{1}{2}\ln\left(\frac{\left|(C_i + C_j)/2\right|}{\sqrt{|C_i| \times |C_j|}}\right)$$

$$JM_{ij} = \sqrt{2(1 - e^{-\alpha})}$$

where:

° (i, j) are the two signatures (classes) being compared;
° C_i = the covariance matrix of signature i, with determinant equal to $|C_i|$;
° μ_i = the mean vector of signature i;
° ln = the natural logarithm function.

The JM values are obtained by multiplying by 1000 the result of the above formula.

The proper Erdas command gives as output a report with the distances (calculated through the chosen method) for every possible pair of signatures, considering all the bands and their requested combinations. It contains also the average and the minimum distance for the band set, useful to compare to other separability listings (for other bands combinations) and determine which best group of layers allows an improved classification.
In figure 6.5 a comparison between the results provided by Transformed Divergence and JM distance is shown, considering all the 10 variables together: it can be seen as

the critical classes in the green boxes (maple/beech, maple/ash, beech/ash and Scots pine/larch) present the worse values.

Bands	AVE	MIN	Class Pairs:							Class
			1: 2	1: 3	1: 4	1: 5	1: 6	1: 7	1: 8	1 Maple
			2: 3	2: 4	2: 5	2: 6	2: 7	2: 8	3: 4	2 Beech
			3: 5	3: 6	3: 7	3: 8	4: 5	4: 6	4: 7	3 Ash
			4: 8	5: 6	5: 7	5: 8	6: 7	6: 8	7: 8	4 Norway spruce
1 2 3 4	1873	754	754	865	2000	1995	1999	2000	2000	5 Scots pine
5 6 7			1186	2000	2000	2000	2000	2000	2000	6 Larch
8 9 10			1989	1988	2000	1995	1986	2000	2000	7 Shadows
			1954	1758	2000	1994	2000	1977	2000	8 White fir

Bands	AVE	MIN	Class Pairs:							Class
			1: 2	1: 3	1: 4	1: 5	1: 6	1: 7	1: 8	1 Maple
			2: 3	2: 4	2: 5	2: 6	2: 7	2: 8	3: 4	2 Beech
			3: 5	3: 6	3: 7	3: 8	4: 5	4: 6	4: 7	3 Ash
			4: 8	5: 6	5: 7	5: 8	6: 7	6: 8	7: 8	4 Norway spruce
1 2 3 4	1323	827	827	839	1404	1388	1391	1414	1376	5 Scots pine
5 6 7			1007	1407	1397	1394	1414	1389	1391	6 Larch
8 9 10			1387	1366	1414	1344	1321	1349	1414	7 Shadows
			1284	1195	1414	1356	1414	1340	1414	8 White fir

Figure 6.5 – Extract of two separability reports: Transformed Divergence at the top and JM distance at the bottom, with critical classes in the green boxes. The average value of the first is higher than the second one: in fact TD proved to be generally a bit too optimistic in its evaluation

In this phase, several tests were performed to identify the more suitable method, i.e. the JM distance (because the TD proved to be generally too optimistic, as already mentioned).

Since an estimate with all the bands together is not much coherent with the goal of finding out their best combination, the results in the figure above were considered only as starting reference values for the critical classes. In fact, all the subsequent operations were performed with a special attention to their variations, trying to tune the variables combination able to improve the classification in general and their separation in particular.

6.2.2 ARITHMETICAL COMBINATIONS

A typical remote sensing procedure is the construction of new “pseudo-bands” able to provide specific advantages in the images understanding and classification. The set of transformations that combine original bands to create new ones are generally called “matrix algebra” or “bands algebra”.

Hence, to enhance the separability, some arithmetical combinations of the ten selected variables (in the not rescaled version) were done thanks to the "Model Maker" tool of Erdas Imagine: these operations are listed in table 6.4.

ARITHMETICAL COMBINATIONS	
$(Ratio\_NIR)^2$	$\sqrt[2]{CIR\_IHS\_Hue}$
$(Ratio\_NIR)^3$	$\sqrt[3]{CIR\_IHS\_Hue}$
$\sqrt[2]{Ratio\_Green}$	$\frac{RGB\_IHS\_Saturation - Original\_Red}{Original\_Red + 1}$
$\sqrt[3]{Ratio\_Green}$	$\frac{CIR\_IHS\_Hue - Ratio\_Green}{Ratio\_Green + 1}$

Table 6.4 – The eight arithmetical operations

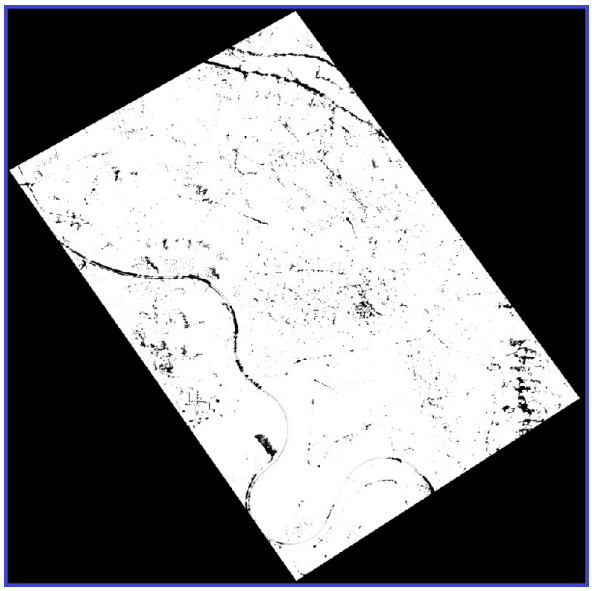

Figure 6.6 – Appearance of $(Ratio\_NIR)^2$

These new variables were produced with "Signed 32-bit" as data type: it has to be said that a normalization procedure is always performed after the bands algebra, due to the fact that the resulting images could have values outside the admitted interval.

In this project, the rescaling to "Unsigned 16-bit" was also necessary for the subsequent generation of a layer stack containing all the new bands. Moreover, a signature file was created and employed to get the classes' statistics, namely, mean and standard deviations values: the former and the (μ ± σ) ones were then plotted, as already described in subsection 6.1.3. The graphs confirmed what had been already suspected through a visual inspection (see figure 6.6): the images coming from the powers were oversaturated and therefore useless in the following processes.

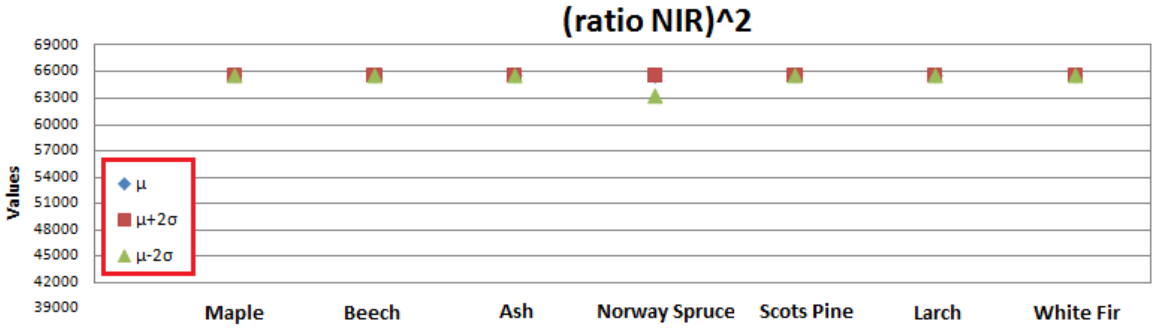

Graph 6.3 – Plot of $(Ratio\_NIR)^2$: the values well show that this image is completely useless

6.2.3 LAYER STACK: 16 VARIABLES

Summarizing the situation, only two rescaled variables of the arithmetical combinations were rejected, whereas the other six were accepted and stacked together with the group of the statistical analysis. This operation is schematized below:

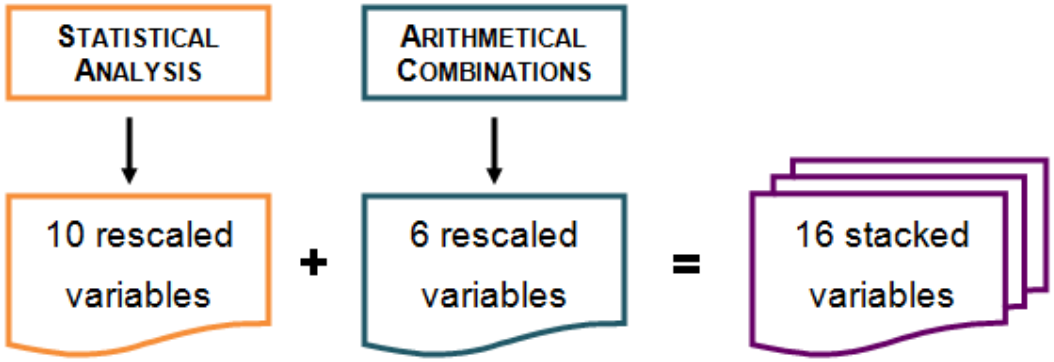

Figure 6.7 – Creation of the new layer stack with 16 variables

Thus, employing the JM distance, the "signature separability" function was run 16 times, increasing by one the number of "layers per combination" at each iteration. To reduce the amount of information in the output reports, only the results below the headings "best minimum" and "best average" separability were compared: the aim was the identification of the combination which would maximize the separability and, at the same time, minimize the number of variables. Of course, greater attention was addressed to the usual critical classes, but without neglecting all the others. A combination of 11 bands (listed in table 6.5) proved to be the best one in fulfilling the two requirements.

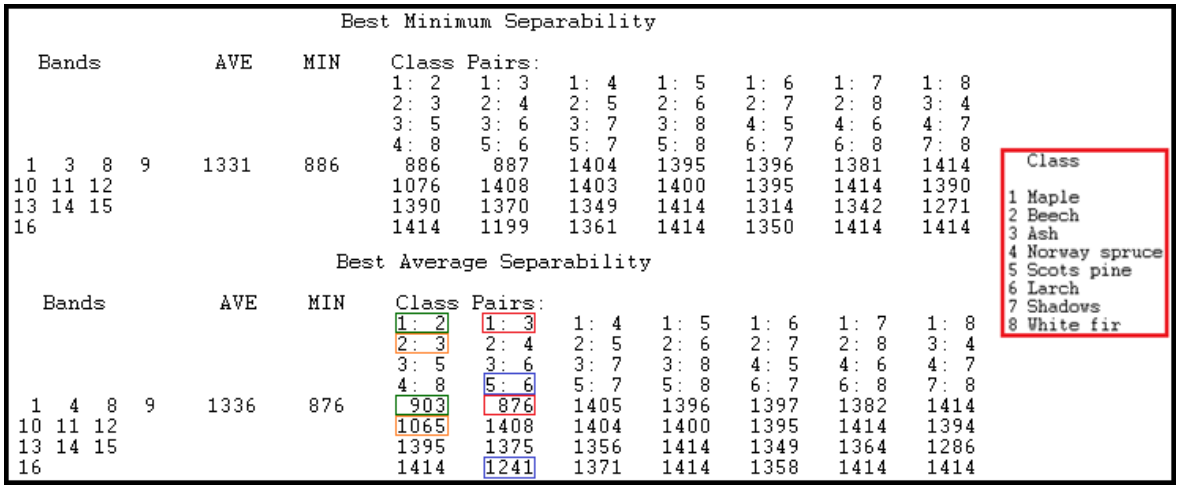

Best Minimum Separability

Bands	AVE	MIN	Class Pairs: 1: 2	1: 3	1: 4	1: 5	1: 6	1: 7	1: 8
			2: 3	2: 4	2: 5	2: 6	2: 7	2: 8	3: 4
			3: 5	3: 6	3: 7	3: 8	4: 5	4: 6	4: 7
			4: 8	5: 6	5: 7	5: 8	6: 7	6: 8	7: 8
1 3 8 9	1331	886	886	887	1404	1395	1396	1381	1414
10 11 12			1076	1408	1403	1400	1395	1414	1390
13 14 15			1390	1370	1349	1414	1314	1342	1271
16			1414	1199	1361	1414	1350	1414	1414

Class

1 Maple
2 Beech
3 Ash
4 Norway spruce
5 Scots pine
6 Larch
7 Shadovs
8 White fir

Best Average Separability

Bands	AVE	MIN	Class Pairs: 1: 2	1: 3	1: 4	1: 5	1: 6	1: 7	1: 8
			2: 3	2: 4	2: 5	2: 6	2: 7	2: 8	3: 4
			3: 5	3: 6	3: 7	3: 8	4: 5	4: 6	4: 7
			4: 8	5: 6	5: 7	5: 8	6: 7	6: 8	7: 8
1 4 8 9	1336	876	903	876	1405	1396	1397	1382	1414
10 11 12			1065	1408	1404	1400	1395	1414	1394
13 14 15			1395	1375	1356	1414	1349	1364	1286
16			1414	1241	1371	1414	1358	1414	1414

Figure 6.8 – Separability for 11 layers per combination: even if slightly, the values of the critical classes are increased (with respect to those in figure 6.5)

SELECTED RESCALED VARIABLES	
NDVI	Original Red band
CIR_IHS_Satuation	Original Green band
RGB_IHS_Hue	Original NIR band
RGB_IHS_Saturation	Ratio_Green
$\frac{CIR\_IHS\_Hue - Ratio\_Green}{Ratio\_Green + 1}$	Ratio_NIR
$\frac{RGB\_IHS\_Saturation - Original\_Red}{Original\_Red + 1}$	

Table 6.5 – The 11 variables which constitute the best combination 'till now

6.2.4 PRINCIPAL COMPONENT ANALYSIS (PCA)

It can be said that, at the moment, the best combination is composed by:

- 9 variables of the statistical analysis;
- 2 variables of the arithmetical operations (i.e. the two ratios).

Thus, they were stacked together in a file to be given in input to the "Principal Components" tool of Erdas Imagine: in fact, the PCA allows to compress the data and to have independent and more interpretable bands (for more information, please refer to subsection 5.2.1). Hence, eleven desired components were supplied as output, again with "Unsigned 16-bit" as data type: after the generation of the corresponding signatures file, the classes' statistics were collected and plotted as usual.

It can be recorded that some bands showed a really better separability, especially for the crucial classes: in graph 6.4, for instance, it's evident the improvement happened between larch and Scots pine (*Larix dec.* and *Pinus sy.*), whereas a similar effect didn't take place for the deciduous trees: therefore, it was tried to ensure an equal enhancement to all the classes, by choosing the components 3, 5, 8 and 9.
It must be said that the plotted values were bounded between 0 and 65535, namely, the minimum and the maximum value of the real data interval.

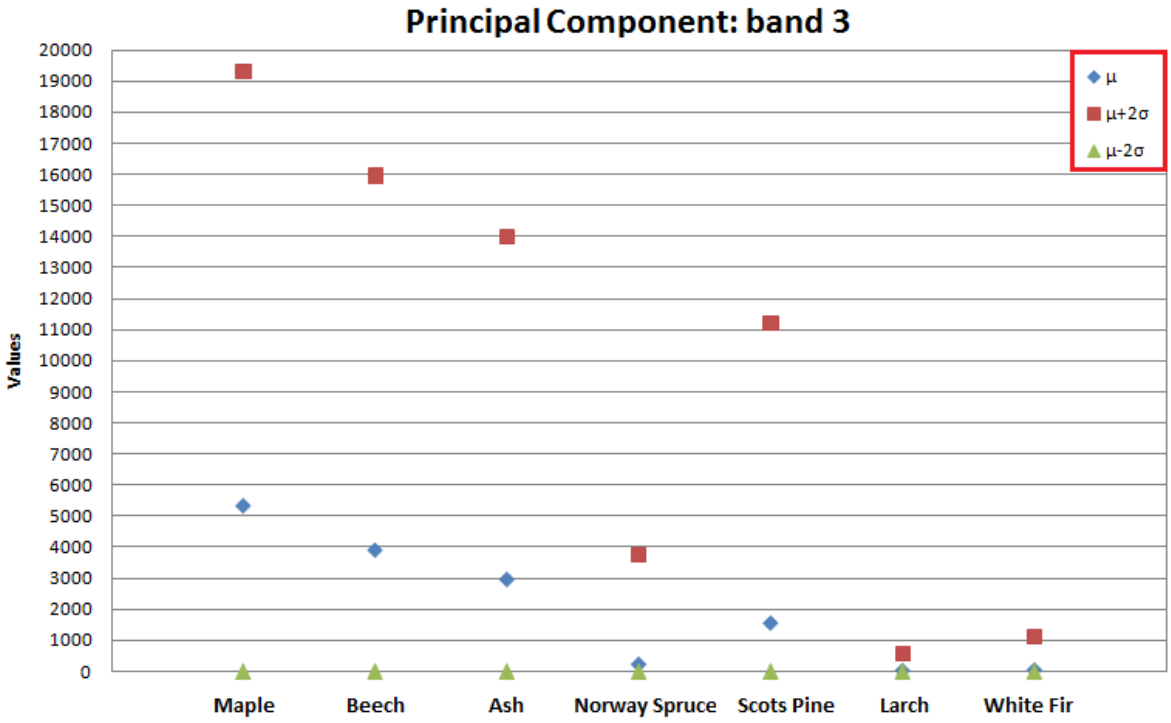

Graph 6.4 – PCA band 3: the achieved improvement can be easily found by looking at the big difference between the larch dispersion and the Scots pine one

On the contrary, graph 6.5 shows an example of rejected component that didn't bring any significant changes in the classes' separability.

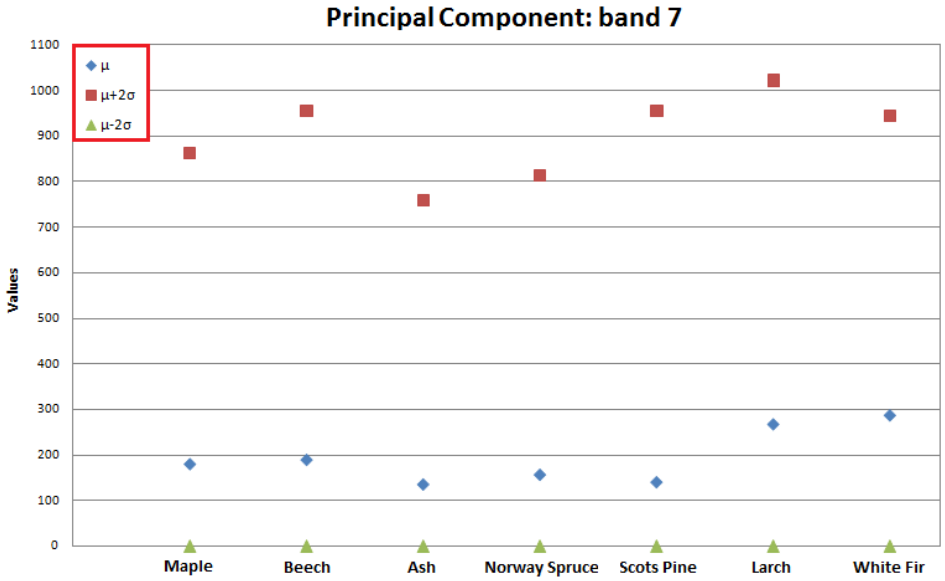

Graph 6.5 – PCA band 7: it can be rejected since the classes overlap almost entirely

6.2.5 LAYER STACK: 15 VARIABLES

Thus, the last layer stack was constituted by 15 variables, of which:

- 9 from the statistical analysis;
- 2 from the arithmetical operations (i.e. the two ratios);
- 4 from the PCA, done on the previous ones.

Again the separability was evaluated by means of the Jeffries-Matusita distance and the reached results were enough satisfactory (especially if compared with the starting ones) to determine the end of the variables selection procedure. The following table summarizes the separability values got at the different steps:

	10 VARIABLES	**16 VARIABLES**	**15 VARIABLES**
Minimum value	827	925	1000
Average value	1323	1355	1370
Maple – beech	827	963	1053
Maple – ash	839	925	1000
Beech – ash	1007	1146	1217
Scots pine - larch	1195	1272	1372

Table 6.6 – The JM distance values for the critical classes: the results improved during the procedure, starting from 10 original variables and ending with 15 (sum of originals, arithmetical combinations and PCA bands). It should be remembered that the JM distance varies from 0 to 1414 (best separability)

6.3 CLASSIFICATION

The classification procedure was carried out on the previous chosen variables' combination, by employing three different algorithms both supervised and unsupervised Afterwards, a qualitative and quantitative evaluation concluded the project.

Even if Erdas Imagine provides many tools that permit to refine the classification results, it was decided to use common algorithms since the main aim of this part was the exploration of the variables' selection:

a) SUPERVISED CLASSIFICATION: starting from the last layer stack (15 variables) and the corresponding signature files, the Maximum Likelihood method and the one based on the Mahalanobis distance were easily run with the proper software commands;

b) UNSUPERVISED CLASSIFICATION: for a brief comparison with the supervised algorithms, it was selected the ISODATA one (Iterative Self-Organizing Data Analysis Technique). As the name suggests, it's an iterative method that uses the minimum spectral distance formula to generate clusters: the function implemented in Erdas needs either arbitrary cluster means or means of an existing signature set to begin. At each iteration, new cluster means are computed, shifted and then exploited for the next steps. The options set in the project are shown in figure 6.9.

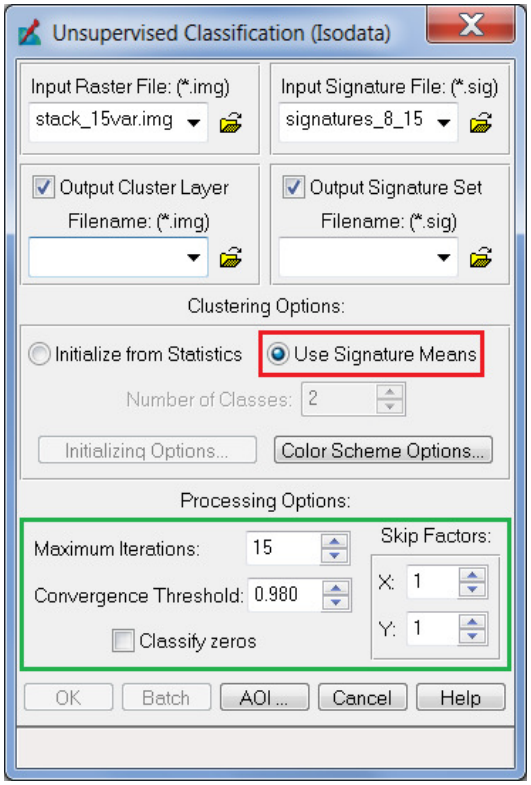

Figure 6.9 – Set options in the ISODATA window

6.3.1 QUALITATIVE EVALUATION

The three thematic output files were visualized through ArcGIS 9.3 and then intersected with the tree mask (described in subsection 5.2.2): in this way, only the vegetated area is visible and all the remaining parts are neglected.
On the basis of a priori information on the algorithm, it can be expected to achieve the best classification from the Maximum Likelihood method, whereas the worse should come from the ISODATA one.
The visual analysis was divided into two separate parts, taking into account areas with different dominance of vegetation type, that is, coniferous and deciduous species.

DOMINANCE OF CONIFEROUS TREES:

The less abundant coniferous species are Scots pine (*Pinus sy.*) and white fir (*Abies al.*), whereas Norway Spruce (*Picea a.*) is the most widespread; as already mentioned, Waser et al. (2010) encountered some misclassification problems concerning the larch (*Larix dec.*) and Scots pine species (for this reason the variables selection was addressed also to improve their separability as much as possible).

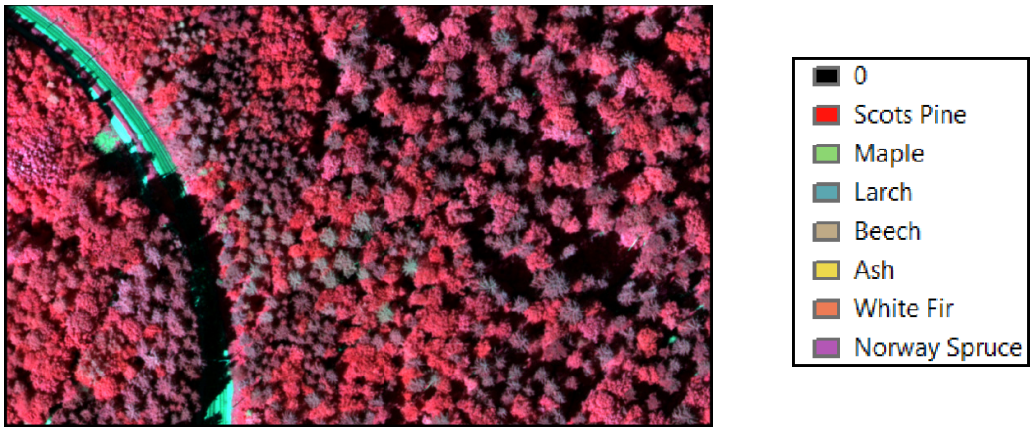

Figure 6.10 – Close and dense forest with dominance of coniferous trees (CIR ADS40 SH52 image) and classification legend (on the right)

Looking at figure 6.11, it can be observed that, since larches were usually classified as Scots pines by the ISODATA method, there's a clearly over-estimation of this latter: it means that, in this case, the trials to improve their separability failed. Furthermore, over-estimation of beeches happened too, while ash and Norway spruce species were almost totally under-estimated.

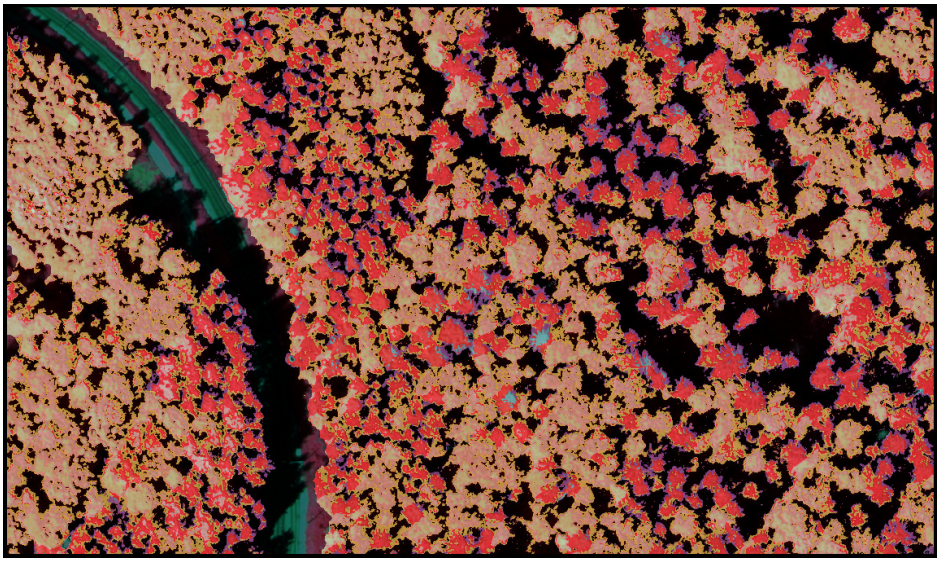

Figure 6.11 – ISODATA classification: dominance of coniferous trees

For what concerns the Maximum Likelihood method, it acted contrary to the ISODATA one since the Scots pine were underestimated whereas the larch was, obviously, overestimated as happened for maple and beech species (see figure below).

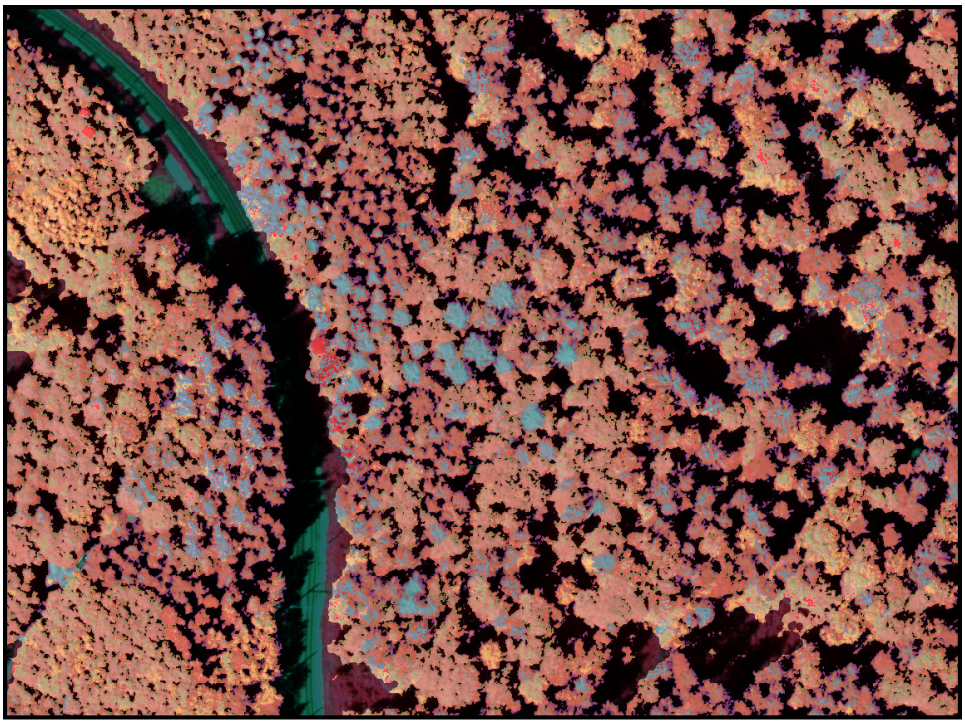

Figure 6.12 – Maximum Likelihood classification: dominance of coniferous trees

Lastly, the Mahalanobis based classification overestimated larch and beech species as well as maple and white fir; on the contrary, ash, Norway spruce and Scots pine were underestimated (see figure 6.13).

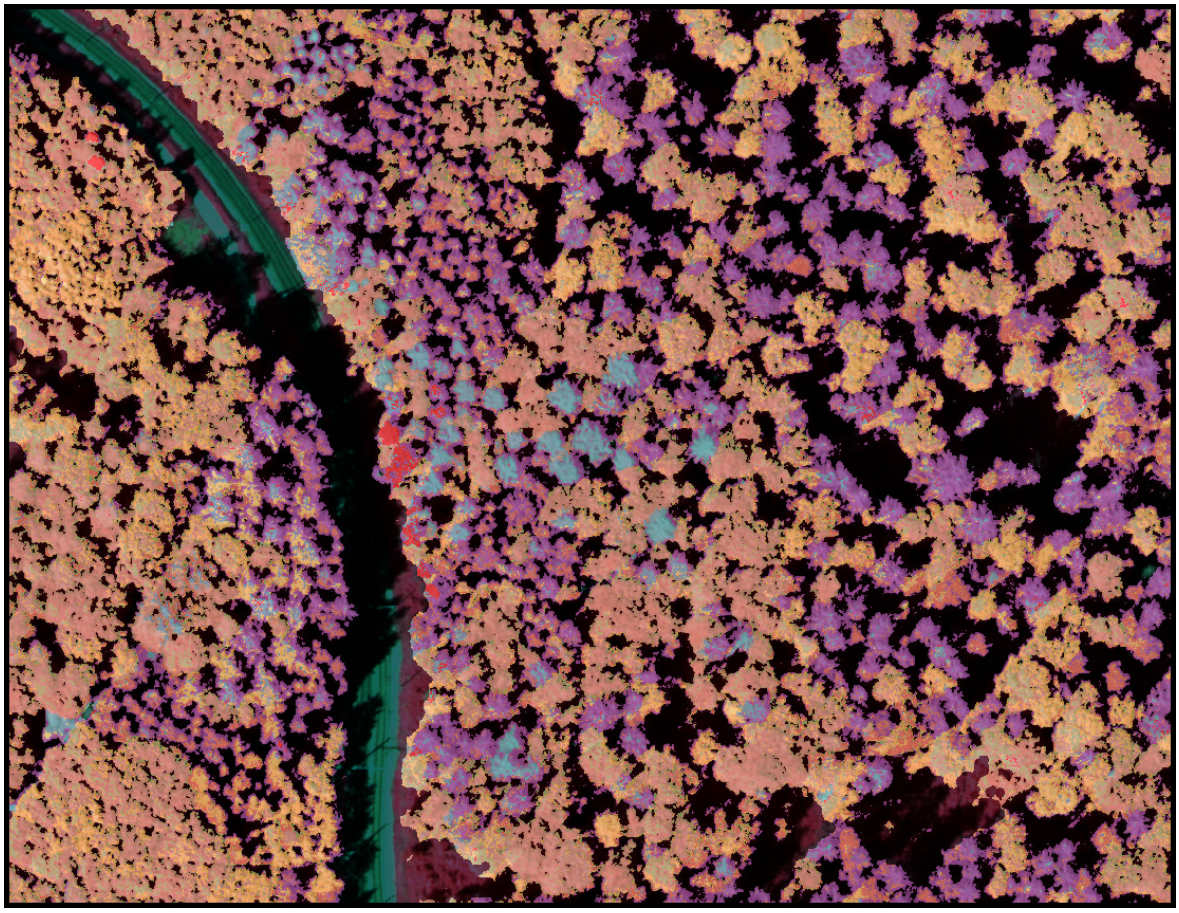

Figure 6.13 – Mahalanobis distance based method: dominance of coniferous trees

Hence, it should be underlined that, in general, the variables selection procedure didn't lead to a really improvement in the coniferous species: in fact, some problems of misclassification still remain, especially between the two "crucial" species (larch and Scots pine).

DOMINANCE OF DECIDUOUS TREES:

The most widespread deciduous species are beech (*Fagus syl.*) and ash (*Fraxinus ex.*), whereas maple (*Acer sp.*) is the less abundant and, hence, often misclassified as the two dominant ones (Waser et al., 2010). Also in this case, it was tried to improve their separability through a suitable variables selection.

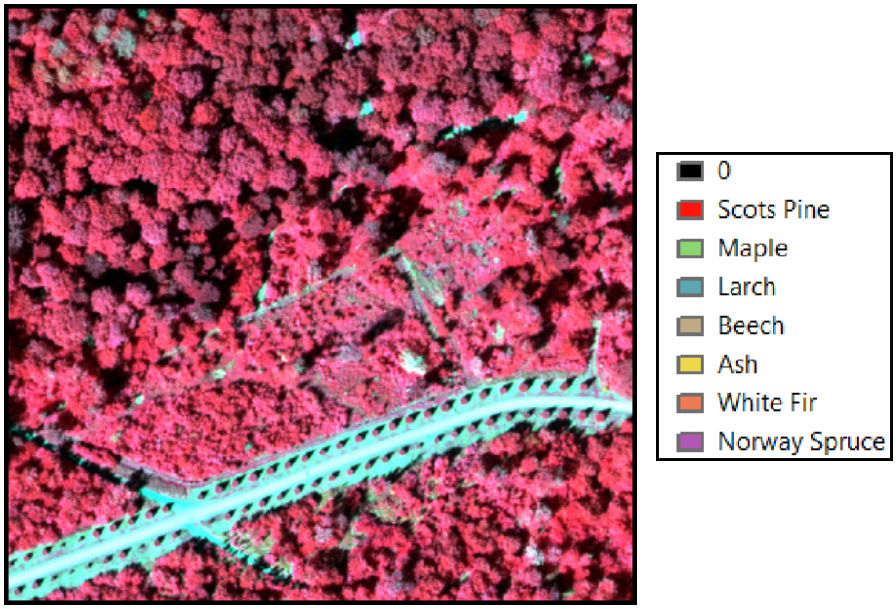

Figure 6.14 – Forest borders with dominance of deciduous trees (CIR ADS40 SH52 image) and classification legend (on the right)

The two dominant deciduous species, that is, beech and ash were clearly overestimated by the ISODATA algorithm, while the maple almost totally disappeared. There were overestimation of Scots pine and white fir as well.

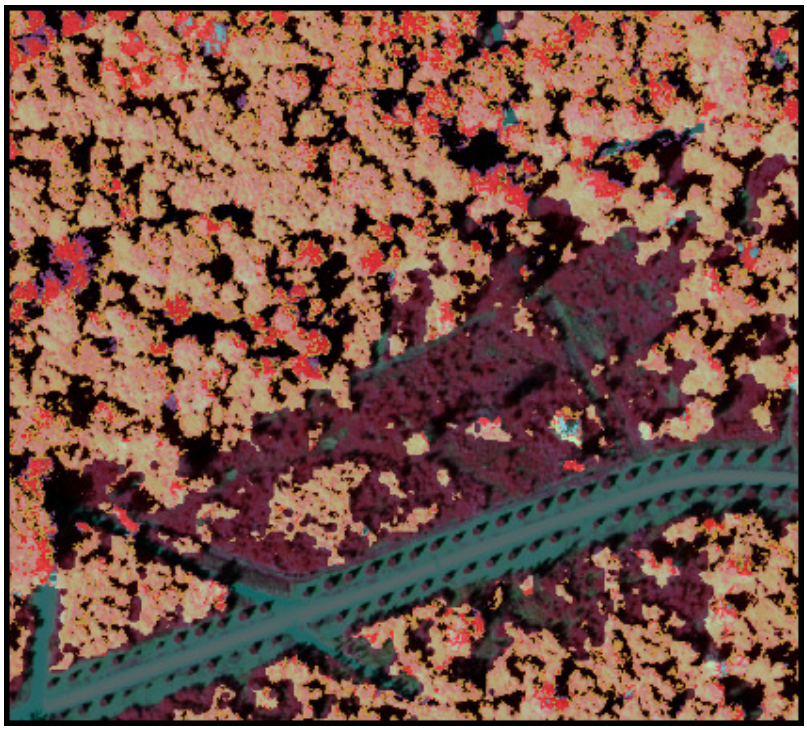

Figure 6.15 – ISODATA classification: dominance of deciduous trees

The Maximum Likelihood algorithm overestimated white fir as well as the dominant deciduous specied (beech and ash) while maple was only partly recognized.

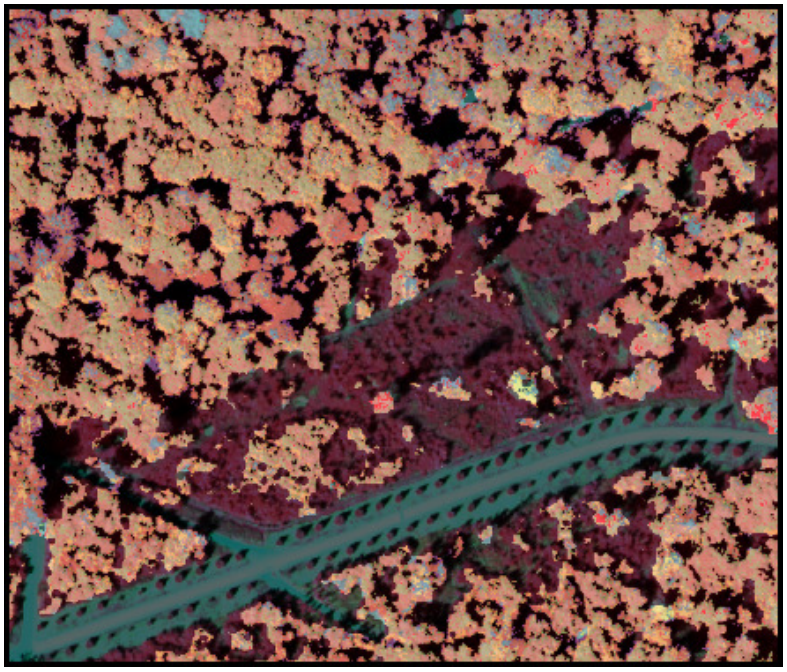

Figure 6.16 – Maximum Likelihood classification: dominance of deciduous trees

In the Mahalanobis classification, it can be observed an overestimation of beech and an underestimation of spruce, while the dominance of ash is only partly visible.

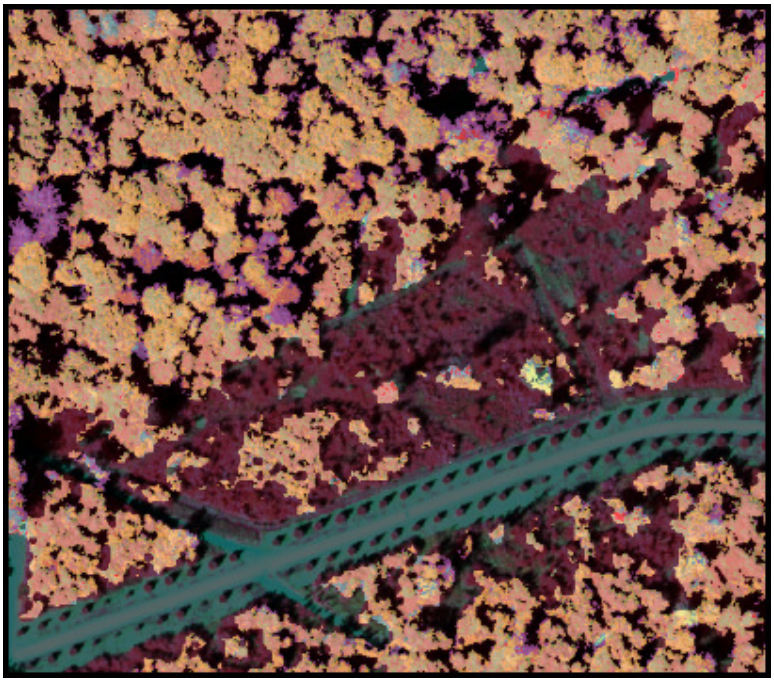

Figure 6.17 – Mahalanobis distance based method: dominance of deciduous trees

6.3.2 QUANTITATIVE EVALUATION

For the quantitative evaluation, the validation samples and the classification results were used to create three confusion matrices (one for each classification method): a confusion matrix is, let's say, a table in which each cell contains the number of pixels belonging to the class of the row but classified as belonging to the column class by the algorithm. A confusion matrix is very useful not only to evaluate the amount of misclassified pixels but also to understand among which classes the misclassification occurs more frequently.

It was decided to plot the values to perform a comparison and a general assessment of the three methods (to see all the graphs, please refer to Appendix D).

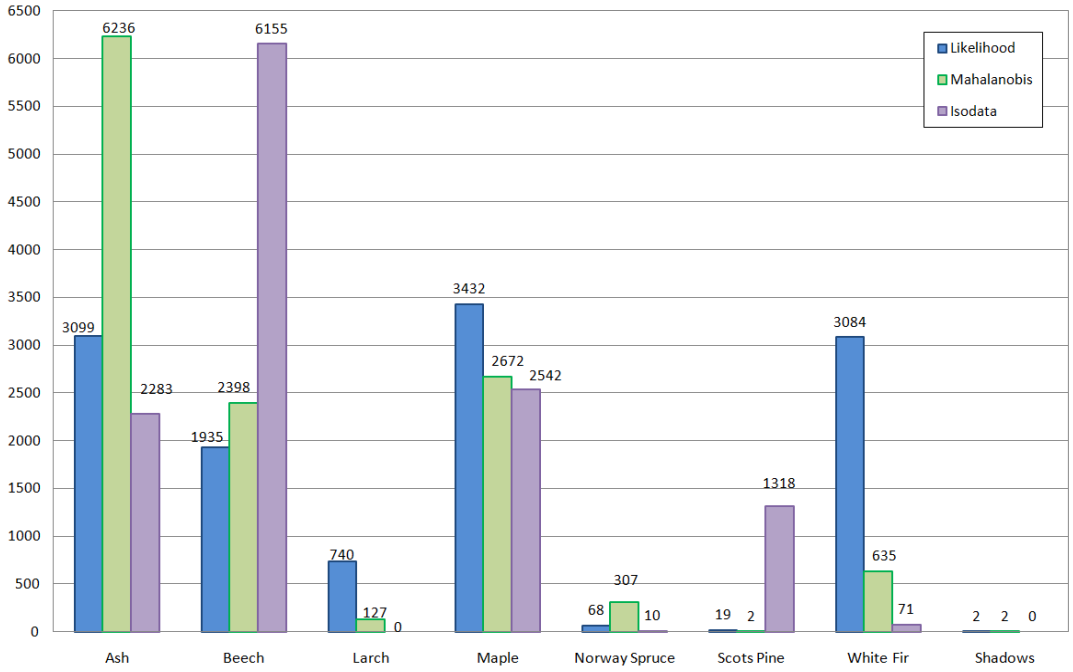

Graph 6.6 – Ash: representation of how ash was classified by the algorithms

Both the graphs (6.6 and 6.7. below) confirmed what was supposed during the visual inspection:

- ASH: it's quite strange to observe that the Mahalanobis method performed the best classification, whereas the expected worse one belongs to ISODATA, which misclassified ash mainly as beech (the most widespread). Even if the more frequent misclassifications were verified between the deciduous species, it has to be underlined the great number of pixels classified, strangely, as white fir by the Maximum Likelihood algorithm;

- NORWAY SPRUCE: it seems that only the Mahalanobis distance based method was able to classify this species properly, while the others two had similar performances: Maximum Likelihood algorithm split the pixels mainly between two classes, that is, larch and white fir. On the contrary, the ISODATA classified almost all the pixels as Scots pine, as already mentioned in the qualitative evaluation.

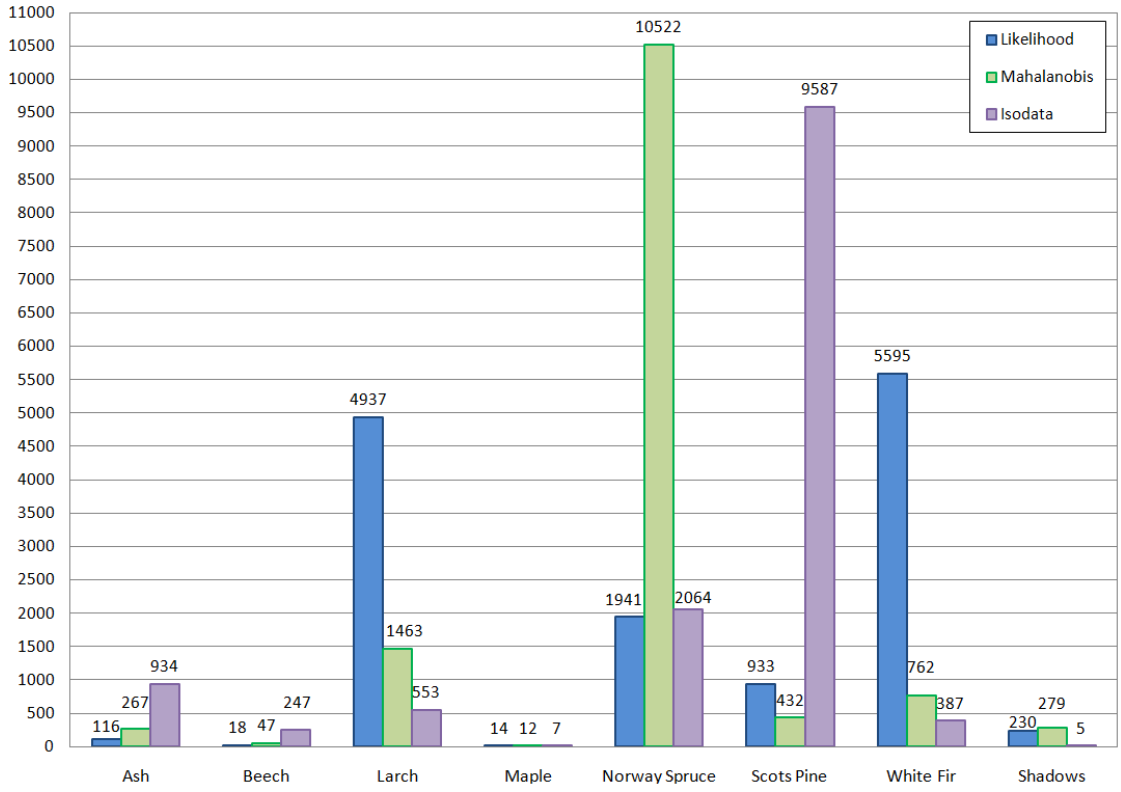

Graph 6.7 – Norway spruce: representation of how Norway spruce was classified by the algorithms

Furthermore, it should be noted that some pixels belonging to the Norway spruce were misclassified as “shadows”: it seems a bit strange since the two spectral signatures should be completely separable. However, an explanation can be found by considering the fact that some tree samples encompassed shadows pixels.

An unexpected result was, for sure, that the Mahalanobis distance method had better performances than the Maximum Likelihood one, which produced really unsatisfying results (maybe more inspections should be conducted to understand why). Not unexpected was, instead, the poor ISODATA classification: indeed, it has to be borne in mind that iterative methods are usually employed for a “rapid” classification as the determination of different land covers (water, bare soil, etc.), namely, when different spectral signatures are analyzed.

CONCLUSIONS

The master thesis project here presented focused on procedures for forestry applications and was embedded in the on-going Ph.D. thesis of Lars T. Waser, entitled "Use of high-resolution airborne remote sensing data for derivation of forest area and tree species composition". The work dealt with two different, but equally essential, aspects: the generation of a high resolution DSM and the improvement of tree species classification through an iterative procedure of selection of the input variables.

In the first part, the research investigated the use of Unmanned Aerial Vehicles (UAVs), performing a flight with the Microdrones MD4-200 in October 2009. The captured pictures were conveniently elaborated (radiometric preprocessing, image matching and orientation and stereo pairs production), so that a DSM with 0.08 m as grid spacing was created. Afterwards, it was compared with standard DSMs, namely, those produced by Aerial Photogrammetry with the ADS40 sensor and the LiDAR system.
Different problems were encountered during the imagery processing: first of all, the data set was affected by shadows and blur, elements that led to a details' reduction with influence on the image matching. It was, in fact, quite difficult to find an enough number of satisfactory tie points (TPs), especially on multi overlap areas; moreover, some problems had to be faced in the image orientation part, mainly due to the fact that all the GCPs were aligned in the center of the images. This implies that the rotation ω along the X axis (roll) could vary with repercussions on the Z coordinates, in particular of all the points near the images' edges. Despite all these issues, the comparison between the generated high resolution DSM and the standard ones (on a flat surface) demonstrated the potential reliability of the former, even for forestry applications.
Thus, it must be pointed out that UAVs will surely play a key role, especially by allowing frequent observations and monitoring: in addition, high resolution orthophotos (generated from their images), in presence of NIR data, could improve the study of the vegetative age and state, beyond the species classification.
However, despite these encouraging results, further studies are needed, including those concerning the development of new methodologies and software suitable for the UAVs imagery processing.

In the second part, instead, some derived quantities ('variables') were derived from the ADS40 SH52 imagery and from LIDAR DTM and DSM. Some of these variables, grouped into geometric, spectral and textural features, could be correlated to each other and/or provide redundant information, so that a selection procedure was needed. Hence, the work focused on finding the best variables' combination able to facilitate the separation, in the so-called "multispectral space", between seven tree species classes.
This operation aimed to improve the subsequent classification, performed with several algorithms (Isodata, Maximum Likelihood method and the one based on the Mahalanobis distance). Though the variables' selection comprised procedure like the principal components analysis, the bands algebra and different iterative evaluation of the classes' separability, the classification didn't seem to really improve: in particular, the Maximum Likelihood method produced poor performances and deeper inspections to understand the reasons should be carried out.
A useful postprocessing can be performed to try to improve the results: for instance, the "salt and pepper" noise (present in the classified images) could be reduced through a smoothing method; another technique could be the segmentation, after which it's possible to assign a polygon (i.e. a tree crown) to the class to which the majority of its pixels belong.
However, it has to be said that other procedures could be evaluated beyond the ones described in this project: in fact, logistic regression models based on the neuronal network algorithm have already produced interesting results and could be further explored.

BIBLIOGRAPHY

- Artuso R., Bovet S., Streilein A. (2003) - "Practical methods for the verification of countrywide terrain and surface models". Proceedings of the ISPRS working group III. Vol. XXXIV, part 3/W 13;
- Baltsavias E., Zhang L., Eisenbeiss H. (2005) – "DSM generation and interior orientation determination of IKONOS images using a test field in Switzerland". ISPRS Workshop on "High-resolution Earth imaging for geospatial information". Hannover, Germany;
- Baltsavias E., Gruen A., Eisenbeiss H., Zhang L., Waser L.T (2008) – "High-quality image matching and automated generation of 3D tree models". International Journal of Remote Sensing, 1366 - 5901, 29: 5, pp. 1243 – 1259;
- Barazzetti L., Remondino F., Scaioni M., Brumana R. (2002) – "Fully automatic UAV image based sensor orientation". International Society for Photogrammetry and Remote Sensing (ISPRS), XXXVIII;
- De Fátima Bento M. (2008) - "Unmanned Aerial Vehicles: an overview". Working Papers. InsideGNSS;
- Dermanis A., Biagi L. (2002) – "Telerilevamento. Informazione territoriale mediante immagini da satellite". Casa Editrice Ambrosiana;
- Eisenbeiss H. (2004) – "A mini Unmanned Aerial Vehicle (UAV): system overview and image acquisition". International Workshop on "Processing and visualization using high-resolution imagery". Pitsanulok, Thailand;
- Eisenbeiss H., Zhang L. (2006) – "Comparison of DSMs generated from mini UAV imagery and terrestrial laser scanner in a cultural heritage application". ISPRS Commission V Symposium on "Image Engineering and Vision Metrology";
- Eisenbeiss H (2009) – "UAV Photogrammetry". Ph. D. thesis - Institute of Geodesy and Photogrammetry, ETH Zürich. Zurich, Switzerland;
- Erdas Imagine 2010-Documentation;
- Federal Office for the Environment (FOEN). (2007) – "Switzerland's Initial Report under Article 7, paragraph 4 of the Kyoto Protocol";

- Freeman M., Akca D., Gruen A., Sargent I. (2008) - "Quality assessment of 3D building data by 3D surface matching". The International Archives of the Photogrammetry, Remote Sensing and Spatial Information Sciences. Vol. XXXVII, part B2;
- Fricker P. (2001) – "ADS40 – Progress in digital aerial data collection". Photogrammetric Week 01;
- Gilardoni O. (2007) - "Confronto tra tecniche di modellazione image–based e range – based per applicazioni terrestri". Master thesis – Corso di Laurea Specialistica in Ingegneria per l'Ambiente e il Territorio, Politecnico di Milano (Polo Regionale di Como). Como, Italy;
- Gruen A., Akca D. (2005) – "Least squares 3D surface and curve matching". ISPRS Journal of Photogrammetry and Remote Sensing, 59, pp. 151 – 174;
- Gruen A., Zhang L., Eisenbeiss H. (2005) – "3D precision processing of high resolution satellite imagery". ASPRS Annual Conference, Baltimore (Maryland), USA;
- Herwitz S.R., Johnson L.F., Higgins R.G., Leung J.G., Dunagan S.E. (2002) – "Precision agriculture as a commercial application for solar – powered Unmanned Aerial Vehicles". AIAA Technical Conference and Workshop on Unmanned Aerospace Vehicles, Systems, Technologies and Operations. Portsmouth, Great Britain;
- Jensen J. R. (2005) – "Introductory digital image processing: a remote sensing perspective". Upper Saddle River, NY: Prentice Hall, USA;
- Kellenberger T. W., Nagy P. (2008) – "Potential of the ADS40 aerial scanner for archaeological prospection in Rheinau, Switzerland". The International Archives of the Photogrammetry, Remote Sensing and Spatial Information Sciences. Vol. XXXVII, part B4. Beijing, China;
- Kerdsrilek J. (2010) - "Application of airborne remote sensing in forest tree (Comparison of ADS40, UAV and LiDAR data)". Master thesis – Institute of Geodesy and Photogrammetry, ETH Zürich. Zurich, Switzerland;
- Neeff T., von Luepke H., Schoene D. (2006) – "Choosing a forest definition for the Clean Development Mechanism". Forest and Climate change working paper 4;

- Pateraki M. N. (2005) – "Adaptive multi–image matching for DSM generation from airborne linear array CCD data". Ph. D. thesis-Institute of Geodesy and Photogrammetry, ETH Zürich. Zurich, Switzerland;
- Pueschel H., Sauerbier M., Eisenbeiss H. (2008) – "A 3D model of Castle Landenberg (CH) from combined photogrammetric processing of terrestrial and UAV – based images". XXI ISPRS Congress. Beijing, China;
- Sandau R. et al. (2000) – "Design principles of the LH Systems ADS40 Airborne Digital Sensor". IAPRS - International Archives of Photogrammetry and Remote Sensing. Vol. XXXIII, part B1. Amsterdam, The Netherlands;
- Sauerbier M., Eisenbeiss H. (2010) – "UAVs for the documentation of archaeological excavations". International Archives of Photogrammetry, Remote Sensing and Spatial Information Sciences, Commission V Symposium. Vol. XXXVIII, part 5. Newcastle upon Tyne, Great Britain;
- Waser L.T., Baltsavias E., Ecker K., Eisenbeiss H., Ginzler C., Küchler M., Thee P., and Zhang L. (2008) – "High-resolution digital surface models (DSM) for modeling fractional shrub/tree cover in a mire environment". International Journal of Remote Sensing, *29*(5), pp. 1261 – 1276;
- Waser L. T., Ginzler G., Kuechler M., Baltsavias E., Hurni L. (2010) – "Semi-automatic classification of tree species in different forest ecosystems by spectral and geometric variables derived from Airborne Digital Sensor (ADS40) and RC30 data". Remote Sensing of Environment;
- Waser L. T. (ongoing) – "Use of high-resolution airborne remote sensing data for derivation of forest area and tree species composition". Ph. D. thesis - Swiss Federal Institute for Forest, Snow and Landscape Research (WSL). Zurich, Switzerland;
- Wolff K., Gruen A. (2007) – "DSM generation from early ALOS/PRISM data using SAT-PP". Geoscience and Remote Sensing Symposium, IGARSS 2007. IEEE International. Barcelona, Spain;
- Zhang C. (2008) – "An UAV–based photogrammetric mapping system for road condition assessment". The International Archives of the Photogrammetry, Remote Sensing and Spatial Information Sciences. Vol. XXXVII, part B5. Beijing, China.

WEBSITE CITATIONS

- http://www.swisstopo.admin.ch/internet/swisstopo/en/home/apps/calc/reframe.html: SWISSTOPO webpage “Reframe” for coordinate transformations – April 30, 2010;
- http://www.fao.org/forestry/en/: official webpage of Food and Agriculture Organization of the United Nations (FAO), forestry section – November 3, 2010;
- http://www.lfi.ch/index-en.php: official webpage of Swiss National Forest Inventory (NFI)-November 3, 2010;
- http://www.microdrones.com/en_md4-200_introduction.php: information and technical specifications of the Microdrones MD4 – 200 – November 8, 2010;
- http://www.dpreview.com/reviews/specs/Panasonic/panasonic_dmcfx35.asp: technical specifications of the Panasonic Lumix DMC – FX35 camera – November 8, 2010;
- http://www.esrith.com/Support/document/ads40.pdf: information and technical specifications of the ADS40 sensor – November 9, 2010;
- http://www.auvsi.org/AUVSI/AUVSI/Home/Default.aspx: official webpage of Association for Unmanned Vehicle Systems International (AUVSI) – November 24, 2010;
- http://www.zenit-sa.com/index.php?lingua=1&nav=8: Microdrones dedicated webpage of Zenit S.r.l. – cartographic services and technologies – November 24, 2010.

I'd like to express gratitude to all the people who gave me the possibility to perform my master thesis project abroad, at the **Institute of Geodesy and Photogrammetry at** ETHZ: it wasn't simply a work but also an unforgettable and enriching experience.

I want to express my special gratitude to my supervisors, Dr. Emmanuel Baltsavias in Zurich and Dr. Giovanna Sona in Como, for the professionalism, the patience and the availability demonstrated in these months. I also thank them for the precious advices and the encouragement that they gave me.

Furthermore, I want to thank Professor Fernando Sansò and Miss Vittoria Capriccioli, in Como, for making possible my Erasmus and for the time spent in overcoming related problems.

My sincere thanks go to Nusret Demir, Henri Eisenbeiss, David Novák, Haris Papasaika Martin Sauerbier and Lars Waser for their valuable advices and help, as well as for the kindness and the liking shown during my stay at ETHZ.

I give thanks to all the professors for the professionalism and to all my colleagues for sharing "joys and sorrows" during these five years of university. I also thank Cristoph for the nice time spent together.

Obviously I could not forget my parents: thanks for the support and for trusting me during my whole life!

A grateful thanks to two special persons, Francesca and Laura… they know why.

«verae amicitiae sempiternae sunt»

Last but not least, thanks to Giacomo, my love:

«sei l'orizzonte che mi accoglie quando mi allontano...»

APPENDIX A: DSMS COMPARISON RESIDUALS

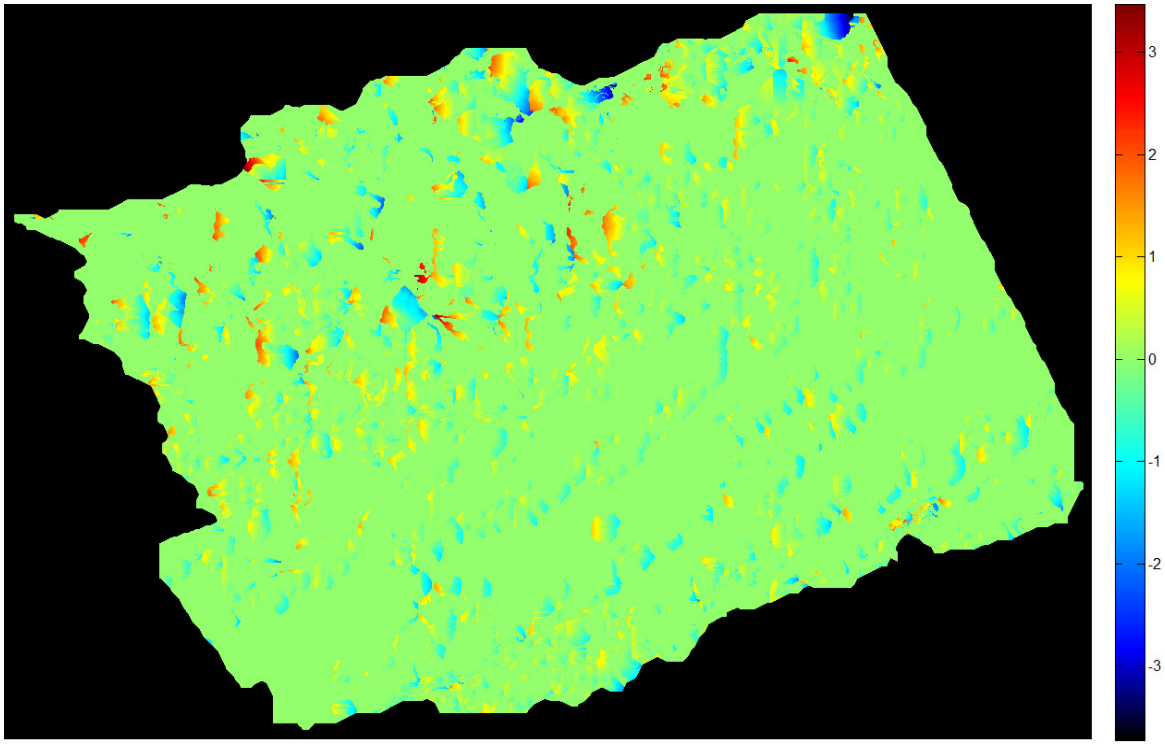

Figure A.1 – Comparison between DSM_UAV and DSM_ADS40: the X residuals

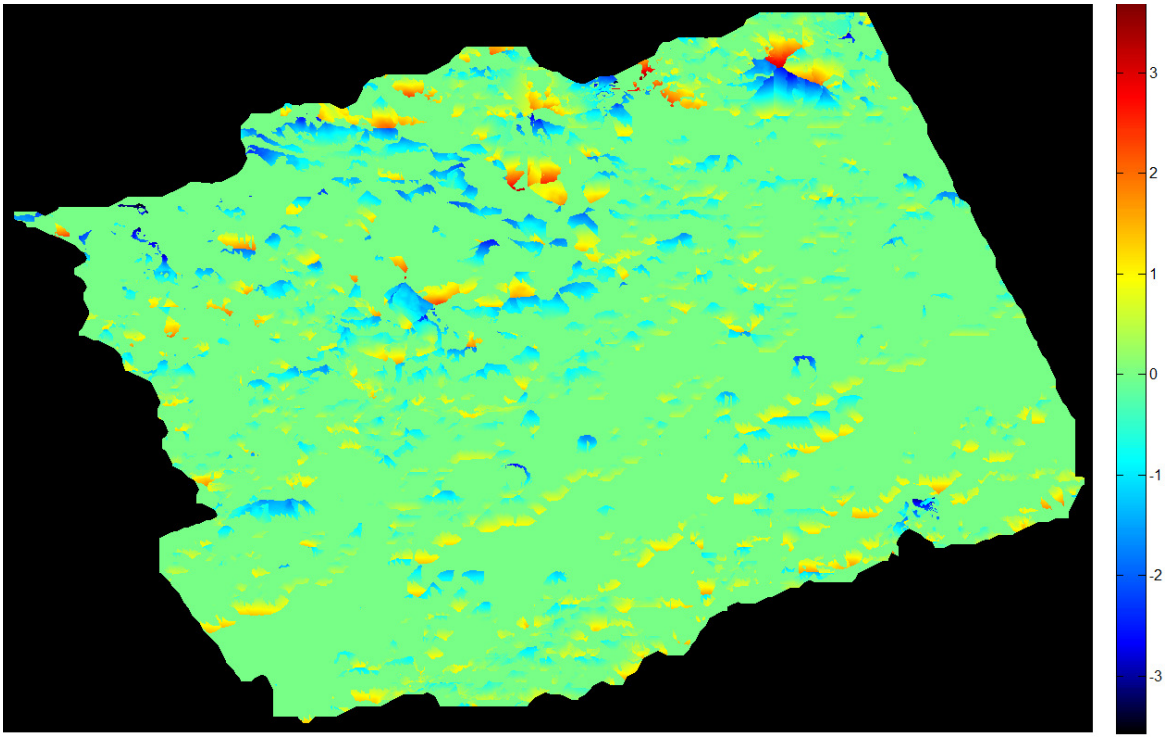

Figure A.2 – Comparison between DSM_UAV and DSM_ADS40: the Y residuals

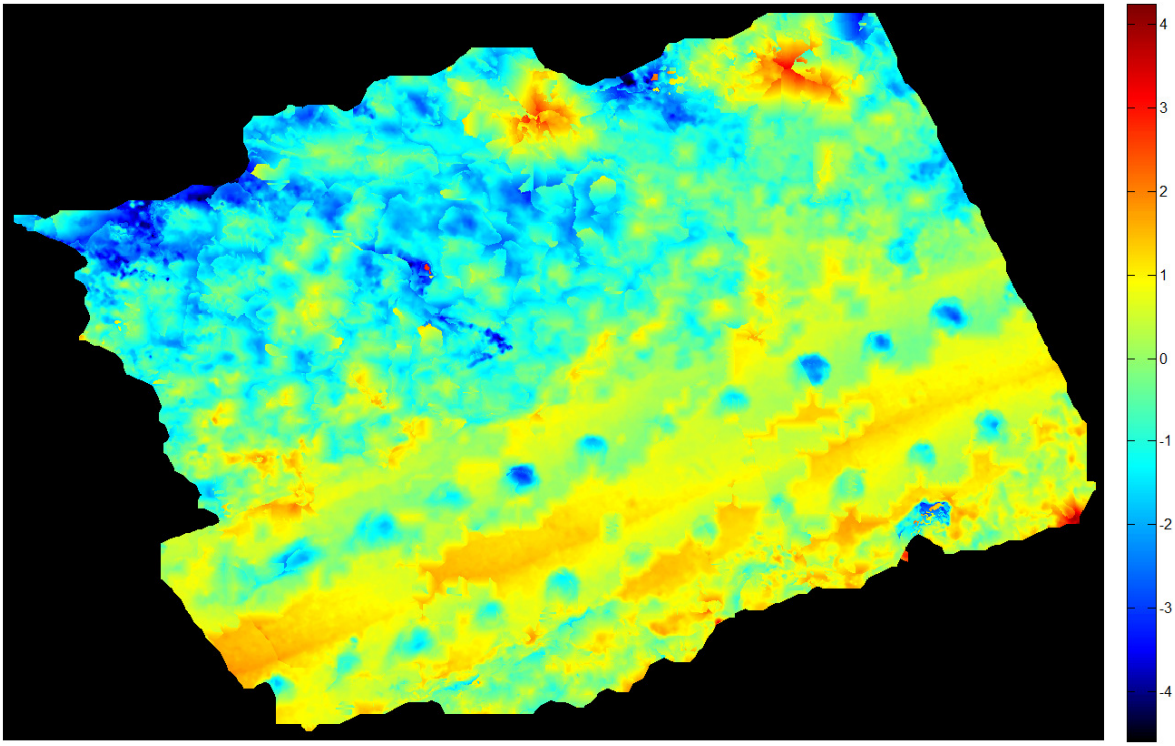

Figure A.3 – Comparison between DSM_UAV and DSM_ADS40: the Euclidean distance

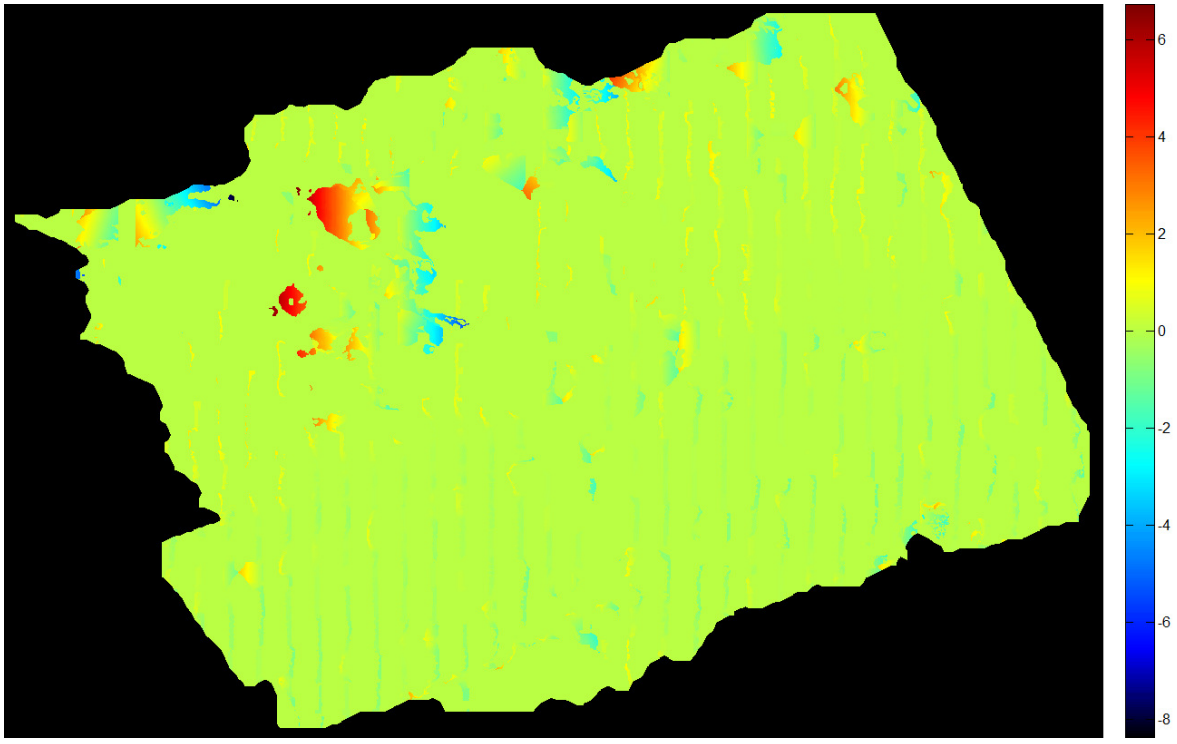

Figure A.4 – Comparison between DSM_UAV and DSM_LiDAR: the X residuals

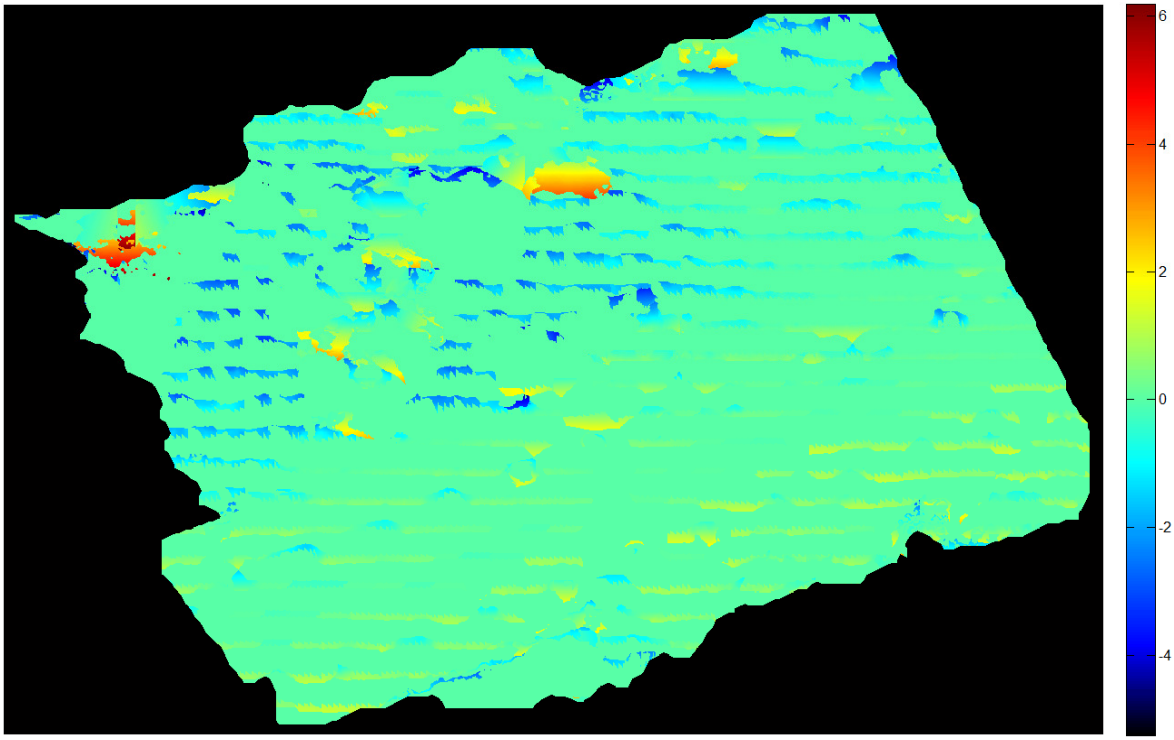

Figure A.5 – Comparison between DSM_UAV and DSM_ LiDAR: the Y residuals

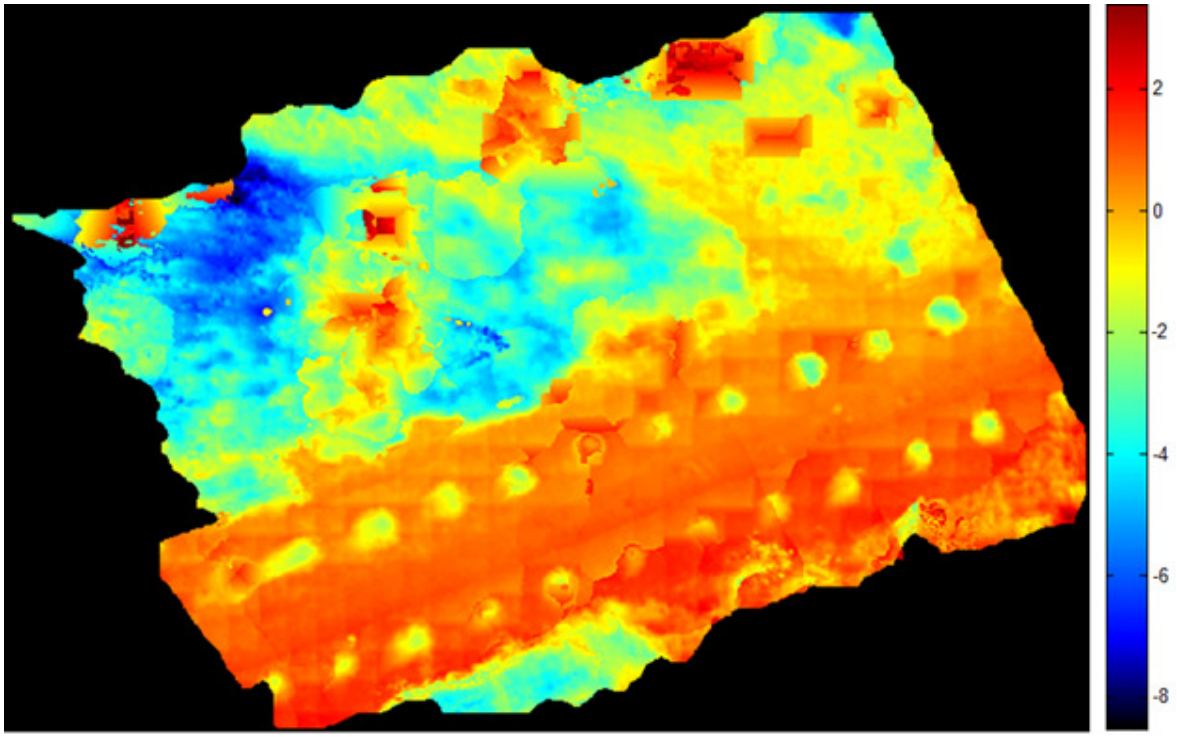

Figure A.6 – Comparison between DSM_UAV and DSM_ LiDAR: the Euclidean distance

APPENDIX B: TREE SPECIES' APPEARANCE

Examples of the selected species' appearance are here shown: after a general trees representation on the left, their aspect in ADS40 RGB imagery (at the center) and in the CIR one (on the right) follow.

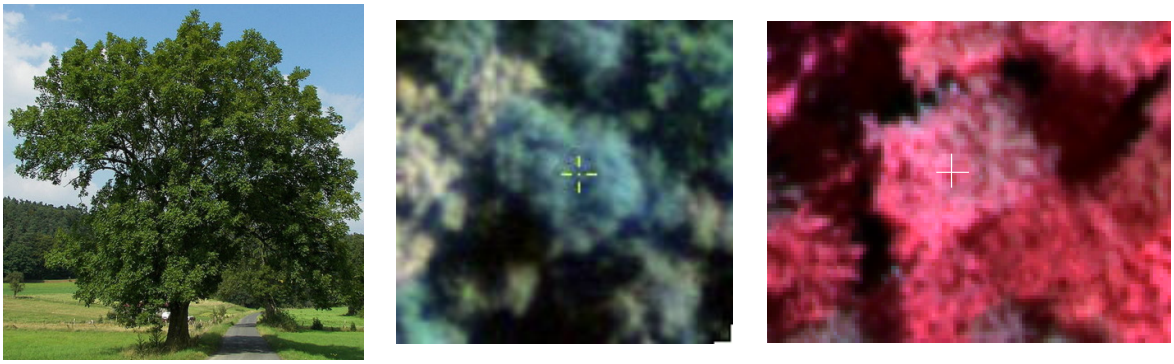

Figure B.1 – Ash (*Fraxinus excelsior*)

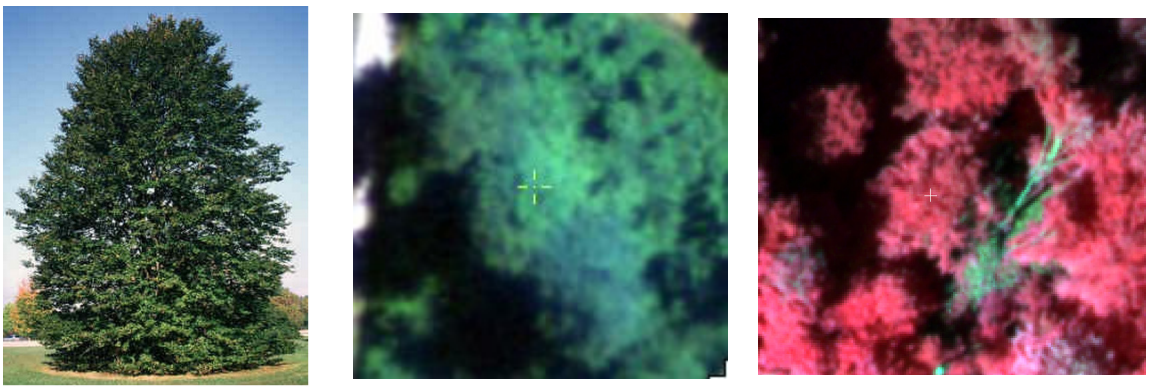

Figure B.2 – Beech (*Fagus sylvatica*)

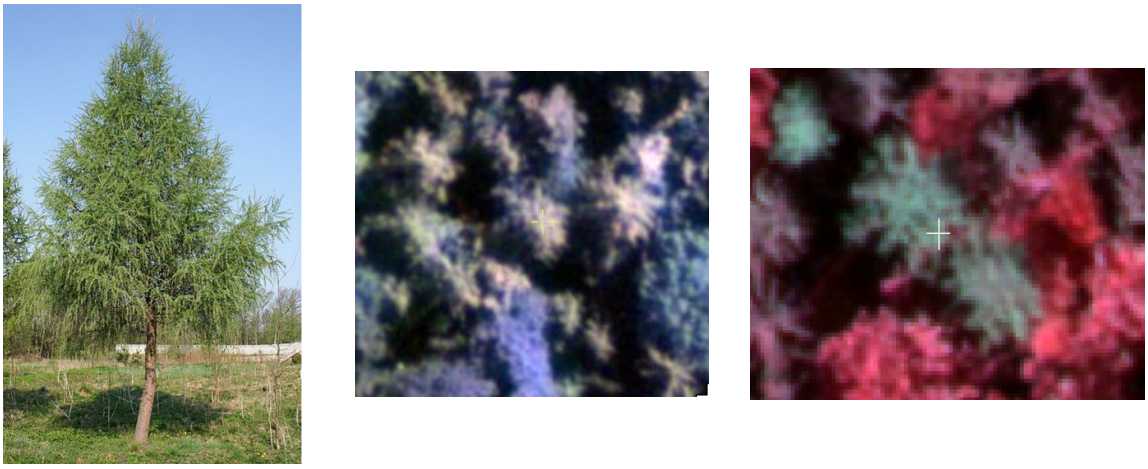

Figure B.3 – Larch (*Larix decidua*)

Figure B.4 – Maple (*Acer sp.*)

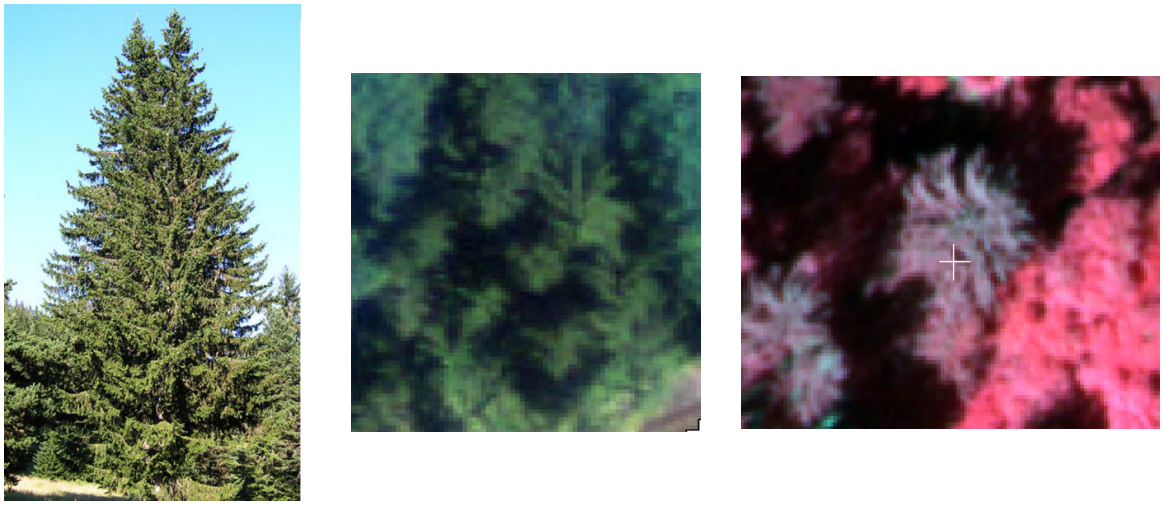

Figure B.5 – Norway spruce (*Picea abies*)

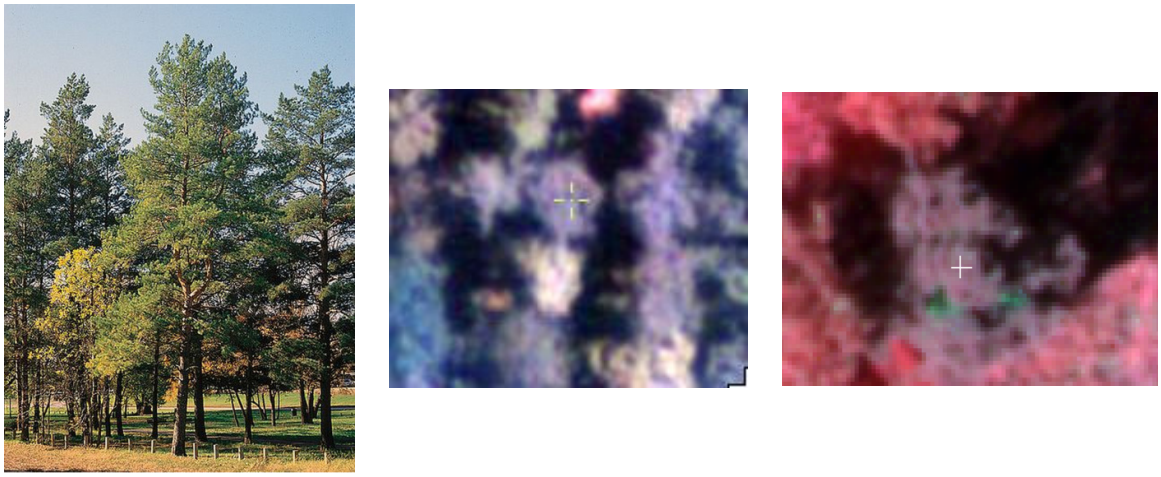

Figure B.6 – Scots pine (*Pinus sylvestris*)

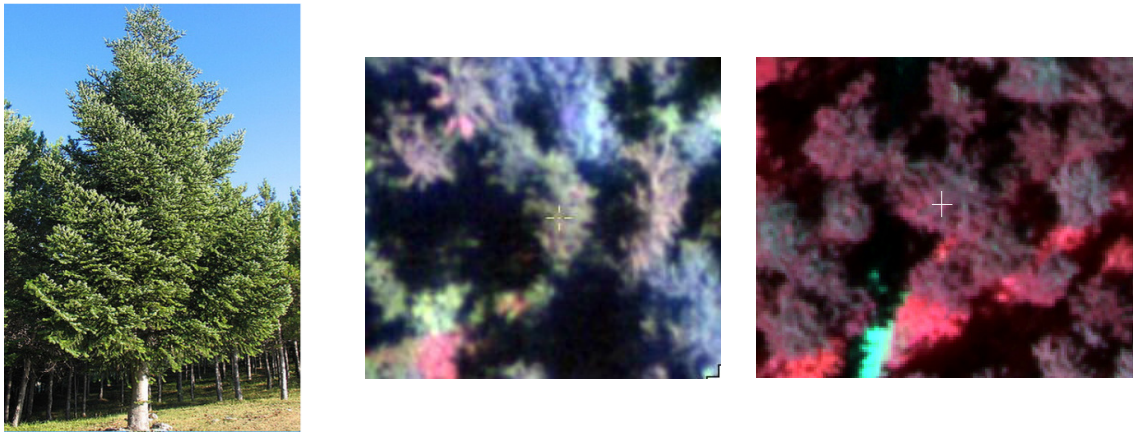

Figure B.7– White fir (*Abies alba*)

APPENDIX C: INPUT VARIABLES DETAILS

VARIABLE NAME	VALUES RANGE	NO DATA VALUE	DATA TYPE
CHM	[0.00; 53.47]	-3.40E+38	Float
Curvature	[-66978; 85419]	-2.15E+09	Signed 32-bit
Slope	[0; 89]	-128	Signed 8-bit
Aspect	[-1; 359]	-32768	Signed 16-bit
Planimetry	[-40025; 49548]	-2.15E+09	Signed 32-bit
Profile	[-45269; 45211]	-2.15E+09	Signed 32-bit
Original Red band	[69; 16666]	0	Unsigned 16-bit
Original Green band	[176; 18986]	0	Unsigned 16-bit
Original Blue band	[418; 12094]	0	Unsigned 16-bit
Original NIR band	[0; 65535]	-2.15E+09	Signed 16-bit
Ratio_Red	[0.0044; 0.3323]	-3.40E+38	Float
Ratio_Green	[0.0087; 0.4125]	-3.40E+38	Float
Ratio_Blue	[0.0102; 0.6772]	-3.40E+38	Float
Ratio_NIR	[0.0000; 0.9743]	-3.40E+38	Float
RGB_IHS_Intensity	[0.0213; 0.9438]	-3.40E+38	Float
RGB_IHS_Hue	[0.0002; 359.9987]	-3.40E+38	Float
RGB_IHS_Saturation	[0.0002; 0.8659]	-3.40E+38	Float
CIR_IHS_Intensity	[0; 1]	-3.40E+38	Float
CIR_IHS_Hue	[0; 359.9928]	-3.40E+38	Float
CIR_IHS_Satuation	[0; 1]	-3.40E+38	Float
NDVI	[-1; 1]	-3.40E+38	Float
RGB_PCA_band 1	[462.3206; 27580.0351]	-3.40E+38	Float
RGB_PCA_band 2	[-3633.3970; 2274.2502]	-3.40E+38	Float
RGB_PCA_band 3	[-3810.5501; 4457.9253]	-3.40E+38	Float
CIR_PCA_band 1	[0; 106971.2969]	-3.40E+38	Float
CIR_PCA_band 2	[-32417.8145; 68541.9531]	-3.40E+38	Float
CIR_PCA_band 3	[-24203.4902; 29230.4746]	-3.40E+38	Float
Skewness_Red	[-3471.4678; 8217.1074]	-3.40E+38	Float
Skewness_Green	[-3333.0713; 8459.6875]	-3.40E+38	Float
Skewness_Blue	[-2210.0925; 4971.4883]	-3.40E+38	Float
Skewness_NIR	[-28139.373; 37312.5703]	-3.40E+38	Float

Table C.1 – Values range, No Data value and data type of the 31 input variables

APPENDIX D: CONFUSION MATRICES

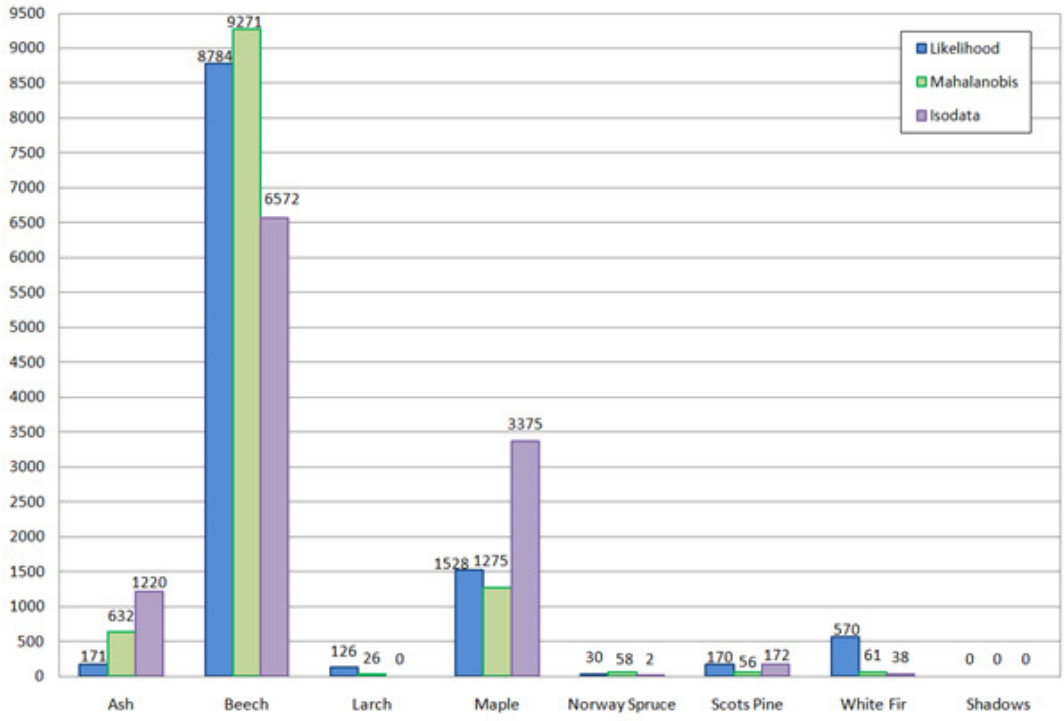

Graph D.1 – Beech (*Fagus sylvatica*)

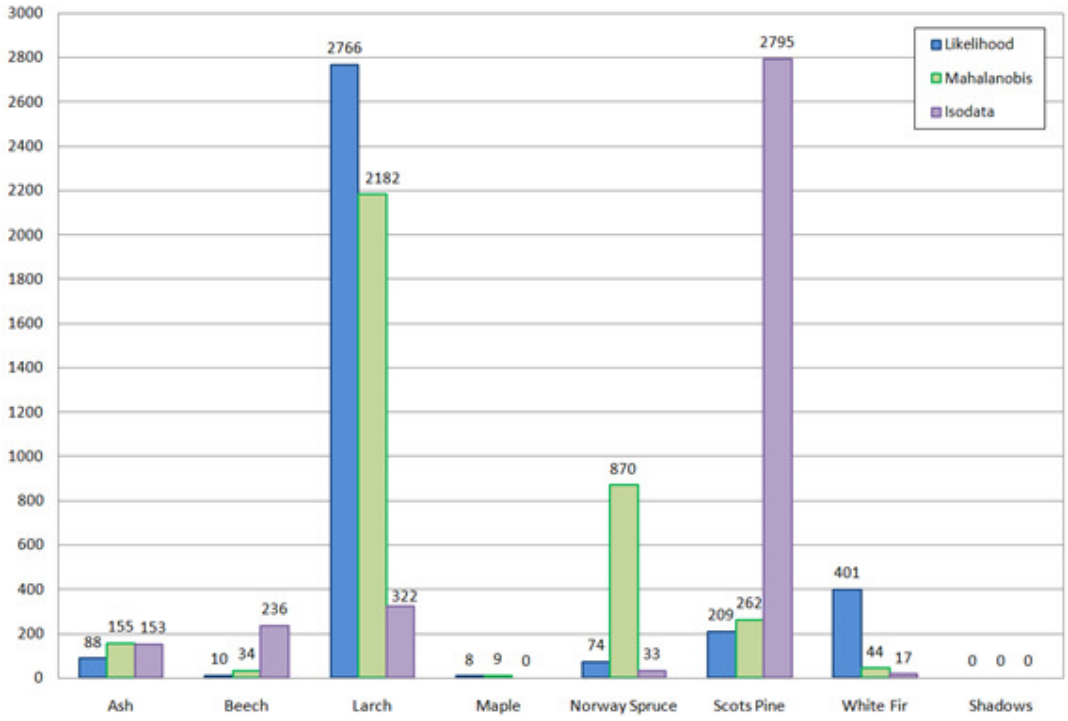

Graph D.2 – Larch (*Larix decidua*)

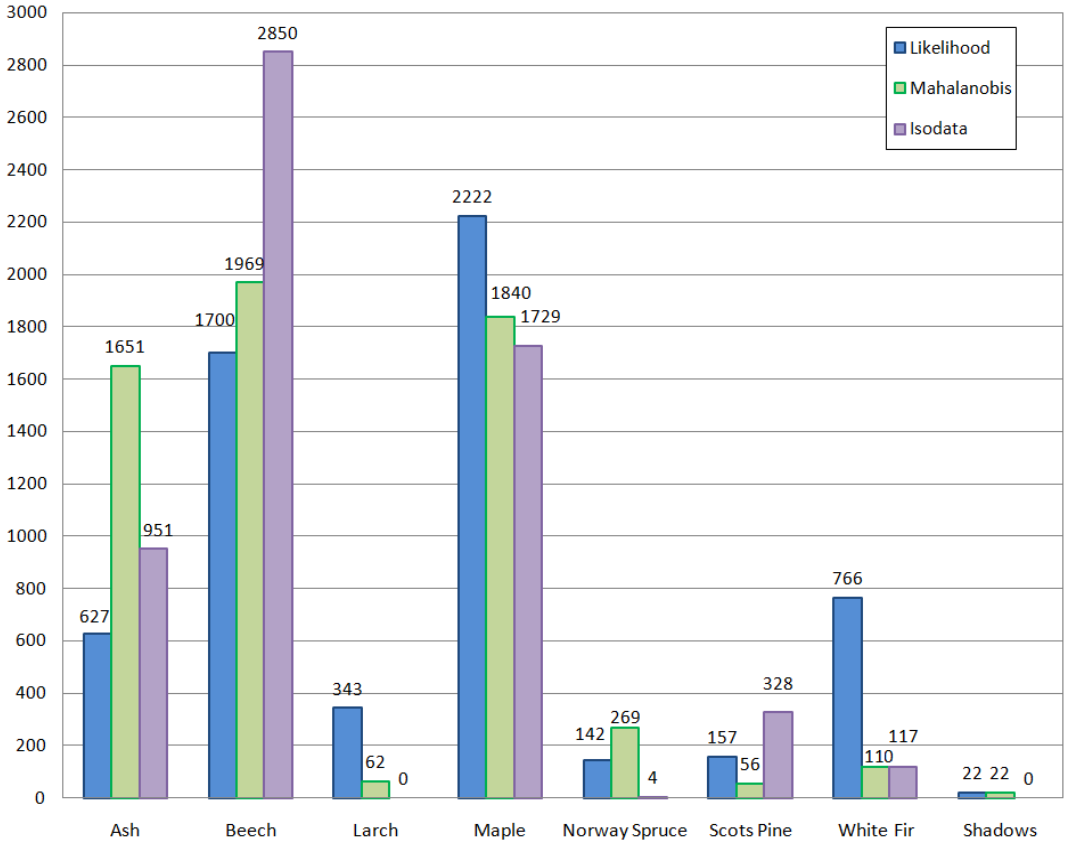

Graph D.3 – Maple (*Acer sp.*)

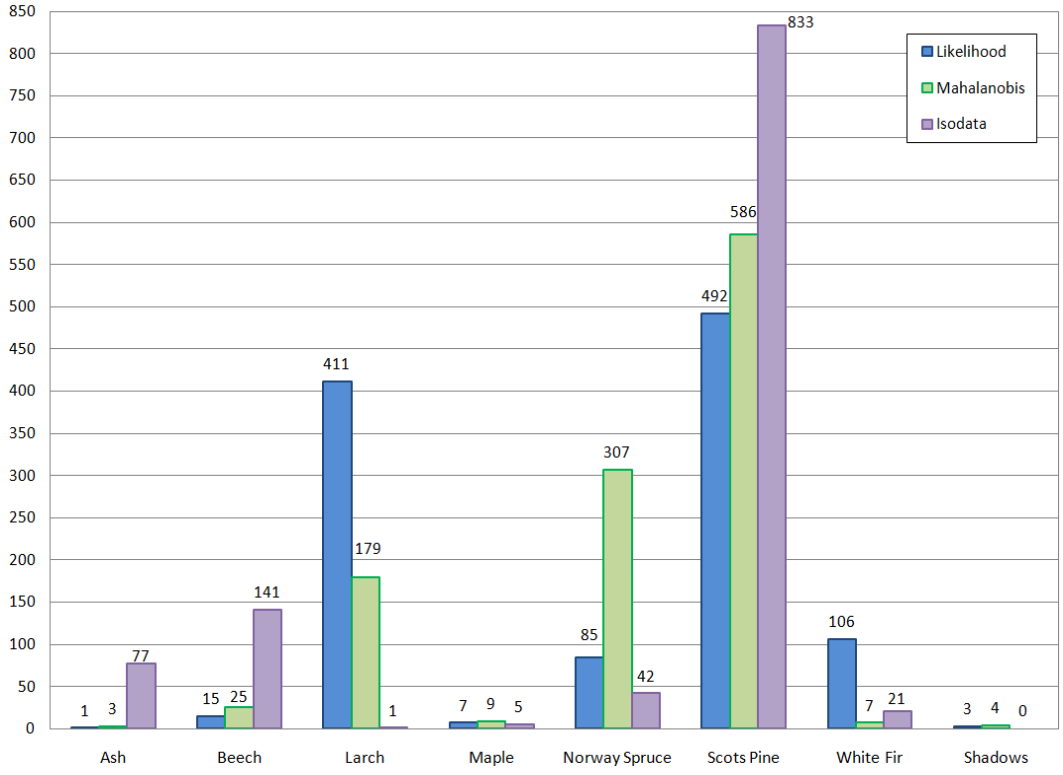

Graph D.4 – Scots pine (*Pinus sylvestris*)

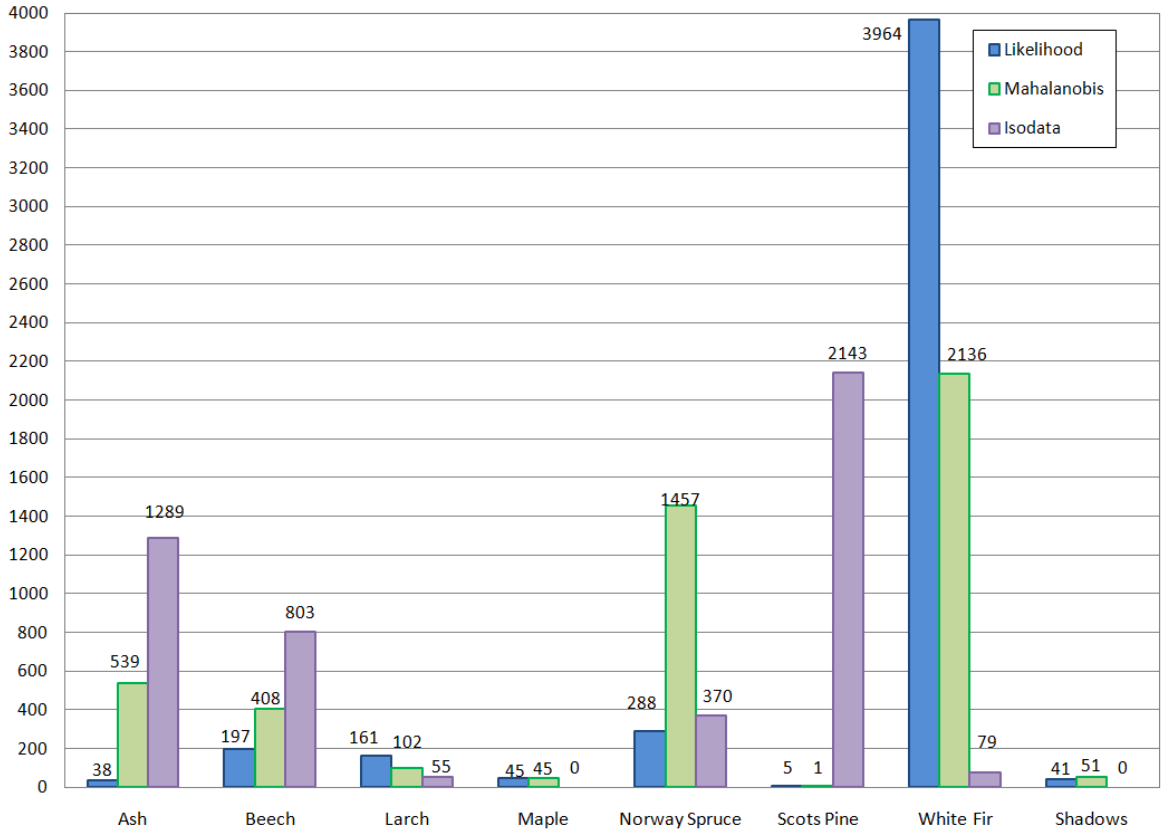

Graph D.5– White fir (*Abies alba*)